

POLITECNICO DI TORINO
UNIVERSIDAD POLITÉCNICA DE MADRID

Master of Science in Civil Engineering



Master's Degree Thesis:

Numerical simulation of shear tests on RC, FRC,
prestressed HPFRC beams without shear
reinforcement

Supervisor:

Prof. Ing. Giuseppe Carlo Marano

Co-supervisor:

Prof. Ing. Hugo Corres Peiretti

Prof. Ing. Leonardo Todisco

Prof. Ing. Stefano Mariani

Candidate:

Antonella Marinelli

275884

Academic Year 2020/2021

December, 2021

A Nonna Maria.

Abstract

Nowadays, the development of modern buildings and infrastructures requires best performing materials in terms of high strength, high toughness, and energy absorption ability. For these reasons the mechanical and structural behavior of Fiber Reinforced Concrete (FRC) and High Performance Fiber Reinforced Concrete (HPFRC) is investigated in this work. In particular, this thesis is focused on the shear behaviour of beams without conventional shear reinforcement. The main advantages are the reduction of material consumption and construction time.

The FRC shear failure domain is related both to its tension and compression properties, characterized by a high level of non-linearity of the problem due to the ductility of the fibers. Consequently, in order to assess the shear structural behaviour of fiber reinforced elements, a nonlinear finite element analysis (NFEA) was conducted. The aim of this thesis is to provide practical recommendations for the numerical modelling of fiber reinforced elements in order to develop reasonable and reliable designs.

The nonlinear material characterization requires several modelling options and input parameters. Furthermore, an accurate prediction of the failure mechanism of the FRC or HPFRC beam can be detected when a careful modelling of the stress-strain relationship in tension and compression or numerical instabilities such as convergence difficulties and mesh sensitivity are taken into account.

In this research work, a modelling in *STKO OpenSees*© of two sets of beams is presented. The first set considered the passive reinforced beams, which is composed of three different rectangular shaped sections. The beams are made of three different materials: normal concrete, and two fiber reinforced concretes with different fiber volumes. The second set consists of four prestressed HPFRC beams with different I-beam cross sections. The results of the numerical analysis are compared with the experimental one in order to evaluate the reliability of numerical predictions, discussing how the parameters considered into the analysis affect the solution. Hence, some of the investigated beams are modelled in another FEA software, called *JCONC*, able to predict the failure conditions in terms of load, displacement and crack formations, considering a concrete rigid plastic stress-strain relationship. The results obtained have been compared with the

STKO Opensees© ones, which take into account a more complex stress-strain law for concrete.

Finally, the modelling strategy is applied for HPFRC prestressed I-beams designed by the Structural Laboratory Team of Universidad Politécnica de Madrid, partnered with Acciona S.A, with the aim to predict failure element in the future experimentation steps.

The work remarks that nonlinear finite element analysis are only numerical predictions and not the reality of physical behaviour. This assumption must guide practitioners' criteria in a preliminary design phase to avoid rough mistakes in the final project.

Index

Abstract.....	1
Figure Index.....	6
Table Index	11
Introduction	16
1. Literature review.....	18
1.1 Steel fiber reinforced concrete SFRC	18
1.2 High performance reinforced concrete HPFRC.....	19
1.3 Codes in force	20
1.4 Mechanical properties of FRC and HPFRC	21
1.4.1 Compressive behaviour	21
1.4.2 Tensile behavior	23
1.4.3 Flexural behaviour.....	26
1.4.4 Shear behaviour.....	27
2. FEA: numerical representation of experimental results with <i>STKO Opensees</i> ©	31
2.1 Introduction on Finite Element Method FEM	31
2.2 Case study 1: Minelli's experimentations.....	32
2.2.1 FEM modelling strategies	34
2.2.2 Plane Reinforced Concrete: result and discussion	45
2.2.3 Fiber Reinforced Concrete: result and discussion.....	56
2.3 Case study 2: Cuenca's Experimentation	71
2.3.1 FEM modelling strategies	73
2.3.2 Pre-stressed fiber reinforced concrete: result and discussion.....	75
3. FEA: numerical representation of experimental results with <i>JCONC</i>	81
3.1 Case study 1: Minelli's experimentations.....	81

3.1.1	FEM Modelling strategies	81
3.1.2	Fiber Reinforced Concrete: result and discussion.....	85
3.2	Case study 2: Cuenca’s experimentations.....	87
3.2.1	FEM modelling strategies	87
3.2.2	Pre-stressed fiber reinforced concrete: result and discussion.....	90
4.	FEA: prediction of experimental results with <i>STKO Opensees</i> ©	92
4.1	Case study 3: UPM and Acciona S.A. beams.....	92
4.1.1	FEM modelling strategies	94
4.1.2	Result and discussion	99
5.	FEA: prediction of experimental results with <i>JCONC</i>	107
5.1	Case study 3: UPM and Acciona S.A. beams.....	107
5.1.1	FEM modelling strategies	107
5.1.2	Results and discussion.....	108
6.	Comparison between Experimental results, <i>STKO Opensees</i> and <i>JCONC</i> predictions	110
6.1	Case study 1: Minelli’s experimentations.....	112
6.2	Case study 2: Cuenca’s experimentations.....	115
6.3	Case study 3: UPM and Acciona S.A. beams.....	118
7.	Conclusions	121
8.	Future developments	125
9.	Bibliography.....	127
Annex 1	132
1.1	Evaluation of control parameters for Minelli’s beams	132
Annex 2	156
2.1	FEM cross section of Cuenca’s beams	156

2.2 Pre-stressing action on Cuenca's beams.....	157
2.3 FEM cross section of UPM's beams	160
2.4 Pre-stressing action on UPM's beams	160
Annex 3	161
3.1 Analytic evaluations with MC10 and EC2-draft.....	161

Figure Index

<i>Fig. 1 - Steel fiber types [4].....</i>	<i>19</i>
<i>Fig. 2 - Compressive strength range for distinction between FRCs [7].....</i>	<i>20</i>
<i>Fig. 3 - Comparison between stress - strain relationship of PC and FRC [1].....</i>	<i>22</i>
<i>Fig. 4 - Experimental tests for determination of tensile properties [14].....</i>	<i>24</i>
<i>Fig. 5 - σ - CMOD relationship for a general FRC element.....</i>	<i>24</i>
<i>Fig. 6 - Simplified constitutive laws: stress-crack opening (solid and dashed lines refer to softening and hardening materials respectively) [fib MC2010 fig.5.6-7] [1].....</i>	<i>25</i>
<i>Fig. 7 - Typical load F vs. CMOD curve for plain concrete and FRC [fib MC2010, Fig. 5.6-6].....</i>	<i>25</i>
<i>Fig. 8 - Stage of cracking and tension stiffening in SFRC members [25].....</i>	<i>27</i>
<i>Fig. 9 - Actions on a concrete cantilever in the shear span of a beam [27].....</i>	<i>28</i>
<i>Fig. 10 - Kani's valley [26].....</i>	<i>29</i>
<i>Fig. 11 - Geometric characteristics of Minelli's specimens [30].....</i>	<i>32</i>
<i>Fig. 12 - Concrete mechanical properties of Minelli's beams [30].....</i>	<i>33</i>
<i>Fig. 13 - Beam geometry in STKO Opensees for Minelli's beam.....</i>	<i>35</i>
<i>Fig. 14 - Concrete stress-strain relationship in compression for STKO Opensees.....</i>	<i>36</i>
<i>Fig. 15 - Concrete stress-strain relationship in tension for STKO Opensees.....</i>	<i>36</i>
<i>Fig. 16 - Stress - crack opening displacement chosen for FRC50 and FRC75.....</i>	<i>37</i>
<i>Fig. 17 - Damage surface for the plane stress case [36].....</i>	<i>39</i>
<i>Fig. 18 - Physical properties in STKO Opensees for Minelli's beams.....</i>	<i>41</i>
<i>Fig. 19 - Quadrilateral Type with 4 nodes.....</i>	<i>41</i>
<i>Fig. 20 - Linear type with 2 nodes.....</i>	<i>41</i>
<i>Fig. 21 - Conditions for Minelli's beams in STKO Opensees.....</i>	<i>43</i>
<i>Fig. 22 - Mesh plot for Minelli's beams in STKO Opensees.....</i>	<i>45</i>
<i>Fig. 23 - Experimental H500PC load-displacement curve with control parameters.....</i>	<i>47</i>
<i>Fig. 24 - Numerical H500PC load-displacement curve with control parameters.....</i>	<i>48</i>
<i>Fig. 25 - Comparison between numerical and experimental load - displacement curve for H500PC.....</i>	<i>49</i>

<i>Fig. 26 - Comparison between numerical (upper figure) and experimental (bottom figure) crack pattern for H500PC</i>	51
<i>Fig. 27 - Comparison between numerical and experimental load - displacement curve for H1000PC</i>	51
<i>Fig. 28 - Comparison between numerical (upper figure) and experimental (bottom figure) crack pattern for H1000PC</i>	52
<i>Fig. 29 - Comparison between numerical and experimental load - displacement curve for H1500PC</i>	53
<i>Fig. 30 - Comparison between numerical (upper figure) and experimental (bottom figure) crack pattern for H1500PC</i>	54
<i>Fig. 31 - P_{cr} (right figure) and P_u trends (left figure) for PC beams</i>	55
<i>Fig. 32 - δ (right figure) and S_1 (left figure) trends for PC beams</i>	55
<i>Fig. 33 - S_2 trend for PC beams</i>	55
<i>Fig. 34 - Comparison between numerical and experimental load - displacement curve for H500FRC50</i>	57
<i>Fig. 35 - Comparison between numerical (upper figure) and experimental (bottom figure) crack pattern for H500FRC50</i>	58
<i>Fig. 36 - Comparison between numerical and experimental load - displacement curve for H1000FRC50</i>	58
<i>Fig. 37 - Comparison between numerical (upper figure) and experimental (bottom figure) crack pattern for H1000FRC50</i>	59
<i>Fig. 38 - Comparison between numerical and experimental load - displacement curve for H1500FRC50</i>	60
<i>Fig. 39 - Comparison between numerical (upper figure) and experimental (bottom figure) crack pattern for H1500FRC50</i>	61
<i>Fig. 40 - Comparison between numerical and experimental load - displacement curve for H500FRC75</i>	61
<i>Fig. 41 - Comparison between numerical (upper figure) and experimental (bottom figure) crack pattern for H500FRC75</i>	62
<i>Fig. 42 - Comparison between numerical and experimental load - displacement curve for H1000FRC75</i>	63
<i>Fig. 43 - Comparison between numerical (upper figure) and experimental (bottom figure) crack pattern for H1000FRC75</i>	64
<i>Fig. 44 - Comparison between numerical and experimental load - displacement curve for H1500FRC75</i>	64

<i>Fig. 45 - Comparison between numerical (upper figure) and experimental (bottom figure) crack pattern for H1500FRC75</i>	65
<i>Fig. 46 - Comparison between numerical (upper figure) and experimental (bottom figure) crack pattern for H1500FRC50 with adjusted G_f</i>	67
<i>Fig. 47 - Comparison between numerical (upper figure) and experimental (bottom figure) crack pattern for H1500FRC50 with adjusted G_f</i>	67
<i>Fig. 48 - Comparison between numerical (upper figure) and experimental (bottom figure) crack pattern for H1000FRC75 with adjusted G_f</i>	69
<i>Fig. 49 - Comparison between numerical (upper figure) and experimental (bottom figure) crack pattern for H1500FRC75 with adjusted G_f</i>	69
<i>Fig. 50 - P_{cr} (right figure) and P_u (left figure) trends for FRC beams</i>	70
<i>Fig. 51 - δ (right figure) and S_1 (left figure) trends for FRC beams</i>	70
<i>Fig. 52 - S_2 trend for FRC beams</i>	70
<i>Fig. 53 - Geometric characteristics of Cuenca's specimens</i>	72
<i>Fig. 54 - Concrete properties of Cuenca's beams</i>	72
<i>Fig. 55 - Element properties plot for Minelli's beams in STKO Opensees</i>	73
<i>Fig. 56 - Comparison of experimental and numerical curve Load - displacement curve for HF600/5</i>	77
<i>Fig. 57 - Final crack damage of HF600/5</i>	78
<i>Fig. 58 - JCONC geometry for H500FRC50</i>	82
<i>Fig. 59 - Concrete stress-strain relationship in JCONC</i>	82
<i>Fig. 60 - Steel stress-strain relationship in JCONC</i>	84
<i>Fig. 61 - Comparison between numerical (left figure) and experimental (right figure) crack pattern for H500</i>	86
<i>Fig. 62 - Comparison between numerical (left figure) and experimental (right figure) crack pattern for H1000</i>	86
<i>Fig. 63 - Comparison between numerical (left figure) and experimental (right figure) crack pattern for H1500</i>	87
<i>Fig. 64 - JCONC geometry for HF600/5</i>	88
<i>Fig. 65 - JCONC crack pattern for HF600/5 (upper figure) and HF400/7 (lower figure)</i>	91
<i>Fig. 66 - JCONC crack pattern for HF400h/6 (upper figure) and HF260/9 (lower figure)</i>	91
<i>Fig. 67 - BMI12 cross section (upper figure) and longitudinal profile (bottom figure)</i>	93

<i>Fig. 68 - UMII2 cross section (upper figure) and longitudinal profile (bottom figure)</i>	93
<i>Fig. 69 - Physical properties of BMI12</i>	96
<i>Fig. 70 - Physical properties of UMI12</i>	96
<i>Fig. 71 - Load-displacement curve for BMI12</i>	99
<i>Fig. 72 - δ, σ_p, σ_b at t_0 and t_f for BMI12</i>	101
<i>Fig. 73 - Crack damage pattern of BMI12 at t_f</i>	102
<i>Fig. 74 - Load-displacement curve for UMI12</i>	103
<i>Fig. 75 - δ, σ_p, σ_b at t_0 and t_f for UMI12</i>	105
<i>Fig. 76 - Crack damage pattern of UMI12 at t_f</i>	106
<i>Fig. 77 - JCONC geometry of UMI12</i>	107
<i>Fig. 78 - JCONC crack pattern for BMI12</i>	109
<i>Fig. 79 - JCONC crack pattern for UMI12</i>	109
<i>Fig. 80 - Ratio overview of results' comparison for Minelli's beams</i>	113
<i>Fig. 81 - Numerical and experimental damage pattern comparison for H500FRC50</i>	114
<i>Fig. 82 - Numerical and experimental damage pattern comparison for H1000FRC50</i>	114
<i>Fig. 83 - Numerical and experimental damage crack comparison for H1500FRC50</i>	115
<i>Fig. 84 - Ratio overview of results' comparison for Cuenca's beams</i>	117
<i>Fig. 85 - Numerical and experimental damage crack pattern comparison for HF600/5</i>	117
<i>Fig. 86 - STKO and JCONC σ_p comparison for BMI12</i>	118
<i>Fig. 87 - STKO and JCONC σ_p comparison for UMI12</i>	118
<i>Fig. 88 - Overview of UPM's beam final shear strength</i>	119
<i>Fig. 89 - Numerical and experimental damage crack pattern comparison for BMI12</i>	120
<i>Fig. 90 - Numerical and experimental damage crack pattern comparison for UMI12</i>	120
<i>Fig. 91 - Experimental H1000PC load-displacement curve with control parameters</i>	132
<i>Fig. 92 - Numerical H1000PC load-displacement curve with control parameters</i>	133
<i>Fig. 93 - Experimental H1500PC load-displacement curve with control parameters</i>	134
<i>Fig. 94 - Numerical H1500PC load-displacement curve with control parameters</i>	135
<i>Fig. 95 - Experimental H500FRC50 load-displacement curve with control parameters</i>	136
<i>Fig. 96 - Numerical H500FRC50 load-displacement curve with control parameters</i>	137

<i>Fig. 97 - Experimental H1000FRC50 load-displacement curve with control parameters</i>	138
<i>Fig. 98 - Numerical H1000FRC50 load-displacement curve with control parameters</i>	139
<i>Fig. 99 - Experimental H1500FRC50 load-displacement curve with control parameters</i>	140
<i>Fig. 100 - Numerical H1500FRC50 load-displacement curve with control parameters</i>	141
<i>Fig. 101 - Experimental H500FRC75 load-displacement curve with control parameters</i>	142
<i>Fig. 102 - Numerical H500FRC75 load-displacement curve with control parameters</i>	143
<i>Fig. 103 - Experimental H1000FRC75 load-displacement curve with control parameters</i>	144
<i>Fig. 104 - Numerical H1000FRC75 load-displacement curve with control parameters</i>	145
<i>Fig. 105 - Experimental H1500FRC75 load-displacement curve with control parameters</i>	146
<i>Fig. 106 - Numerical H1500FRC75 load-displacement curve with control parameters</i>	147
<i>Fig. 107 - Numerical H500FRC50 load-displacement curve with control parameters with G_t adjusted.</i>	148
<i>Fig. 108 - Numerical H1000FRC50 load-displacement curve with control parameters with G_t adjusted</i>	149
<i>Fig. 109 - Numerical H1500FRC50 load-displacement curve with control parameters with G_t adjusted</i>	150
<i>Fig. 110 - Numerical H500FRC75 load-displacement curve with control parameters with G_t adjusted.</i>	151
<i>Fig. 111 - Numerical H1000FRC75 load-displacement curve with control parameters with G_t adjusted</i>	152
<i>Fig. 112 - Numerical H1500FRC75 load-displacement curve with control parameters with G_t adjusted</i>	153
<i>Fig. 113 - Comparison between HF600/5's FEM and real section</i>	156
<i>Fig. 114 - Comparison between HF400h/6's FEM and real section</i>	156
<i>Fig. 115 - Comparison between HF400/7's FEM and real section</i>	156
<i>Fig. 116 - Comparison between HF260/9's FEM and real section</i>	157
<i>Fig. 117 - HF600/5 FEM model section with pre-stressing action</i>	157
<i>Fig. 118 - HF400/7 FEM model section with pre-stressing action</i>	158
<i>Fig. 119 - HF400h/6 FEM model section with pre-stressing action</i>	159
<i>Fig. 120 - HF260/9 FEM model section with pre-stressing action</i>	159
<i>Fig. 121 - Comparison between UMI12 and BMI12's FEM and real section</i>	160

Table Index

<i>Table 1- Concrete compressive parameters inputs of Minelli's beams</i>	36
<i>Table 2 – Concrete tensile parameters inputs of Minelli's beams</i>	37
<i>Table 3 - Steel reinforcement parameters input of Minelli's beams</i>	40
<i>Table 4 - Comparison between the M_{exp} and M_{fl}</i>	45
<i>Table 5 - Data input for the evaluation of H500 experimental S_1</i>	47
<i>Table 6 - Data input for the evaluation of experimental H500 S_2</i>	48
<i>Table 7 - Data input for the evaluation of H500 numerical S_1</i>	48
<i>Table 8 - Data input for the evaluation of H500 numerical S_2</i>	48
<i>Table 9 - Control parameters for H500PC</i>	49
<i>Table 10 - Control parameters for H1000PC</i>	52
<i>Table 11 - Control parameters for H1500PC</i>	53
<i>Table 12 - Control parameters overview for PC</i>	54
<i>Table 13 - Control parameters for H500FRC50</i>	57
<i>Table 14 - Control parameters for H1000FRC50</i>	59
<i>Table 15 - Control parameters for H1500FRC50</i>	60
<i>Table 16 - Control parameters for H500FRC75</i>	62
<i>Table 17 - Control parameters for H1000FRC75</i>	63
<i>Table 18 - Control parameters for H1500FRC75</i>	65
<i>Table 19 - Control parameters overview for FRC50</i>	66
<i>Table 20 – Control parameters for the FRC50 with the G_t adjusted</i>	66
<i>Table 21 - Control parameters for FRC75</i>	68
<i>Table 22 - Control parameters for the FRC75 with the G_t adjusted</i>	68
<i>Table 23 - Concrete compressive parameters inputs of Cuenca 's beams</i>	74
<i>Table 24 - Concrete tensile parameters inputs of Cuenca's beams</i>	74
<i>Table 25 - Steel tendons parameters input of Cuenca's beams</i>	74
<i>Table 26 - Control parameters for HF600/5</i>	77
<i>Table 27 - Control parameters for HF400/7</i>	78

<i>Table 28 - Control parameters for HF400h/6</i>	79
<i>Table 29 - Control parameters for HF260/9</i>	79
<i>Table 30 - Overall view for the Cuenca's pre-stressed beams</i>	79
<i>Table 31 - Compressive input data for Minelli's beams in JCONC</i>	83
<i>Table 32 - Tensile input data for Minelli's beams in JCONC</i>	83
<i>Table 33 - JCONC's results for the Minelli's FRC beams</i>	85
<i>Table 34 - Compressive input data for Cuenca's beam in JCONC</i>	88
<i>Table 35 - Tensile input data for Cuenca's beams in JCONC</i>	88
<i>Table 36 - Steel input data for Cuenca's beams in JCONC</i>	89
<i>Table 37 - JCONC's results for the Cuenca's HPFRC beams</i>	90
<i>Table 38 - Concrete properties of HPFRC</i>	94
<i>Table 39- Concrete compressive parameters inputs of Minelli's beams</i>	95
<i>Table 40 - Concrete tensile parameters inputs of Minelli's beams</i>	95
<i>Table 41 - Steel tendon parameters input of UPM's beams</i>	96
<i>Table 42 - Horizontal distributed prestressing force for UPM's beams</i>	98
<i>Table 43 - Control parameters for BMI12 for STKO Opensees</i>	99
<i>Table 44 - Control parameters for BMI12 at t_0</i>	100
<i>Table 45 - Control parameters for BMI12 at t_f</i>	100
<i>Table 46 - Control parameters for UMI12 for STKO Opensees</i>	103
<i>Table 47 - Control parameters for UMI12 at t_0</i>	104
<i>Table 48 - Control parameters for UMI12 at t_f</i>	104
<i>Table 49 - Compressive input data for UPM's beam in JCONC</i>	108
<i>Table 50 - Tensile input data for UPM's beams in JCONC</i>	108
<i>Table 51 - Steel input data for UPM's beams in JCONC</i>	108
<i>Table 52 - JCONC control parameters for BMI12</i>	108
<i>Table 53 - JCONC control parameters for UMI12</i>	109
<i>Table 54 - Comparison between MC10, EC2-draft, STKO Opensees and JCONC results for Minelli's beams</i>	112
<i>Table 55 - Statistical evaluation on result's comparison for Minelli's beams</i>	113

<i>Table 56 - Comparison between MC10, EC2-draft, STKO Opensees and JCONC results for Cuenca's beams.....</i>	<i>115</i>
<i>Table 57 - Statistical evaluation on result's comparison for Cuenca's beams</i>	<i>116</i>
<i>Table 58 - MC10, EC2-Draft, STKO and JCONC results for UPM's beams.....</i>	<i>119</i>
<i>Table 59 - Data input for the evaluation of H1000PC experimental S₁.....</i>	<i>132</i>
<i>Table 60 - Data input for the evaluation of experimental H1000PC S₂.....</i>	<i>133</i>
<i>Table 61- Data input for the evaluation of H1000PC numerical S₁.....</i>	<i>133</i>
<i>Table 62 - Data input for the evaluation of H1000PC numerical S₂.....</i>	<i>133</i>
<i>Table 63 - Data input for the evaluation of H1500 experimental S₁.....</i>	<i>134</i>
<i>Table 64 - Data input for the evaluation of experimental H1500 S₂.....</i>	<i>134</i>
<i>Table 65 - Data input for the evaluation of H1500 numerical S₁.....</i>	<i>135</i>
<i>Table 66 - Data input for the evaluation of H1500 numerical S₂.....</i>	<i>135</i>
<i>Table 67 - Data input for the evaluation of H500FRC50 experimental S₁.....</i>	<i>136</i>
<i>Table 68 - Data input for the evaluation of experimental H500FRC50 S₂.....</i>	<i>136</i>
<i>Table 69 - Data input for the evaluation of H500FRC50 numerical S₁.....</i>	<i>137</i>
<i>Table 70 - Data input for the evaluation of H500FRC50 numerical S₂.....</i>	<i>137</i>
<i>Table 71 - Data input for the evaluation of H1000FRC50 experimental S₁.....</i>	<i>138</i>
<i>Table 72 - Data input for the evaluation of experimental H1000FRC50 S₂.....</i>	<i>138</i>
<i>Table 73 - Data input for the evaluation of H1000FRC50 numerical S₁.....</i>	<i>139</i>
<i>Table 74 - Data input for the evaluation of H1000FRC50 numerical S₂.....</i>	<i>139</i>
<i>Table 75 - Data input for the evaluation of experimental H1500FRC50 S₁.....</i>	<i>140</i>
<i>Table 76 - Data input for the evaluation of experimental H1500FRC50 S₂.....</i>	<i>140</i>
<i>Table 77 - Data input for the evaluation of H1500FRC50 numerical S₁.....</i>	<i>141</i>
<i>Table 78 - Data input for the evaluation of H1500FRC50 numerical S₂.....</i>	<i>141</i>
<i>Table 79 - Data input for the evaluation of H500FRC75 experimental S₁.....</i>	<i>142</i>
<i>Table 80 - Data input for the evaluation of H500FRC75 experimental S₂.....</i>	<i>142</i>
<i>Table 81 - Data input for the evaluation of H500FRC75 numerical S₁.....</i>	<i>143</i>
<i>Table 82 - Data input for the evaluation of H500FRC75 numerical S₂.....</i>	<i>143</i>
<i>Table 83 - Data input for the evaluation of H1000FRC75 experimental S₁.....</i>	<i>144</i>

<i>Table 84 - Data input for the evaluation of H1000FRC75 experimental S_2.....</i>	<i>144</i>
<i>Table 85 - Data input for the evaluation of H1000 numerical S_1.....</i>	<i>145</i>
<i>Table 86 - Data input for the evaluation of H1000FRC75 numerical S_2.....</i>	<i>145</i>
<i>Table 87 - Data input for the evaluation of H1500FRC75 experimental S_1.....</i>	<i>146</i>
<i>Table 88 - Data input for the evaluation of H1500FRC75 experimental S_2.....</i>	<i>146</i>
<i>Table 89 - Data input for the evaluation of H1500FRC75 numerical S_1.....</i>	<i>147</i>
<i>Table 90 - Data input for the evaluation of H1500FRC75 numerical S_2.....</i>	<i>147</i>
<i>Table 91 - Data input for the evaluation of H500FRC50 numerical S_1 with G_t adjusted.....</i>	<i>148</i>
<i>Table 92 - Data input for the evaluation of H500FRC50 numerical S_2 with G_t adjusted.....</i>	<i>148</i>
<i>Table 93 - Data input for the evaluation of H1000FRC50 numerical S_1 with G_t adjusted.....</i>	<i>149</i>
<i>Table 94 - Data input for the evaluation of H1000FRC50 numerical S_2 with G_t adjusted.....</i>	<i>149</i>
<i>Table 95 - Data input for the evaluation of H1500FRC50 numerical S_1 with G_t adjusted.....</i>	<i>150</i>
<i>Table 96 - Data input for the evaluation of H1500FRC50 numerical S_2 with G_t adjusted.....</i>	<i>150</i>
<i>Table 97 - Data input for the evaluation of H500FRC75 numerical S_1 with G_t adjusted.....</i>	<i>151</i>
<i>Table 98 - Data input for the evaluation of H500FRC75 numerical S_2 with G_t adjusted.....</i>	<i>151</i>
<i>Table 99- Data input for the evaluation of H1000FRC75 numerical S_1 with G_t adjusted.....</i>	<i>152</i>
<i>Table 100 - Data input for the evaluation of H1000FRC75 numerical S_2 with G_t adjusted.....</i>	<i>152</i>
<i>Table 101 - Data input for the evaluation of H1500FRC75 numerical S_1 with G_t adjusted.....</i>	<i>153</i>
<i>Table 102 - Data input for the evaluation of H1500FRC75 numerical S_2 with G_t adjusted.....</i>	<i>153</i>
<i>Table 103 - Control parameters for H500FRC50 with G_t adjusted.....</i>	<i>154</i>
<i>Table 104 - Control parameters for H1000FRC50 with G_t adjusted.....</i>	<i>154</i>
<i>Table 105 - Control parameters for H1500FRC50 with G_t adjusted.....</i>	<i>154</i>
<i>Table 106 - Control parameters for H500FRC75 with G_t adjusted.....</i>	<i>154</i>
<i>Table 107 - Control parameters for H1000FRC50 with G_t adjusted.....</i>	<i>155</i>
<i>Table 108 - Control parameters for H1500FRC75 with G_t adjusted.....</i>	<i>155</i>
<i>Table 109 - Geometric characteristic and pre-stressing action on HF600/5.....</i>	<i>158</i>
<i>Table 110 - Geometric characteristic and pre-stressing action on HF400/7.....</i>	<i>158</i>
<i>Table 111 - Geometric characteristic and pre-stressing action on HF400h/6.....</i>	<i>159</i>
<i>Table 112 - Geometric characteristic and pre-stressing action on HF260/9.....</i>	<i>160</i>

<i>Table 113 - Geometric characteristic and pre-stressing action on BMI12 and UMI12.....</i>	<i>160</i>
<i>Table 114 - $V_{u, MC10}$ evaluation for Minelli's beams.....</i>	<i>161</i>
<i>Table 115 - $V_{u, EC2-draft}$ evaluation for Minelli's beams</i>	<i>161</i>
<i>Table 116 - $V_{u, MC10}$ evaluation for Cuenca's beams.....</i>	<i>162</i>
<i>Table 117 - $V_{u, EC2-draft}$ evaluation for Cuenca's beams.....</i>	<i>162</i>
<i>Table 118 - $V_{u, MC10}$ evaluation for UPM's beams</i>	<i>163</i>
<i>Table 119 - $V_{u, EC2-draft}$ evaluation for UPM's beams.....</i>	<i>163</i>

Introduction

Nowadays, the development of modern buildings and infrastructures requires best performing materials in terms of high strength, high toughness, and energy absorption ability.

The civil engineering industry replaces developing new advanced materials such as the High Performance Fiber Reinforced Concrete (HPFRC) which is the result of the combination of High Strength Concrete and Fibers.

Recently, the HPFRC and FRC are increasingly applied in the construction of tunnels, industrial pavements, dams and precast elements for bridges. The awareness of the FRC potentiality is growing up and this demands high research investment to provide reliable models able to represent mechanical behaviour. In particular, the adoption of FRC and HPFRC are able to mitigate the well-known brittleness in tension of concrete allowing the optimization of design and the reduction of material consumption.

The UPM structural laboratory team, partnered with Acciona S.A., has responded to the new challenges imposed by the civil engineering industry with a new HPFRC concrete mix design. In particular, the main aim of the researchers is to provide a material able to carry shear loads without transverse reinforcement in a simply supported bridge.

Furthermore, the marketability of new material requires a deep knowledge of mechanical behaviour and physical characteristics in order to be implied in the design process with a high level of reliability and safety. The material features are being detected with experimental campaigns that are going to be carried out in the Structural Laboratory. The test will be realized on 12 IPE beams with bonded and unbonded prestressing designed to fail due to shear under four points load.

The objective of this research work is to conduct Finite Element Analysis calibrations to provide a further blind prediction of UPM beams experimental behaviour at test stage. In particular, the models should detect possible complications and, at the same time, provide an estimation of the shear ultimate capacity. The predictions are fundamental for professionals to have a previous idea of structural final behaviour of the element.

The research document is organized in eight chapters. In the first Chapter a brief literature review on HPFRC and FRC is reported in order to understand the main physical variables which domain the mechanical behaviour of FRC and HPFRC beams. In Chapter 2, the reproduction of experimental results for the two sets of beams provided by Minelli et al. and E. Cuenca with *STKO OpenSees*© are reported. Afterwards, Chapter 3 presents the simulation of the previous beams' sets with another FEM software, called *JCONC*. Next, in Chapter 4, the blind predictions for UPM beams are described with *STKO OpenSees*© as well as with *JCONC* in Chapter 5. In Chapter 6 an overall comparison of numerical, experimental and analytical estimations is proposed. Finally, in the Chapter 7 and 8 the main conclusions and the future developments are detailed.

1. Literature review

1.1 Steel fiber reinforced concrete SFRC

The plane concrete is characterized by a brittle behaviour in tension due to the low tensile strength and the low strain capacity. As a consequence, a common practice is to add steel bars as reinforcement to replay the concrete tensile inefficiencies. Moreover, the use of a huge amount of reinforcement could lead to the possibility of brittle failure, due to a compression control collapse. Indeed, an uncontrolled concrete might generate crack propagation generating corrosion phenomena due to the exposure to the natural environment. The addition of randomly distributed discontinuous fibers to plane concrete is able to “bridge” cracks and provide a certain grade of ductility in the post cracking stage. As a consequence of fiber characteristics, the flexural strength, fracture toughness, thermal shock strength and resistance under impact and fatigue loadings can be improved.

Fiber reinforced concrete (FRC) is defined, according to Model Code 2010, as “*a composite material made by a cement matrix and discrete fibers. The matrix could be mortar or concrete while the fibers can be made of steel, polymers, carbon, glass or natural fibers*” [1]. The idea of adding fibers to a construction material came up in ancient times when Egyptians used horsehair to reinforce bricks. Nevertheless, the fiber reinforced concrete has become a field of research interest in the international community since the fifties with investigation of Portland Cement Associations [2]. Furthermore, the first publication is dated 1963, realized by Romualdi and Batson [3] in which the authors demonstrated the effectiveness of short fibers in reducing the brittleness of the concrete.

Different types of fibers, made by different materials, can be used in fiber reinforced concrete. Moreover, this work is focused on steel fibers since they are widely used as the preferred technical and practical solution by the design community. Several steel fibers applications and the mechanical behaviour are investigated in this work. Steel fibers are available in length between 6 and 80 mm and with a cross section area around the 0.1 and 1.5 mm² which correspond to a diameter between 0.15 and 1.2 mm. The tensile strength is commonly in a range between 300 and 2400 MPa. In the market, a large variety of shapes are available, therefore, the best performing ones are reported in Fig. 1.

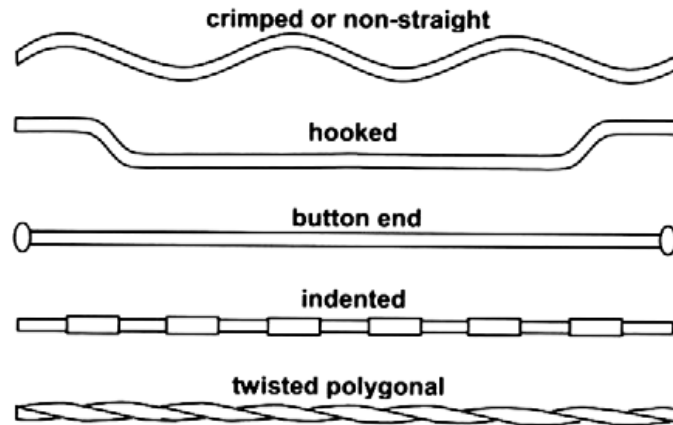


Fig. 1 - Steel fiber types [4]

The fibers are added during the concrete mixing. The main problem caused by the presence of fibers, especially if they exhibit curvilinear or irregular surfaces and complicated configuration, is the workability reduction which can be mitigated involving the use of closely configured steel fibers [5]. The fibers' parameters which affect the design and the performance of FRC are:

- V_f : fiber volume content;
- l/d : ratio between the length and the diameter of fibers;
- FWR: fiber weight ratio, defined as a weight of fiber in 1 m^3 .

In particular, the l/d ratio affects the number of fibers which cross the cracks under load, keeping constant V_f .

1.2 High performance reinforced concrete HPFRC

The development of modern building engineering and infrastructure demands high material's performance which means high strength, high toughness, and energy absorption ability. Examples of new materials are represented by High Performance Concrete (HPC) and Ultra High Performance Concrete (UHPC), capable of reaching an ultimate compressive strength between 60 and 240 MPa. The improvement of mechanical properties, as the strength, workability and durability, is allowed by the integration of supplementary cementitious materials such as silica fume (SF), ground granulated blast-furnace slag (GGBS), fly ash (FA) and the reduction of water-to-cement ratio [6]. The main properties of HPC are:

- high modulus of elasticity;
- high density and low permeability which leads in a better durability behaviour;

- low creep deformation which results in lower pre-stressed force loss [5].

Furthermore, reaching high strength has also negative impacts due to the increase of concrete brittleness which can be mitigated by the addition of fibers. The mixture which combines HPC and fibers is called High Performance Fiber Reinforced Concrete (HPFRC) or Ultra High Performance Fiber Reinforced Concrete (UHPFRC) depending on the ultimate compressive strength achieved. The distinction between the various types of fiber reinforced concrete could be based on the compressive strength range, as it is shown in Fig. 2. The FRC has less promising performance compared to the HPFRC and UHPFRC as they are implied for different fields of applications. Indeed, the FRC is cheaper than the other and it pushes the researcher to keep on investigating its behaviour because it is widely used in the community of practitioners.

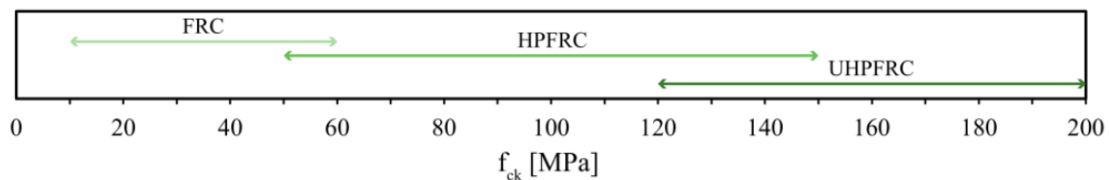


Fig. 2 - Compressive strength range for distinction between FRCs [7]

1.3 Codes in force

Despite the expected performance of those materials, the application is not so widespread due to the lack of robust international guidelines. For FRC, the turning point for structural application came in 2010 when it was recognized as a new material in Model Code 2010 [1]. Recently, new international standards have been published such as the new draft of Eurocode 02 [8] and the new version of Model Code 2020 [9] which considers the FRC and HPFRC as building materials, while UHPFRC is not mentioned. Furthermore, there are national standards such as French code NF P18 [10], Swiss code SIA 2052 [11], American code ASTM C1856 [12] and Japanese code [13] to give directions on the application of UHPFRC [7].

1.4 Mechanical properties of FRC and HPFRC

Concrete is a material released by the mix of cement, water, additives and aggregate which can have different sizes. After the concrete hardening, the final product consists of a matrix characterized by the presence of an interfacial transition zone around the surface of the mortar aggregates which is the weakest link in the concrete system and influences the material mechanical properties. As a consequence, the concrete shows a low tensile strength which results in a brittle behavior and in the cracks propagation that is absolutely inevitable in any concrete structure [14]. The fiber's addition is capable of transferring stresses between matrix and tensile strains during the crack propagation, improving the post-cracking and the material toughness. Moreover, also during the loading, the matrix is able to transfer part of the load to the fibers, which, depending on their elastic modulus and quantity, can increase the concrete strength. Consequently, the mechanical properties of material strongly depend on several factors of concrete mix design such as aggregate's size, cement type, water ratio and finally fiber's parameters [15].

1.4.1 Compressive behaviour

The compressive behaviour is characterized by a stress-strain relationship investigated with direct compression on cube or cylinder's specimens. The stress strain relationship in compression of a plain concrete commonly presents a linear branch up to the 40% of f_{ck} [8], which is the characteristic value of cylinder compressive strength, followed by a nonlinear curve until the peak value f_{ck} , at a strain of 0.002 . This is followed by a softening branch up to the ultimate concrete strain which, in general, is set equal to 0.0035 . The failure in compression appears due to the sliding on aggregate-paste interface and it propagates as tensile cracks.

The compressive behaviour of SFRC depends on the V_f and the l/d ratio. Considering a small value of V_f , it has been proved that fibers are effectively able to control the cracks formation but not greatly increase the compressive strength. Indeed, also Olivito e Zuccarello pointed out that the most important contribution of steel fiber is the changing of failure mode from fragile to ductile due to the bridging effect of fibers that is able to maintain the integrity of specimens as long as possible as shown in Fig. 3 [16]. This allows the development of higher strain deformation. As far as l/d ratio is concerned, it has been pointed out that short fibers are able to improve the concrete capacity in

compression more than the longer ones. As a consequence, there is an optimum value of l/d which allows better performance, otherwise higher values may lead to a lower strength and workability issues. Hence, the development of higher strain deformation is allowed. [17].

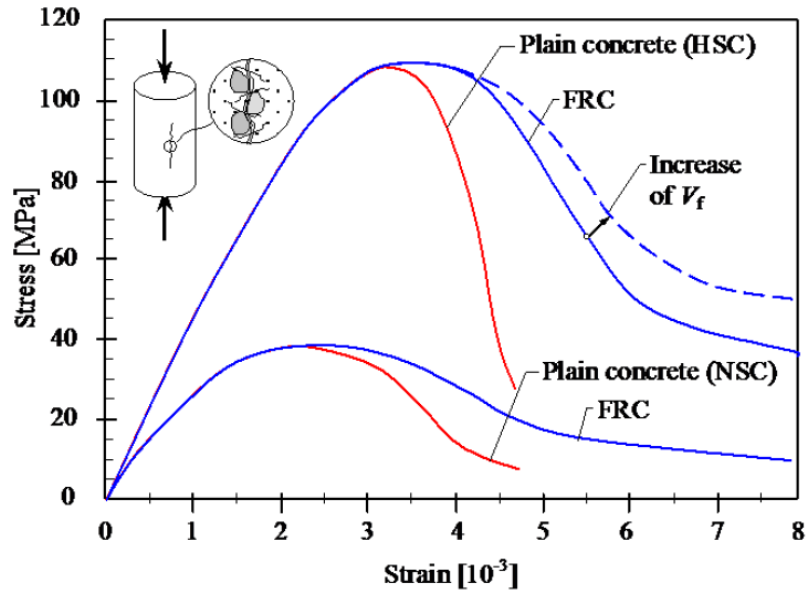


Fig. 3 - Comparison between stress - strain relationship of PC and FRC [1]

The HPFRC presents high compressive strength due to the presence of additional cementitious components. Consequently, the compressive strength improvement is mainly affected by the quantity of aggregate mixture added in the mix design such as silica fume. Despite this, as it is reported by Koksall et al. [18], the introduction of fibers inside the matrix leads to a higher compressive strength compared to the one without steel fibers if a high fiber quantity is added. On the other hand, the fibers help to mitigate the negative effect of silica fume, which introduces an elevated brittleness in the material. However, the study of Ding et al. [19] shows that adding steel fibers to HPC have no important influence in the definition of compressive peak, especially in low content.

The most important aspect both for HPFRC and SFRC is that fibers help to develop a more ductile behaviour after the reaching of the compressive peak. Thus, it is an essential key element in the nonlinear analysis and design of reinforced concrete members under compressive load.

1.4.2 Tensile behavior

The tensile strength of normal concrete is much lower than the compressive one. Under tensile load, cracks propagate faster than compressive load due to the low energy quantity needed to propagate the cracks. The embedding of fibers does not lead to a great improvement of tensile strength, f_{ct} , because the real contribution gets out after the formation of the first crack. In fact, fibers can change the tensile mode failure. Unlike plane concrete, the FRC does not fail in a brittle mode due to the transmission of stress operated by the fibers. In particular, the bond-pull out resistance is the crucial factor that dominates the tensile failure. It depends on the fiber slip, elongations and strengthening associated with three bond mechanisms: adhesion, friction and mechanical anchorage. As a consequence, the shape, the orientation respect loading direction and the aspect ratio greatly influences the *pull out* response and consequently, the overall capacity of FRC [14].

The characterization of tensile behaviour is analysed considering the stress-crack opening relationship $[\sigma - w]$ which describes the stresses carried by steel fibers across tension cracks in SFRC as a function of the crack-width/opening. This procedure was first suggested by Hillerborg et al. [20] and it is determined by experimental tests on the material. The most common tests for FRC characterization are the tensile flexural tests performed on prismatic specimens. Depending on the International Standards considered, it can be performed a three points bending test on notched specimens or four points bending test on unnotched beams as shown in Fig. 4. RILEM and other agencies have standardized the method and procedure to determine properly the $\sigma - w$ curve. Otherwise, it is also possible to perform the uniaxial tensile test although several critical issues can occur. First, fracture at the glued end faces of the specimen should be avoided using appropriate geometrical proportion, such as tapering the specimens. Second, the result of the tests can be highly influenced by eventual load eccentricities, which are hard to avoid [21].

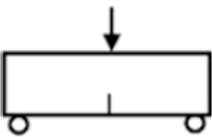
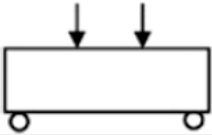
Test	Specimen size (mm)	Loading-setup	Standard
3-point bending test	600 × 150 × 150		RILEM TC 162-TDF (2002) and EN 14651:2005
4-point bending test	600 × 150 × 150		CNR-DT 204 (2006)
Uniaxial tensile test	150 Φ × 150		RILEM TC 162-TDF (2002)

Fig. 4 - Experimental tests for determination of tensile properties [14]

The SFRC $\sigma - w$ curve [Fig. 5] presents commonly a linear branch up to the ultimate tensile strength (phase1), followed by a crack formations bridged by fibers which are able to transmit tensile strength (phase 2) and enhance load capacity and, hence, the tension strength of fibers is recognized (phase 3). In HPFRC Walraven demonstrated that the fibers help heavily in the stabilization of crack formations [22].

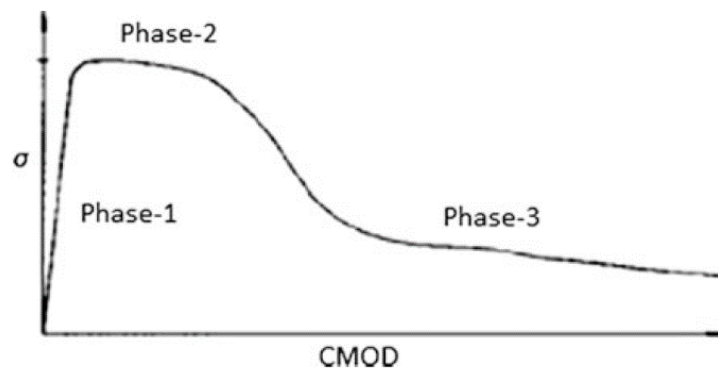


Fig. 5 - σ - CMOD relationship for a general FRC element

The area below the $\sigma - w$ curve was defined by Hillerborg as the fracture energy G_F . The tensile constitutive law is determined considering the $\sigma - w$ curve standardized by procedure proposed in international codes such as Model Code 2010 [1]. The MC210 suggests the possible adoption of two different stress-crack relationships: rigid-plastic and linear softening or hardening as shown in Fig. 6:

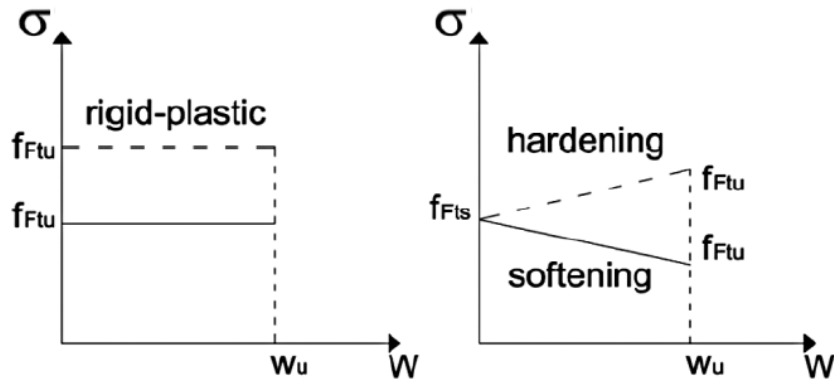


Fig. 6 - Simplified constitutive laws: stress-crack opening (solid and dashed lines refer to softening and hardening materials respectively) [fib MC2010 fig.5.6-7] [1]

where:

- w_u is the crack opening corresponding to ULS;
- f_{Fts} is the serviceability residual strength, defined as the post-cracking strength for a crack opening significant for SLS;
- f_{Ftu} is the residual strength significant for ULS.

The f_{Fts} and f_{Ftu} are evaluated using the residual flexural strength $f_{R,1}$ and $f_{R,3}$ identified in the three points bending test.

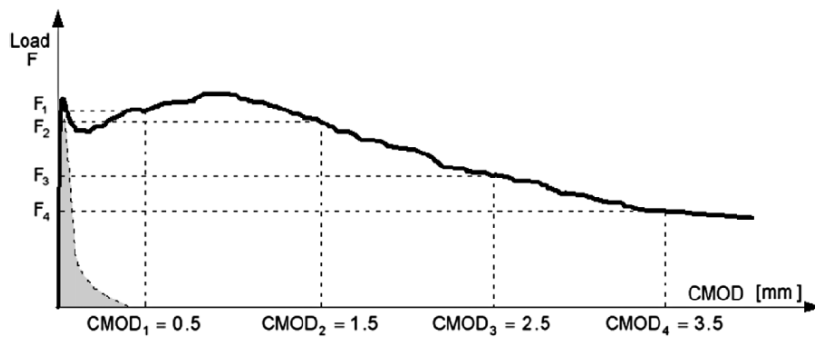


Fig. 7 - Typical load F vs. $CMOD$ curve for plain concrete and FRC [fib MC2010, Fig. 5.6-6]

Considering a typical curve, Fig. 7, the stresses at the fixed values of w_u are evaluated considering an elastic approach by the Equation (1).

$$f_{R,j} = \frac{3F_j l}{2bh_{sp}^2} \quad (1)$$

Afterwards, it is possible to calculate f_{Ftu} and f_{Ftu} performing a rotational equilibrium at ULS and a longitudinal and rotational one at SLS. The final formulations are reported below:

- Rigid-plastic model:

$$f_{Ftu} = \frac{f_{R,3}}{3} \quad (2)$$

- Linear model:

$$f_{Fts} = 0.45 f_{R,1} \quad (3)$$

$$f_{Ftu} = f_{Fts} - \frac{w_u}{CMOD_3} (f_{Fts} - 0.5f_{R,3} + 0.2f_{R1}) \geq 0 \quad (4)$$

Afterwards, the constitutive law is estimated dividing the crack opening w for the characteristic length l_{cs} which is equal to the crack spacing when multiple cracking takes place and corresponds to the beam depth when a plane section approach is used in the analysis [2].

$$\varepsilon = \frac{w}{l_{cs}} \quad (5)$$

1.4.3 Flexural behaviour

Most researchers pointed out that the inclusion of fiber in NSC and HPC resulted in an improvement of flexural strength. The main reason stays in the fiber capacity of carrying the load between the cracks interface. Indeed, the fibers allow to reduce the propagation of cracks and delay the failure of the specimen which results in an increase of load carrying capacity of concrete.

The flexural strength increases with the V_f and the l/d ratios. According to Abbass et al. [23], the flexural strength of concrete with the steel fibers content of 0.5% to 1.5% has increased from 100% to 150% for fiber with smaller l/d ratio. The concrete with 1.5% steel fibers and with higher l/d of 80 has shown an increase in the flexural strength that can reach about 150% in the high strength concrete ($w/c = 0.25$).

Moreover, considering the study of Lee et al. [24], the level of stress decreases suddenly after concrete cracking with a magnitude which depends on the fiber volume and concrete

compressive strength. This also means that the SFRCs permit to adsorb a higher amount of energy during the crack's formation that leads to an improvement of toughness.

Furthermore, the elements are able to develop higher deformation before the failure. If it is considered a Moment-Curvature diagram, it is evident that after the reaching of the first crack, the effect of tension stiffening is higher than a plain concrete as it is shown in Fig. 8. In particular, in the first stage the FRC concrete behaves in a linear elastic way since the tensile strength is not reached (Stage I). Once the first crack appears, the concrete-steel bond is activated and the tension stiffening action arises (Stage II). The tension stiffening is the ability of concrete to adsorb tension stresses across the flexural cracks. The fibers improve the bond efficiency due to the ability to also carry tension across cracks and the tension stiffening performance of the members [25]. Afterwards, the crack pattern is stabilized and the crack spacing remains constant in Stage III. Finally, the tensile average in the member exceeds the yield stresses of reinforcement bars and the FRC element behaviour is dominated by rebars and fibers (Stage IV).

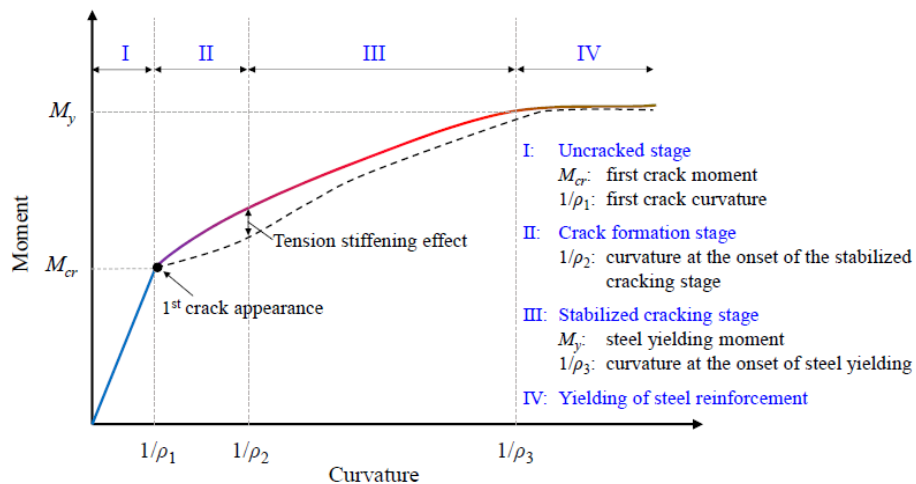


Fig. 8 - Stage of cracking and tension stiffening in SFRC members [25]

1.4.4 Shear behaviour

The shear mechanism is one of the most discussed problems in structural engineering. In transverse unreinforced concrete, the theoretical and experimental evidence shows that shear actions generate tangential stresses that, according to Mohr's circle, lead to the development of inclined principal stresses. Increasing the load, the tensile principal stress

reaches the tensile strength causing the structural cracking while the compressive principal stress is carried by the concrete portion between consecutive cracks.

The generally accepted shear mechanism for elements without stirrups is associated to a cantilever model fixed in the top compressive chord, presented in Fig. 9. The shear capacity is offered by the concrete compressive strength, the *dowel effect*, due to the presence of longitudinal reinforcement, and the aggregates interlocking action. These shear-carrying mechanisms induce tensile stresses in concrete near to the flexural crack tip and at the level of reinforcement which, once reached the ultimate tensile strength, develops diagonal cracks. However, the beams could not fail due to diagonal crack because another mechanism, called *arching action*, may arise [26]. The arching action consists of the development of compressive inclined struts in the shear span.

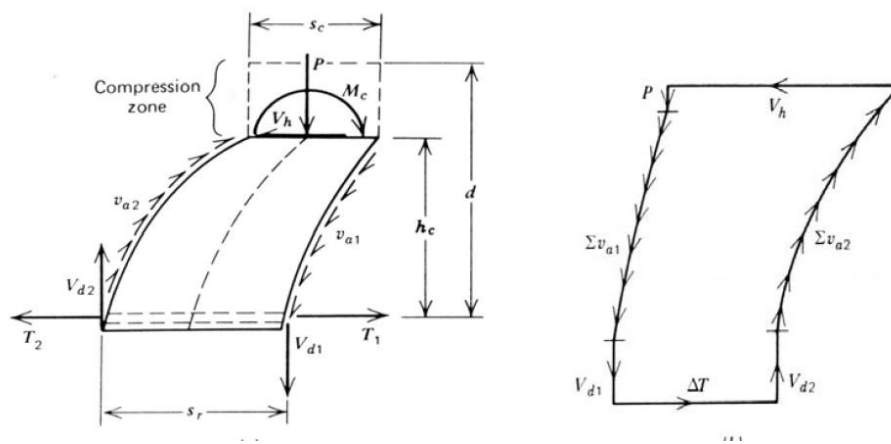


Fig. 9 - Actions on a concrete cantilever in the shear span of a beam [27]

Therefore, the capacity of the strut can be lowered by the arising of diagonal cracks. The diagonal cracks development is strictly related to the shear span - depth ratio a/d , a phenomenon known as *Kani's valley*, Fig. 10. The experiments of Kani showed that for high values of a/d ($a/d > 3$) the elements do not develop the inclined strut and the flexural capacity can be reached. For a/d values between 1 and 3, the shear cracks develop and affect the overall capacity of the element and finally, for $a/d < 1$ the flexural strength is reached again. As a consequence, the shear capacity depends on the concrete compressive and tensile strength, mix design, amount of longitudinal reinforcement and the geometry of the problem.

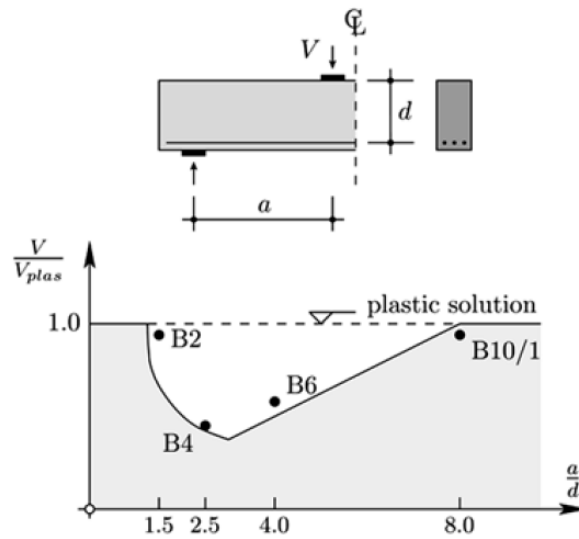


Fig. 10 - Kani's valley [26]

Traditionally, the improvement of shear capacity is realized with the introduction of transversal reinforcement realized by stirrups. The shear mechanism is analysed with truss model theory which provides a promising way to treat the problem. The compressive principal stress is carried by concrete strut while the tensile principal one is carried by stirrups. The bending moment capacity is assured by the rotational equilibrium between the compressive force in the upper part and the tensile chord in the bottom part. The stirrups also improve the aggregate interlocking effect because they control the cracking process.

Therefore, the presence of stirrups causes an increase in construction time due to the complexity of reinforcement layout and possible corrosion problem which requires adequate concrete cover and consequently an increasing consumption of material. For this reason, nowadays the researchers are investigating the possibility of replacing traditional stirrups with fibers especially for deep beams, where the shear cracks usually cause the element failure before reaching its bending moment capacity.

The steel fibers help to shift the failure pattern of structural elements from brittle shear mode to a more ductile flexural one. Compared to stirrups, the fibers have more advantages: first of all, the small size allows a more uniform distribution in the concrete matrix which improves the bridging effect over the crack and as a consequence the interlocking effects. Secondly, the fibers improve the tensile strength enhancing the shear capacity of the structural element. Despite the promising performance of steel fiber

reinforced concrete, there are limited published research efforts on the problem. These works have demonstrated the improvement of shear capacity and ductility in deep beams.

However, there are still open questions about the optimum fiber dosage to avoid the stirrups' presence and the interaction between stirrups ratio and fiber quantity. Meda et al. [28] performed experimental tests on full scale fiber reinforced prestressed beams to compare beams made with transverse reinforcement and with a low volume fraction ($V_f = 0.64\%$) to evaluate the possibility of substituting stirrups with fibers. The results showed that the beams reinforced with fibers had a similar or better post cracking behaviour respect to the ones with the minimum transverse reinforcement.

Furthermore, considering the study realized by J. A. Torres et al. [29], the introduction of 1.2% fiber content changes the failure mode from shear to shear-flexural cracks. However, they demonstrated that fibers do not affect the arching action. Nevertheless, when the inclined cracking load is considered, the effect of adding steel fibers is important. Using a higher fiber content, a higher inclined cracking load is reached with an increase of 24% in shear capacity for a fiber volume fraction increasing from 0.0% to 1.2%. Besides this, Minelli et al. [30] demonstrated that presence of fibers can mitigate the size effect in deep beams.

Afterwards, Dang et al. [31] tested 12 deep beams with different fiber content and stirrup ratios. The results showed that there was an enhancement in shear cracking (up to 30%), shear loading capacity (up to 55%) and deformation capacity (up to 45%). Indeed, there was a decrease in average crack width (up to 11 times) and in the displacement of the beam (up to 13 times).

Nevertheless, as far as HPFRC shear behavior is concerned, the few available research results show that the presence of steel fiber in the mixture can improve the shear capacity of beams. The experimental campaign carried out by W. Pansuk et al. on six I-beams with different fiber content and shear reinforcement pointed out that when V_f increased from 0 to 0.8% and from 0 to 1.6%, the shear strength increased from 90.7 kN to 340 kN and 531 kN, respectively, which is equivalent to increases of 275% and 485%, respectively [32].

2.FEA: numerical representation of experimental results with *STKO Opensees*©

2.1 Introduction on Finite Element Method FEM

In the science of construction, the availability of closed-form solutions exists only for small clusters of problems which present a high geometrical regularity and load conditions. However, the practical problems present a complexity that requires approximate solutions solved by numerical methods [33]. Since the sixties, the most used numerical technique is the Finite Element Method (FEM), especially in structural engineering applications. The FEM has become the most implemented technique in commercial software for structural analysis. Basically, the finite element method is a numerical technique able to solve partial differential equations with the discretization of the space dimensions into finite elements: in this way it creates a spatial domain with finite elements of points. Hence, the method approximates the unknown function over the domain.

Commonly, the commercial software considers, as an unknown function, the displacement: this type of analysis is called the *Displacement Based Finite Element Procedure (DBFE)*. The main steps which the software follows are:

1. assuming a polynomial displacement function based on the independent degrees of freedom;
2. evaluating of strain function from the application of compatibility relationships;
3. evaluating the stresses considering the material constitutive law;
4. applying the *Principle of Virtual Works* for the evaluation of nodal force and displacement.

Clearly, the method requires a series of approximations. First of all, the chosen displacement function could not satisfy the requirement of continuity between adjacent elements and, consequently, the compatibility conditions may be violated. Second, concentrating the equivalent forces at nodes, equilibrium conditions are fulfilled in

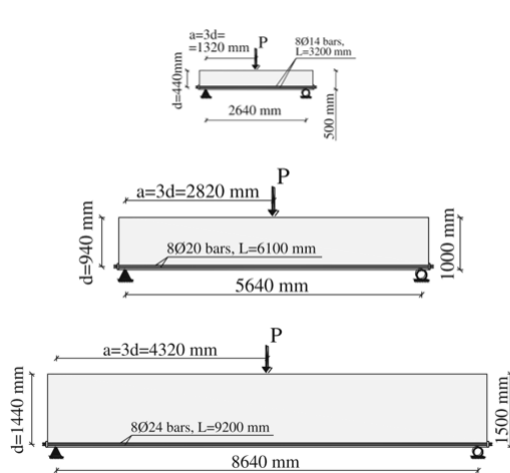
overall sense only. Hence, local violation of equilibrium conditions within each element and on its boundary could arise [34].

As a consequence, the method provides approximate solutions which must be carefully evaluated by structural engineers.

2.2 Case study 1: Minelli's experimentations

The first beams' set modeled is composed of the beams tested by Minelli et al. at the University of Brescia [30]. The aim of the experimentations consisted of investigating the effect of steel fibers on key parameters which domain the shear response of concrete members.

Nine full scale beams were tested under three points bending test and a shear-depth ratio a/d equal to 3. The beams were made by different amounts of fibers: 0, 50 and 75 kg/m³. For each type of concrete, they casted three beams with different heights: 500 (H500), 1000 (H1000), 1500 (H1500) mm and a thickness equal to 250 mm. The distance between the bottom fiber and the rebars' centroid is equal to 60 mm and, consequently, the effective depths are 440, 940 and 1440 mm. In Fig. 11, there are reported the geometry characteristics of specimens.



Beams	H500	H1000	H1500
Height (mm)	500	1000	1,500
Effective depth d (mm)	440	940	1,440
Total length (mm)	3,000	5,900	9,000
Span (mm)	2640	5640	8,640
Shear span a (mm)	1,320	2,820	4,320
Width (mm)	250	250	250
Bottom to rebar centroid distance d' (mm)	60	60	60
Reinforcement longitudinal bars	8Ø14	8Ø20	8Ø24
Reinforcement area (mm ²)	1,232	2,513	3,619
Reinforcement ratio	1.12 %	1.07 %	1.01 %

Fig. 11 - Geometric characteristics of Minelli's specimens [30]

The longitudinal reinforcement layout is realized by two levels of four rebars for a total amount of 8 bars which are $\phi 14$ for the H500, $\phi 20$ for the H1000 and $\phi 24$ for the H1500. The bars are anchored at the end by two steel plates.

The three concrete types are called “PC” for the one with no fibers, “FRC50” for a fiber content of 50 kg/m³ and “FRC75” for a fiber content of 75 kg/m³.

Beams	PC	FRC50	FRC75
Fibres V_f (%)	0.00	0.64	1.00
f_{cm} (MPa)	38.7	32.1	33.1
f_{ctm} (MPa)	3.0	2.4	2.5
E_{cm} (MPa)	33,500	30,800	32,100
$f_{R,1}$ (MPa)	–	5.4	6.0
$f_{R,2}$ (MPa)	–	5.6	6.1
$f_{R,3}$ (MPa)	–	5.0	6.0
$f_{R,4}$ (MPa)	–	4.5	5.5

Fig. 12 - Concrete mechanical properties of Minelli's beams [30]

The concrete is a normal strength concrete, having a target characteristic strength, f_{ck} , of 30 MPa. In Fig. 12, we found the mechanical characteristics of the concrete: there are reported the mean values of compressive and tensile strengths f_{cm} and f_{ctm} , the Young's Modulus as well as the residual flexural strength $f_{R,1}$, $f_{R,2}$, $f_{R,3}$, $f_{R,4}$. Actually, the authors did not detail how they evaluated the compressive characteristics while for the tensile properties they performed a material characterization with three points bending test on notched prismatic beams.

The yielding and tensile ultimate strength of longitudinal rebars are: 506 and 599 MPa for $\phi 14$ bars, 555 and 651 MPa for $\phi 20$ bars, 518 and 612 MPa for $\phi 24$.

The load is applied by means of electro-mechanical screw jack with a power of 500 kN for H500 and 1500 kN for H1000 and H1500 on a steel plate. Moreover, the supports can be represented by a roller and a pin, set on steel plates.

2.2.1 FEM modelling strategies

The software used for the numerical models is *STKO Opensees*© developed by ASDEA software [35]. The *Scientific ToolKit for OpenSees*, aka STKO, is an advanced Graphical User Interface (GUI) for *OpenSees*©.

The software includes two modules: Preprocessor and Postprocessor. In the Preprocessor the geometry, the physical and elements properties, the interaction between different elements, the boundary conditions, the mesh and the analysis commands are defined. In *STKO* there is not the possibility of setting measure's units and for this reason the user must be consistent. The unit chosen for geometry is *millimeters* while it is *Newton* for the load.

In this section, the different tasks used to generate the FE model are described. The models are set in order to develop a 2D static analysis.

2.2.1.1 Geometry

The geometry is reproduced easily due to the GUI. In particular, before assigning the physical properties, the geometry is just a CAD draw without any physical meaning. The body of beams and the steel plates for the supports and the anchorage have been realized by the command *Face4* which generates a surface and subsequently combined with the command *Merge* to create one element. The reinforcement is represented as an equivalent unique bar with an area equal to the total amount of reinforcement, drawn by a *Line*. The steel plates dimensions have been obtained directly from the picture reported in the reference as they are not detailed by the authors. In particular, the plates have dimensions equal to 150x30x250 mm. The creation of geometry was carefully evaluated to avoid the creation of mesh irregularities as shown in Fig. 13.

2.2.1.2 Interaction

The interaction modelling defines the links between nodes or elements in order to simulate the relationship between different elements. In these models, the interactions are used to assign the bond between rebars and concrete and the anchorage between the bars and the steel plate. In particular, the interaction assigned for both of the links needed is a *Node To Element links*. This type of interaction generates $N (M-1)$ - node master - slave links, where N is the number of slave nodes. Each node of the slave geometry is coupled

with the M nodes of the closest element of the master geometry. Furthermore, in the definition of links for the bonding, the master geometry is the concrete while the slave is the bars and for the anchorage links the master geometry was the extreme point of the rebar and the slave the points of the steel plate. In Fig. 13 the interactions are plotted in pink.

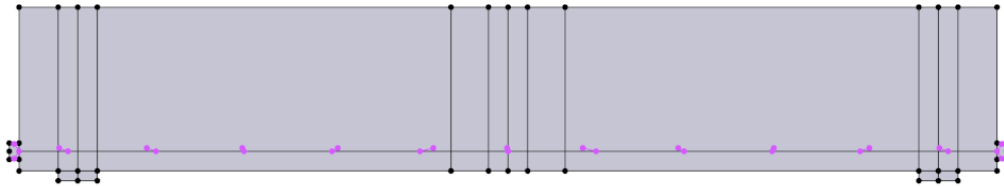


Fig. 13 - Beam geometry in STKO OpenSees for Minelli's beam

2.2.1.3 Physical properties

In the section Physical properties, the material, the section characteristics and the special purpose for the elements are reported.

- Material properties for concrete

The concrete material is defined using the *DamageTC3d* [36] model implemented in *STKO OpenSees*®. This model defines the tensile and the compressive behavior, the damage evolution and the failure criteria.

The compressive uniaxial law is determined setting several parameters:

- E : is the elastic modulus provided by authors;
- ν : is the Poisson Ratio set equal to 0.2, according to MC2010 [1];
- f_{c0} : is the elastic limit for concrete that is setting equal to 40% of f_{cm} - according to Eurocode 02 [8];
- f_{cm} : is the peak strength equal to the f_{cm} provided by the authors and reported in Fig. 12;
- f_{cr} : is the residual strength equal to 20% of f_{cm} - according to Yu et al. [37];
- ϵ_p : is the strain at peak load equal to 0.002 - according to Eurocode 02 [8].
- G_c : is the compressive fracture energy evaluated as (6), according to [38], where G_f is the tensile fracture energy provided by the MC2010 and evaluated as (7) [1].

$$G_c = 250 \cdot G_f \quad (6)$$

In Table 1, the values used for the different types of concrete are reported.

Table 1- Concrete compressive parameters inputs of Minelli's beams

Concrete type	E [MPa]	f_{c0} [MPa]	f_{cp} [MPa]	f_{cr} [MPa]	G_c [N/mm]
PC	33500	15.5	38.7	7.7	35
FRC50	30800	12.8	32.1	6.4	34
FRC75	32100	13.2	33.1	6.6	34

The uniaxial law is reported in Fig. 14.

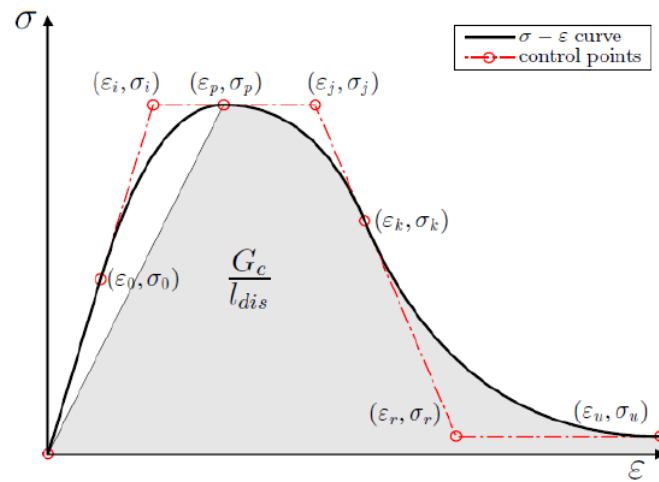


Fig. 14 - Concrete stress-strain relationship in compression for STKO Opensees

The tensile behavior is defined by a linear branch until the ultimate tensile stress admissible, afterwards it is described by a nonlinear branch as shown in Fig. 15. The area below the curve is the fracture energy G_f divided by the critical length l_{cs} which is assumed equal to the mesh size.

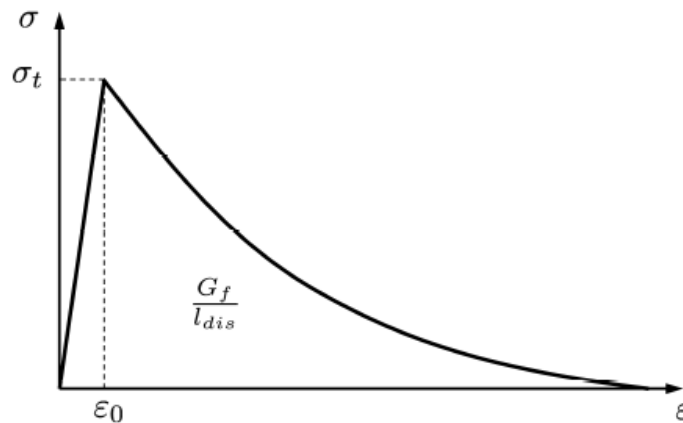


Fig. 15 - Concrete stress-strain relationship in tension for STKO Opensees

The parameter used for the calibration of tensile behavior are:

- f_t : uniaxial tensile strength, equal to the 2/3 of the f_{ctm} , reported in Fig. 12;
- G_t : tensile fracture energy.

The tensile fracture energy G_t has been evaluated differently for the normal concrete and the fiber reinforced one. In particular, for the first it has been set as the MC2010 recommends (7):

$$G_t = 73 \cdot f_{cm}^{0.18} \quad (7)$$

For fiber reinforced concrete, the MC2010 allows the adoption of two possible $\sigma - w$ diagrams: linear softening or hardening and constant as reported in § 1.4.2. In this modelling, the constant diagram has been applied as it is shown in Fig. 16.

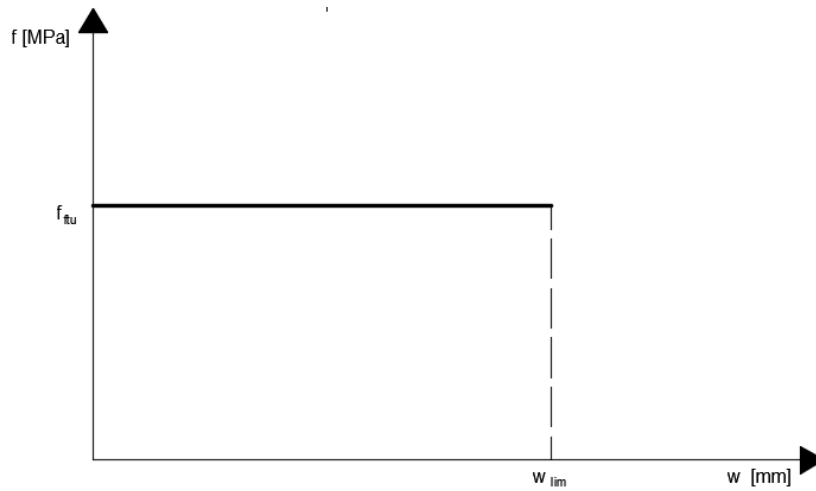


Fig. 16 - Stress - crack opening displacement chosen for FRC50 and FRC75

The stress tension f_{Ftu} is evaluated as 1/3 of $f_{R,3}$ (2) while the maximum crack width w_{lim} is set equal to 2.5 mm as MC2010 [1] recommends. Finally, by fixing the values which define the $\sigma - w$ law, it has been possible to evaluate the G_t as the area under the curve. In Table 2, f_t , f_{Ftu} and G_t for each material are reported.

Table 2 – Concrete tensile parameters inputs of Minelli's beams

Concrete type	f_t [MPa]	f_{Ftu} [MPa]	G_t [N/mm]
PC	2.00	-	0.14
FRC75	1.60	1.67	4.20
FRC75	1.67	2.00	5.00

The nonlinearity of the problem requires the adoption of a damage model for the concrete to reproduce the shear response. The damage model is defined by two parameters d^+/d^- based on continuous model put forward by Cervera et al. [39] and it defines the tensor of the stresses as (8):

$$\sigma = (1 - d^+) \bar{\sigma}^+ + (1 - d^-) \bar{\sigma}^- \quad (8)$$

where $\bar{\sigma}$ is the elastic stresses tensor (9):

$$\bar{\sigma} = C : \varepsilon \quad (9)$$

The d^+ and d^- are the damage index in tension and in compression and they influence the evaluation of positive and negative components of the stresses' tensor. The d^+/d^- are scalar values which can vary from 0 to 1, respectively when the concrete is intact or completely damaged [36].

Besides the damage index, the model also introduces two compressive and tensile damage thresholds τ^+ and τ^- as (10 - (13):

$$\tau^- = \frac{1}{1 - \alpha} \left(\alpha \bar{I}_1 + \sqrt{3 \bar{J}_2} + k_1 \beta \langle \bar{\sigma}_{max} \rangle \right) \quad (10)$$

$$\alpha = \frac{k_b - 1}{2k_b - 1} \quad (11)$$

$$\beta = \frac{f_{cp}}{f_t} (1 - \alpha) - (1 + \alpha) \quad (12)$$

where:

- \bar{I}_1 : is the first invariant of the stresses tensor;
- \bar{J}_2 : is the second invariant of tensor deviation;
- $\bar{\sigma}_{max}$: is the maximum principal stress;
- k_1 : is a parameter related to the influence criteria on the model dilatant behaviour;
- k_b : is the ratio of the bi-axial strength to the uniaxial strength in compression.

$$\tau^+ = \frac{1}{1 - \alpha} \left(\alpha \bar{I}_1 + \sqrt{3 \bar{J}_2} + k_1 \beta \langle \bar{\sigma}_{max} \rangle \right) \frac{f_t}{f_{cp}} \quad (13)$$

Once evaluated the τ^+ / τ the failure surface is individuated Fig. 17.

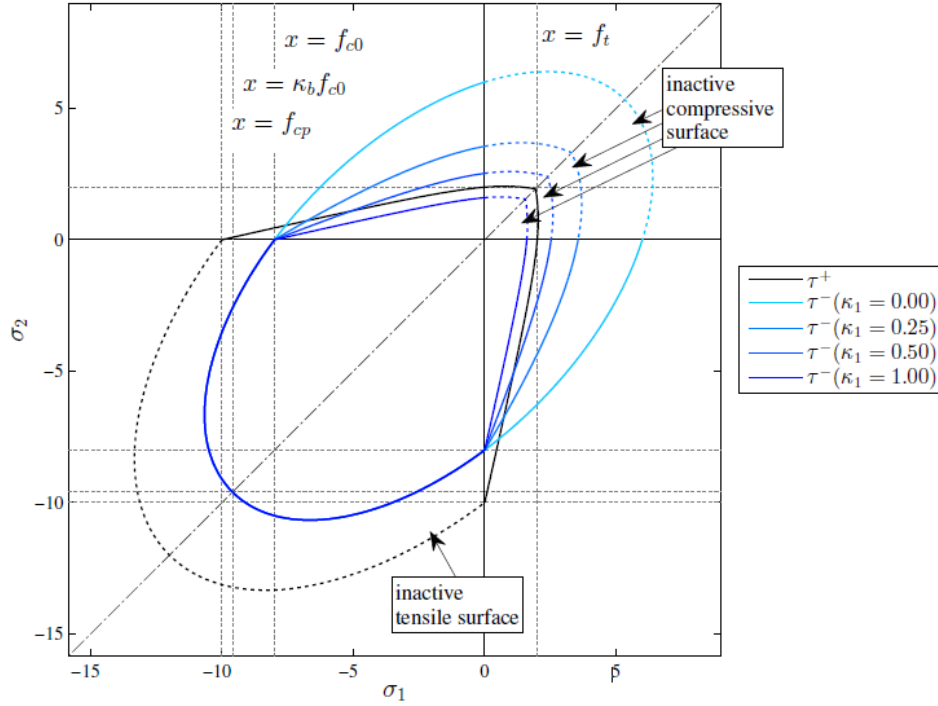


Fig. 17 - Damage surface for the plane stress case [36]

The damage index d^+ / d^- are evaluated based on the concrete stress-strain relationship in compression and in tension previously explained. In particular, the analytic formula for d^+ and d^- are (14)-(15):

$$d^+(r^+) = 1 + \frac{r_0^+}{r_0^-} \exp \left\{ \frac{2H_{dis}(r_0^+ - r^+)}{r_0^+} \right\} \quad (14)$$

$$d^-(r^-) = 1 - \frac{\Sigma(\xi)}{r^-} \quad (15)$$

where:

- H_{dis} : softening parameter
- r^+ : is the tensile damage index which accounts the irreversibility of the damage
- r_0^+ : is the threshold initial damage
- r^- : is equal to f_t ;
- r_0^- : is equal to f_{c0} ;
- Σ : is the hardening variable
- ξ : is the strain-like counterpart

The model uses the IMPLEX algorithm to improve the numerical stability of the analysis. The resulting response is stepwise linear with a positive-definite tangent stiffness matrix due to the explicit extrapolation of the internal variables.

- Material properties for reinforcement's steel

The stress-strain relationship of the steel has been modelled with the material model *Steel01* which considers an elastoplastic law. The parameters inputs are the yielding stress f_y and the elastic modulus E. In Table 3 the value for each bars' diameter is reported.

Table 3 - Steel reinforcement parameters input of Minelli's beams

Type of bars	E [MPa]	f_y [MPa]
$\phi 14$	210000	506
$\phi 20$	210000	555
$\phi 24$	210000	518

- Material properties for plates' steel

The steel plates role is the distribution of forces, avoiding the concentration of stresses which generates singularities in the models. For this reason, they are modelled as elastic isotropic material by the command *ElastoIsotropic* with an E equal to 210 GPa and ν to 0.3.

- Rebars section

The rebars section has been created with the command *sections>Fibers* which allows the creation of a general shaped section and the assignment of the material property which, in this case, is the steel for reinforcement. In particular, the sections are discretized in fibers with a triangular shape. The dimension of mesh size for the discretization depends on the cross section dimension in order to perform a correct approximation.

- Special purpose for Physical Properties

In *STKO Opensees*© is not allowed to assign more physical properties to an element because a property assignment overwrites the previous one. After creating more physical properties such as sections, materials etc. it is possible to create a special purpose. In the Minelli's models, a special purpose for the rebars with the command *truss* has been

created because the aim was to create subsequently an 1D Finite Element. In Fig. 18 the physical properties are individuated by different colours.

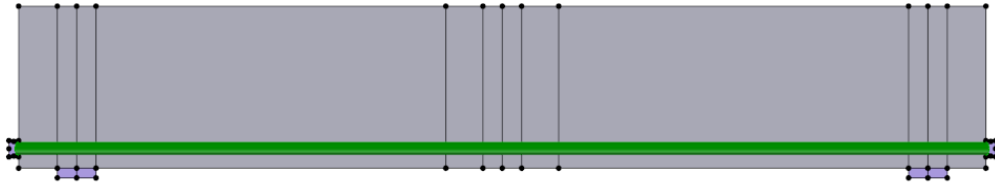


Fig. 18 - Physical properties in STKO Opensees for Minelli's beams

2.2.1.4 Element properties

The Finite Element chosen for the beam is a Shell which has 2D dimensions. The command selected is *quad* which is composed by a unique 2D element made by four nodes located at the four geometric corners of the quadrangle as it is shown in Fig. 19. The *quad* command uses a bilinear isoparametric formulation which refers that the same function is used to define the element geometry and the displacement within the elements. The Gauss points are four in the single FE. As a 2D element for an 2D analysis, the plate is able to carry 2 normal stresses (σ_{11} and σ_{22}) and a tangential one (σ_{12}). The local axes have the origins in the centroid of the element and they are directed according to the global reference system.

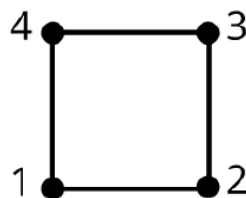


Fig. 19 - Quadrilateral Type with 4 nodes

The Finite Element assigned at rebars is a 1D element. The command used is *truss* which is a linear type defined by two nodes at each extremity of the line, as it is shown in Fig. 20. The element develops one Gauss Point in each centroid of the section fiber. The element is able to carry only the normal stresses directed along its axis. The local reference system is directed as the global one.



Fig. 20 - Linear type with 2 nodes

2.2.1.5 Conditions

Under the folder *Condition*, the constraints, the restraints and the load have been defined.

- Restraints

The restraint conditions are a pin and a roller at the supports. To assign the restraints *Condition* > *New Condition* > *Constraints* > *sp* > *fix* have been selected. In the *fix* section the displacement in y and x direction, U_y and U_x , have been ticked for the pin in order not to allow them while for the roller only the U_y has been selected.

- Constrains

The constraint conditions have been defined for the bond between concrete and reinforcement and for the anchorage of bars. In the first case, a multi-points constraint called *ASDEEmbeddedNodeElement* has been used. It constrains the displacements of the constrained node (NC) to be the weighted average of the displacements of the surrounding retained nodes (NRi). The same is done with the infinitesimal rotation, if the constrained node has rotational DOFs. The constraint is imposed using the penalty approach, imposing a penalty stiffness value to enforce the constraint. This value should be large enough to enforce the constraint, but not too large, otherwise the system may become ill-conditioned. In these models, the value is assumed equal to 1E06 in order not to allow the bar's slipping and, at the same time, avoid numerical instabilities.

Finally, the constraint between steel plate and bars is given using the command *edof*: selecting the U_y , U_x and R_z the plate's nodes move as the rebar's ones. In this way, the plate, which is contrasted by the concrete, gives the anchorage action.

- Load

The load is applied as distributed on a length equal to the plate width (120 mm) with the command *EdgeForce*. The choice of distributing load is done to avoid the modelling of the material presented during experimentations at the interface between plate and beams which allows the plate's sliding. This aspect is important to avoid the concentration of stresses under the loading zone and numerical instabilities.

In Fig. 21, the restraints and constrains are indicated with dots while the load with arrows.

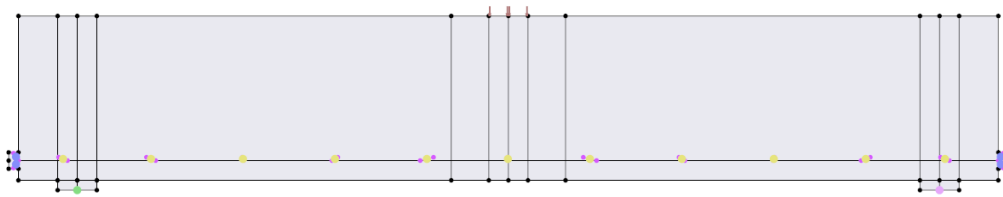


Fig. 21 - Conditions for Minelli's beams in STKO Opensees

2.2.1.6 Analysis steps

Under the menu Analysis steps, the steps which the analysis follows chronologically are defined and, for this reason, it is important to set them in the proper order.

- Recorder

The first element which must be set is the *MPCRecorder*, inside the menu *Recorders*. In this section it is possible to choose the nodal and the element results which is needed to record. To evaluate the shear behaviour and make a comparison between the numerical and experimental results, the following has been recorded:

- the nodal displacement;
- the reaction force;
- the material stresses;
- the materials strain;
- the material damage;
- the section fiber stress;
- the section fiber strain.

- Patterns

In the *patterns* menu, it is possible to add a load pattern and a constraints pattern which assign respectively load and constraint conditions.

In particular, firstly the boundary conditions have been added, imposing two single point conditions (pin and roller) and two multi-points conditions (*ASDEmbeddedNodeElement* and *edof*). Subsequently, the load condition has been given, assigning a linear time series previously defined in the section *definitions*.

- Analyses

The analysis features are set in the *AnalysesCommand* which allows the user to define the different linear and nonlinear available analysis tools. For each analysis, the following options have been defined:

- *Analysis type command*: this command is used to construct the analysis object which is a static analysis;
- *Constrain command*: it determines how the constraint equations are enforced in the analysis. In these models, a *PenaltyMethod* with default penalty values has been set;
- *Numberer Command*: it is used to construct the mapping between equation numbers and degrees-of-freedom. It has been set on *Parallel Reverse Cuthill-McKee Numberer* because the analysis is splitted in more than one processor;
- *System Command*: it is used to construct the *LinearSolver* objects to store and solve the system of equations. In these models, it has been set on *Mumps*;
- *Algorithm Command*: it defines the sequence of steps taken to solve the nonlinear equation and the *Krylov-Newton Algorithm* has been adopted;
- *Test Command*: it is used to build a *ConvergenceTest* object. It is set on the *Norm Displacement Increment* which uses the norm of the right hand side of the matrix equation to determine if convergence has been reached;
- *Integrator Command*: it defines the *IntegratorObject* which is a *Parallel Displacement Control* and it means that the analysis proceeds by increasing the displacement. The displacement is imposed to the mid span point, previously defined in a *SelectionSet*. According to the choice of 2D analysis, the point has two degrees of freedom;
- *Analyze*: it defines the number of analysis steps to perform. In this case, the *Adaptive Time Step* has been chosen which tries to adapt the time step size based on the convergence properties of the problem.

2.2.1.7 Meshing

The mesh has been created by the command *GlobalSeed* in which the type of divisions is possible to choose: in these models the elements have been divided creating a uniform mesh size of 25 mm. By using the *MeshControlCommand*, a structured quadrilateral mesh has been generated to obtain a uniform pattern for the 4-sided surface. Furthermore, an

analysis with lower mesh size of 10 mm has been carried out to assess the mesh sensitivity. The analysis showed negligible differences between them and as a consequence the mesh size does not affect the numerical prediction. Moreover, the *MeshControlCommand* allows to decide the polynomial order for the shape function which is set equal to one, setting a linear function for all the beams. However, some tests have been carried out setting the quadratic function in order to verify if the previous assumption provided stable results. The analysis has shown a negligible improvement of approximation and, finally, the first order has been kept for all the analyses, reducing the computational cost.

Finally, the models have been partitioned in several undermodels, according to the dimension and the computational cost of the beams, using the command *MeshPartition*. Hence, a multiprocessor analysis is carried out, reducing the time analysis and the computational cost.

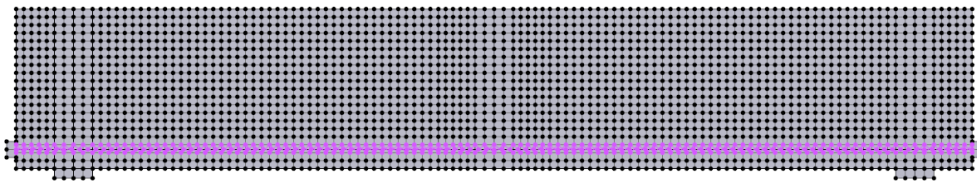


Fig. 22 - Mesh plot for Minelli's beams in STKO OpenSees

2.2.2 Plane Reinforced Concrete: result and discussion

The behavior of the three beams are expressed by load-displacement ($P-\delta$) curves. As it was expected, the three beams reached the failure due to shear action as the ultimate bending moment midspan M_{fl} , provided by authors, is higher than the M_{exp} developed during the experimentations as it is shown in Table 4.

Table 4 - Comparison between the M_{exp} and M_{fl}

ID	M_{fl} [kNm]	M_{exp} [kNm]
H500PC	254	153
H1000PC	1210	529
H1500PC	2511	911

Awareness of the beams real behaviour has required a careful examination of the experimental results and numerical prediction through the definition of some control

parameters which have been evaluated from experimental and numerical results and manual checking:

- P_{cr} : first cracking load;
- P_u : ultimate load at the peak;
- δ : displacement at peak load;
- S_1 : linear branch slope;
- S_2 : nonlinear branch slope.

The P_{cr} represents the value at which the first crack appears. It has been evaluated manually according to *Bernoulli - Navier* formulations (16) and the well-known formulation for the midspan Moment in the three points bending test (17).

$$M_{cr} = \frac{f_{ctm}}{y} \cdot I \quad (16)$$

$$P_{cr} = \frac{4 \cdot M_{cr}}{l} \quad (17)$$

The experimental P_{cr} has been caught directly from the curve as the load corresponds to a great change of stiffness. The numerical value has been evaluated from the *Postprocessor*, considering the one at which the first damage appears in the *GaussPlot*.

The P_u represents the failure load. The experimental value has been considered as the maximum load provided by the P- δ curve reported in the references and accurately digitized while the numerical one is the peak of the predicted P- δ curve.

The displacement at peak point δ corresponds to the displacement reached at the maximum load value for both numerical and experimental curves.

The linear branch slope is evaluated as the secant (18) between the point A and B which corresponds to the curve's origin and the cracking load P_{cr} .

$$S_1 = \frac{y_B - y_A}{x_B - x_A} \quad (18)$$

The nonlinear branch slope is evaluated in correspondence of the curve tangent at the M displacement point. The middle point between the C and the D, which are P_2 and P_u . P_2 represents the numerical predicted load at which the mid span flexural crack starts to go

deeply in the beam height. This value is useful for the evaluation of nonlinear slope. Hence, the importance of considering the inclination of the different branches is related to the stiffness changing according to the propagation of damage.

2.2.2.1 H500PC

In this section, the evaluation of control parameters for the H500PC is reported. In Table 5, Table 6, Table 7 and Table 8, there are the points used to calculate S_1 and S_2 and in Fig. 23 and Fig. 24 both linear branch secant and the nonlinear branch tangent are plotted.

- Experimental curve:

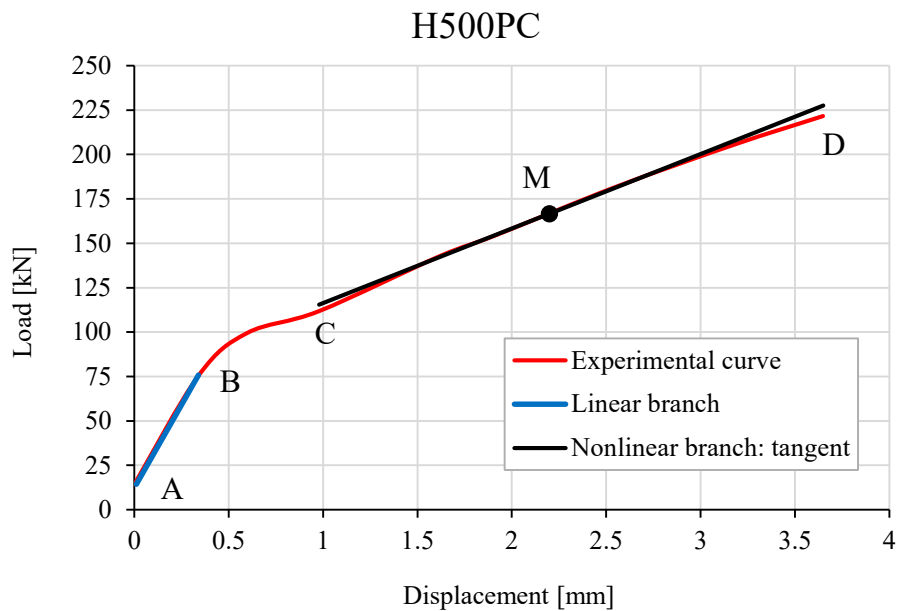


Fig. 23 - Experimental H500PC load-displacement curve with control parameters

Table 5 - Data input for the evaluation of H500 experimental S_1

Points	x	y
Point A	0.01	14.4
Point B	0.34	75.9
Slope S_1		187

Table 6 - Data input for the evaluation of experimental H500 S₂

Points	x	y
Point C	0.98	110
Point D	3.65	221.5
Point M	2.20	166.65
Slope S ₂		42

– Numerical curve:

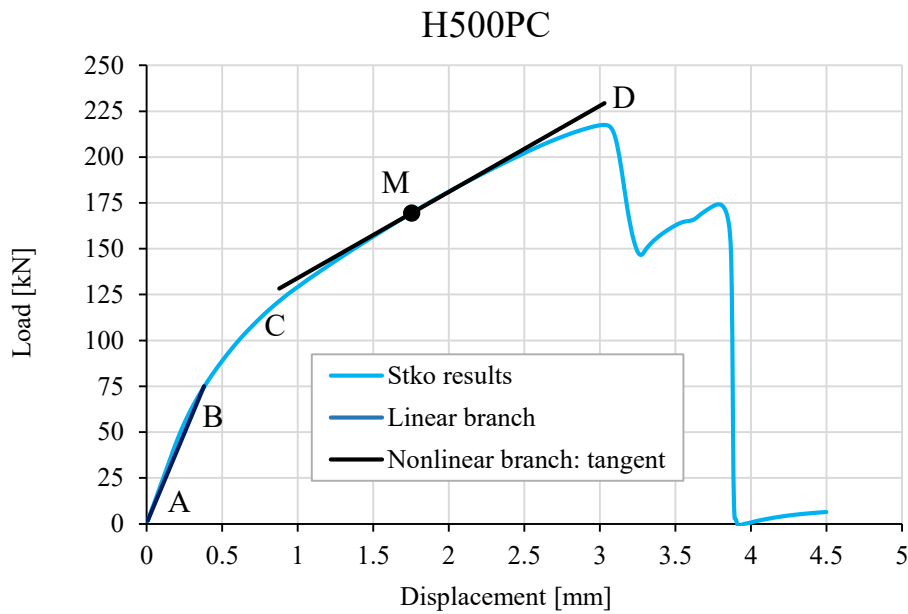


Fig. 24 - Numerical H500PC load-displacement curve with control parameters

Table 7 - Data input for the evaluation of H500 numerical S₁

Points	x	y
Point A	0	1.70
Point B	0.38	75
Slope S ₁		187

Table 8 - Data input for the evaluation of H500 numerical S₂

Points	x	y
Point C	0.88	121.45
Point D	3.03	217.5
Point M	1.76	169.4
Slope S ₂		47

In Table 9, the main evaluation for the H500PC are reported. The P_u manually evaluated is the value calculated by Minelli et al. with the formulations proposed by the authors.

Table 9 - Control parameters for H500PC

H500PC	P_{cr} [kN]	P_u [kN]	δ [mm]	S_1 [-]	S_2 [-]
Experimental results	75	224	3.70	187	43
STKO predictions	41	218	3.03	197	47
Manual evaluations	47	224	-	-	-
STKO predictions/Experimental results	0.55	0.97	0.82	1.05	1.09
Manual evaluation/Experimental results	0.63	1.00	-	-	-

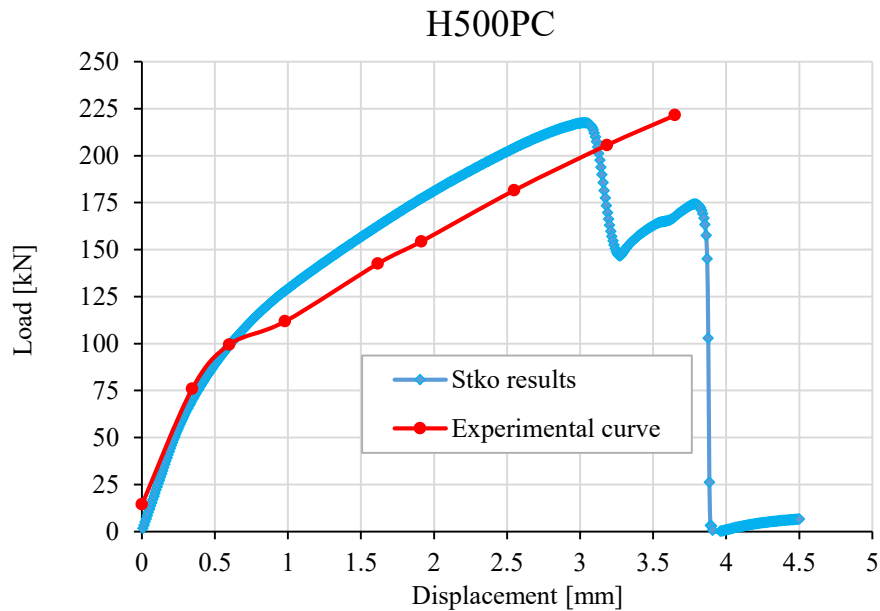


Fig. 25 - Comparison between numerical and experimental load - displacement curve for H500PC

Considering the comparison between the numerical and experimental ultimate load-displacement curve in Fig. 25, there is a good agreement between them. Therefore, also Table 9 shows that the P_u predicted is very close to the experimental value, with an error of 3%, and the stiffness in the linear and nonlinear stage is quite the same considering that there is an error of 5% and 9%. Moreover, there are differences in the stiffness evolution due to the damage development and, consequently, the curve presented an ultimate displacement lower than the experimental one, with an error of 12%. Particular attention has been given to the shape of the experimental and numerical P - δ curves in order to better detect the real failure mechanism and the reason for the presence of different branch slopes, assessing the reliability of numerical results.

As it is possible to observe from Fig. 25, in the experimental curve of the beam H500PC there is no great slope change up to 75 kN. Assuming the Bernoulli hypothesis, it is possible to evaluate the first crack load considering a flexural tensile strength, f_{ctm} , of 3 MPa which results equal to 47 kN. If the beam behaves according to Bernoulli's hypothesis at that crack load it should be reported a great change of stiffness. This behaviour can be explained considering that the beam has an a/d ratio equal to 3 which is a borderline value between the possibility of developing flexural cracking failure mode or *arch mechanism*. As a consequence, the real behaviour is a mixed one which can explain the experimental results. In particular, if the first mechanism activated is the strut and tie model, the cracking process starts propagation of short microcrack due to the uniaxial tension developed in the tie. Afterwards, due to the flexural mechanism the cracks grow in height in the midspan zone, leading to a great change in the stiffness. Indeed, taking into account the crack pattern reported by the authors [30], the great flexural cracks appear at a load equal to 100 kN.

The numerical model shows the first crack at a tension equal to the uniaxial tensile strength at a load equal to 37 kN which is lower than the value obtained assuming Bernoulli's hypothesis which means that the first crack is caused by an uniaxial force in the tie. Furthermore, the numerical curve does not greatly change its slope until the load of 75 kN, matching perfectly the experimental one. Therefore, the FEM prediction is not able to match perfectly the change of stiffness because, observing the crack propagation process, the midspan cracks do not grow quickly above 75 kN in the beam's height but they continue to spread in horizontal direction, creating a smoother stiffness loss. The latter gives a P_{cr} error of 45%. However, the rapid stiffness changes could be explained also with the possibility of existing internal crack developed during load assessment cycle or beam's transportation.

Moreover, the possible reliability of numerical models is proved by the fact that the numerical and the experimental branch are parallel, which means that the failure stiffness is the same. Indeed, the crack pattern could help to confirm that the variation of stiffness is caused by the differences of the flexural crack propagation which results in cracks less high than the real ones. The latter means a high depth of compressive zone and a low neutral axis position which must be higher at the ultimate state of the beam. An

explanation of this behaviour could be that the damage model is not able to simulate a crack evolution attached to the real one.

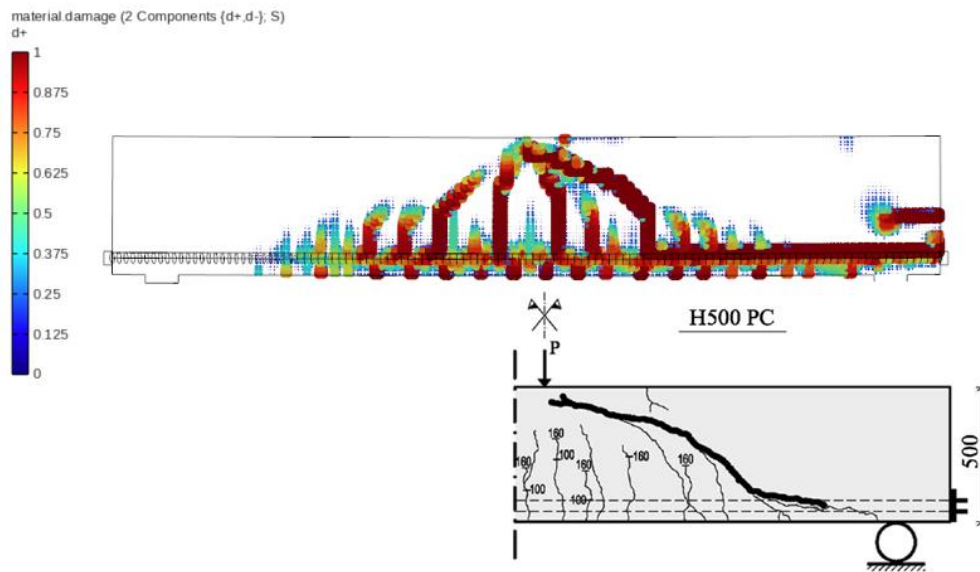


Fig. 26 - Comparison between numerical (upper figure) and experimental (bottom figure) crack pattern for H500PC

2.2.2.2 H1000PC

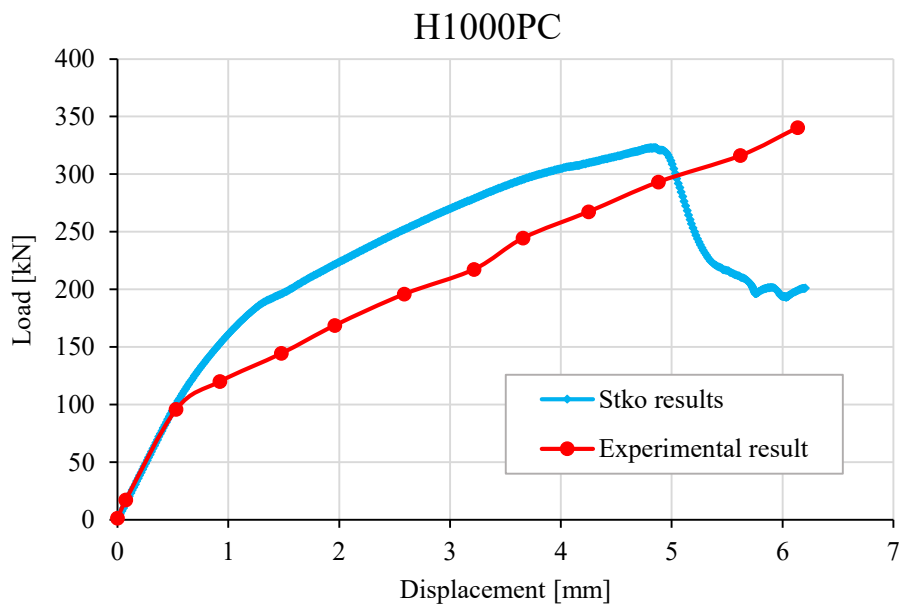


Fig. 27 - Comparison between numerical and experimental load - displacement curve for H1000PC

Considering the beam H1000PC, the experimental curve [Fig. 27] presents a clear change of stiffness at 100 kN. As the H500PC, the first crack load evaluating with Bernoulli's

theory is lower, around 88 kN so the beam behaves as it is explained before. Therefore, the numerical curve presents a first crack load of 77 kN, which corresponds to a principal tensile stress in the bottom part equal to 2 MPa, equal to the uniaxial tensile strength. The evaluation of control parameters is reported in Annex 1 and the final results are presented Table 10.

Table 10 - Control parameters for H1000PC

H1000PC	P_{cr} [kN]	P_u [kN]	δ [mm]	S_1 [-]	S_2 [-]
Experimental results	100	340	6.30	179	42
STKO predictions	77	323	4.86	190	43
Manual evaluations	88	393	-	-	-
STKO predictions/Experimental results	0.77	0.95	0.77	1.06	1.02
Manual evaluation/Experimental results	0.88	1.16	-	-	-

In this case, it is more evident than in the previous beam, the inability of the numerical model in matching the perfect crack propagation. In fact, the simulated curve leads to a P_{cr} error of 23% and a δ difference of 23%. Moreover, the elastic and the nonlinear stiffness are quite in agreement due to the low error percentages (6% and 2%). Finally, also for this beam the ultimate load's reliability is proved by a development of a shear failure, quite similar to the real one. Indeed, more than for H500PC the crack pattern presents a final configuration far from a possible real one, due to the low height of flexural crack.

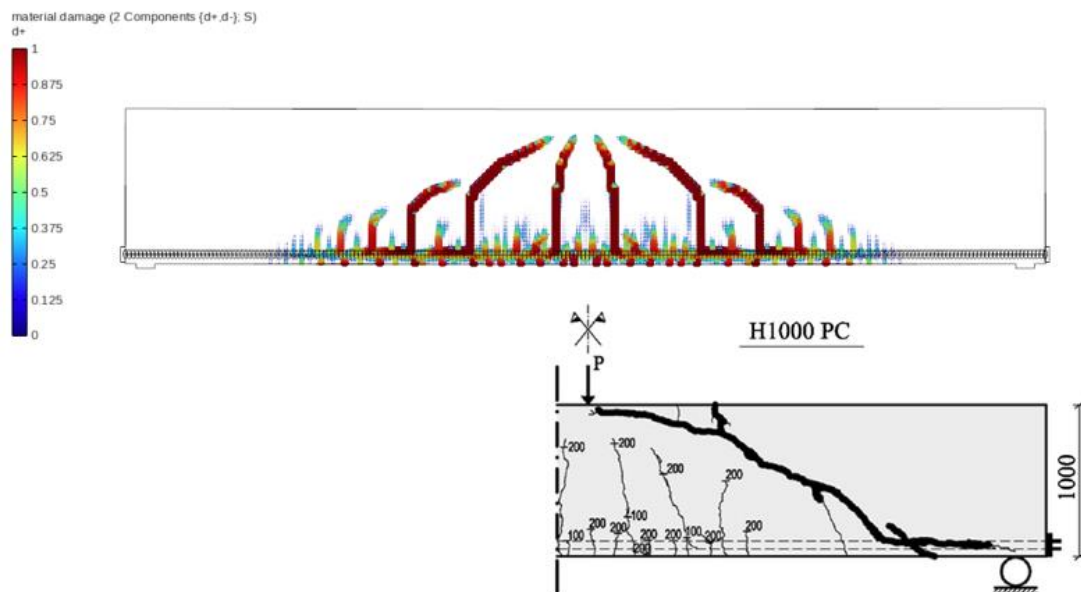


Fig. 28 - Comparison between numerical (upper figure) and experimental (bottom figure) crack pattern for H1000PC

2.2.2.3 H1500PC

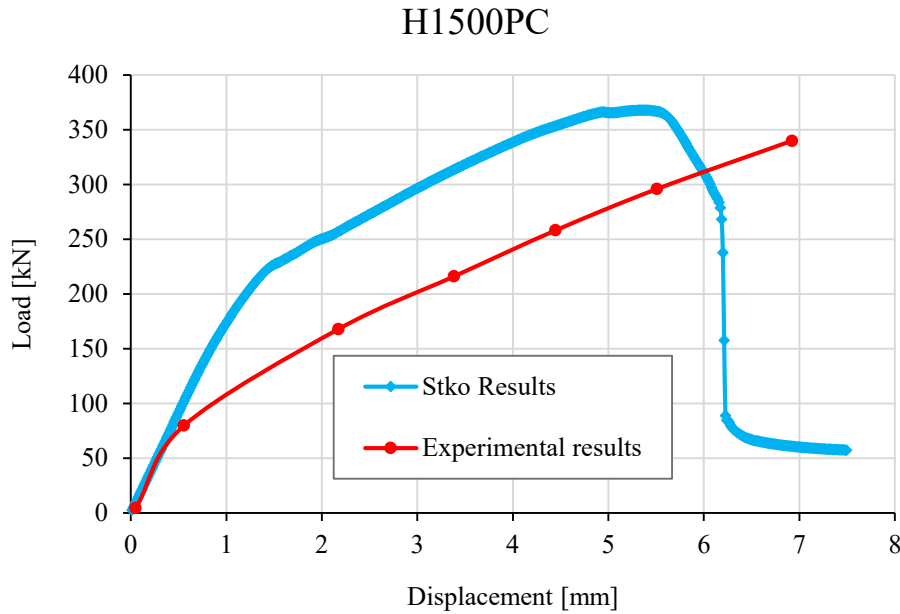


Fig. 29 - Comparison between numerical and experimental load - displacement curve for H1500PC

The H1500PC experimental curve presents a linear branch up to 60 kN, as shown in Fig. 29, which is lower than the first crack load evaluated manually considering the Bernoulli theory, which is around 130 kN. In this case, the experimental curve leads some doubts about its validity due to the very low cracking load, compared to Bernoulli's one. A possible explanation could be that it was pre-cracked internally before the test. The evaluation of control parameters is reported in Annex 1 and the final results are presented in Table 11.

Table 11 - Control parameters for H1500PC

H1500PC	P_{cr} [kN]	P_u [kN]	δ [mm]	S_1 [-]	S_2 [-]
Experimental results	50	341	7.00	209	39
STKO predictions	150	368	5.35	179	43
Manual evaluations	130	523	-	-	-
STKO predictions/Experimental results	3.00	1.08	0.76	0.86	1.10
Manual evaluation/Experimental results	2.60	1.53	-	-	-

Clearly, the numerical curve shows a very far behavior with respect to the experimental one which leads to an P_{cr} error of 300% and a displacement difference of 24%. In fact, it shows the first crack at 150 kN with a tensile stress of 2.2 MPa which is closer to the f_t value: this demonstrates that the beam's behavior is a mixed one and probably the first

activated mechanism is the arch one. As with the previous beams, the crack propagation [Fig. 30] does not follow the real one which has been faster due to the high stiffness loss, observed in the experimental curve. Nonetheless, the stiffness up to the failure seems to be quite similar and the final crack pattern follows the real one, in fact it shows an error of 10%.

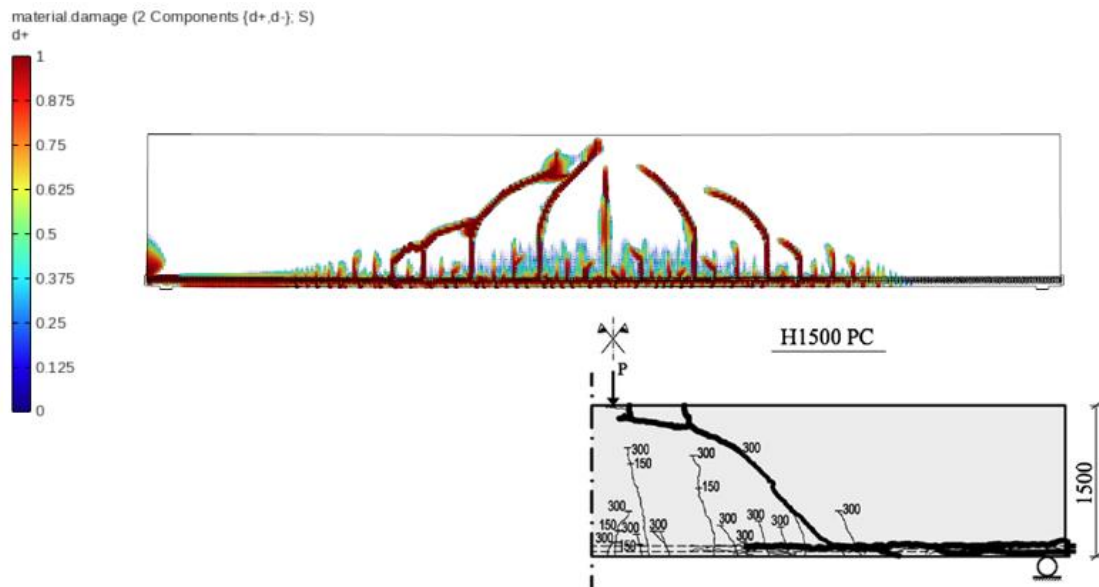


Fig. 30 - Comparison between numerical (upper figure) and experimental (bottom figure) crack pattern for H1500PC

2.2.2.4 Final results and comments for PC beams

In this paragraph it is given a final overview of control parameters measured for the three beams H500, H1000, H1500 with the “PC” concrete.

Table 12 - Control parameters overview for PC

STKO predictions / Experimental results					
ID	P_{cr}	P_u	δ	S_1	S_2
H500PC	0.55	0.97	0.82	1.05	1.09
H1000PC	0.77	0.95	0.77	1.06	1.02
H1500PC	3	1.08	0.76	0.86	1.10
μ	1.44	1.00	0.78	0.99	1.07
SD	368.05%	0.95%	0.18%	2.73%	0.41%

In Table 12, the mean values, μ , and the Standard Deviation, SD, of the ratio between the STKO predictions and the experimental results are reported. Considering the overall view, the models present a very low dispersion around the mean value as far as the P_u , S_1

and S_2 , and it refers that the models are able to predict the capacity of the model and the stiffness during the elastic stage and at the ultimate state. Moreover, it is clearly evident that it is not able to provide a reasonable development of crack pattern which leads to a high SD value for the first cracking load P_{cr} and for the ultimate displacement δ .

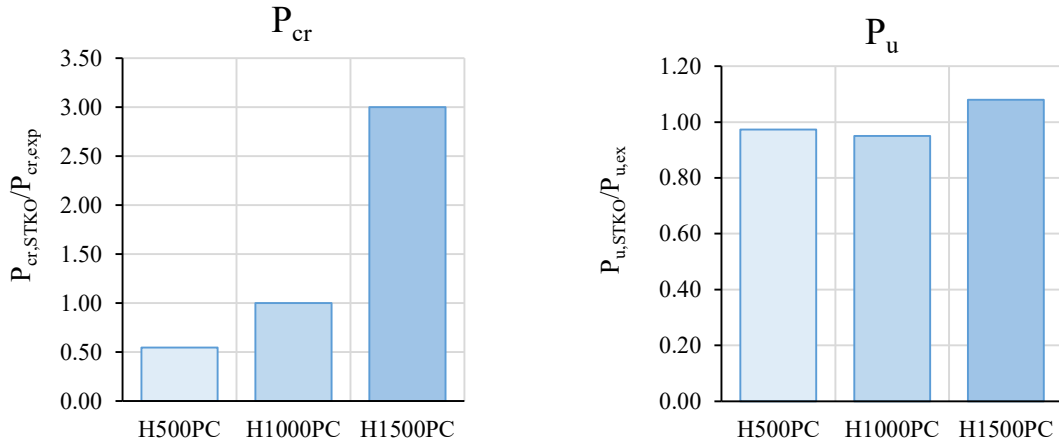


Fig. 31 - P_{cr} (right figure) and P_u trends (left figure) for PC beams

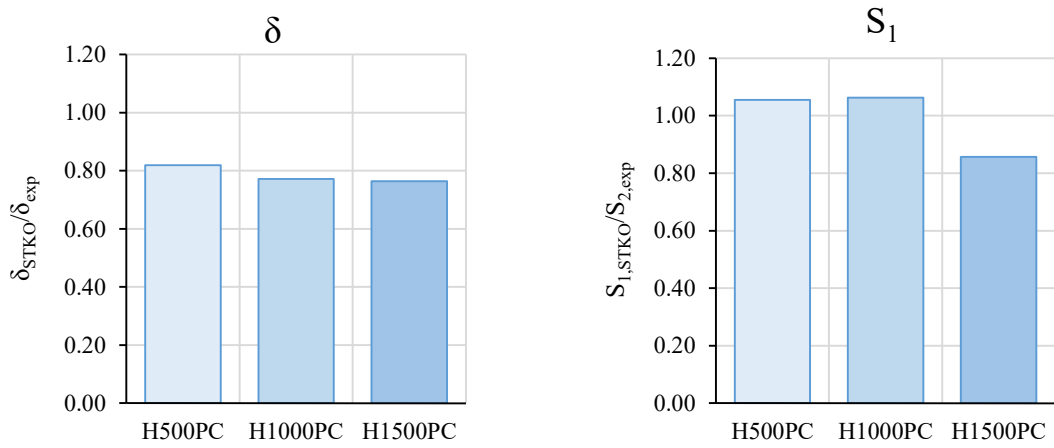


Fig. 32 - δ (right figure) and S_1 (left figure) trends for PC beams

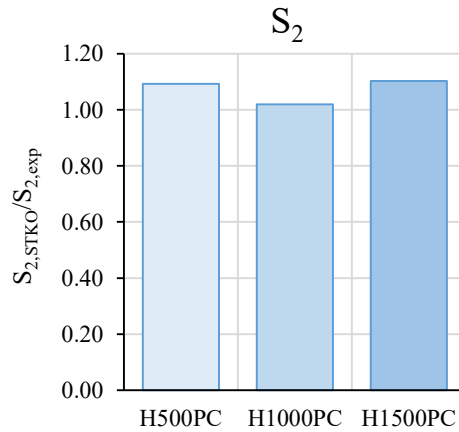


Fig. 33 - S_2 trend for PC beams

Fig. 31, Fig. 32 and Fig. 33 show the general trend of numerical prediction for P_u , δ , S_2 . For all the three beams, the predictions maintain the same errors up to +15%. In particular, P_u is in good agreement with experimental results while for δ the trend is constant while the percentage of error is high due to the wrong stiffness evolution predicted by the model. Indeed, the S_2 maintains an acceptable and constant error which detects that even if the stiffness is higher the final damage evolution reproduces the real one since the nonlinear branch stiffness is the same as the experimental one. The S_1 matches the experimental results for the H500 and H1000, while the H1500 is an outlier, as shown in Fig. 32. Furthermore, as explained before, the H1500 has an experimental first crack load which is very far from the analytical one and as a consequence it is not taken into account. The P_{cr} chart shows a high dispersion of the results and a good prediction only for the H1000. Those results report that the model is not able to predict the crack load which determines the quick change of stiffness. The explanation is in the predicted evolution of the flexural cracks which do not arise deep in the beams' height but remain low and smeared horizontally.

2.2.3 Fiber Reinforced Concrete: result and discussion

The analysis of the previous beam without the fibers has been useful in order to evaluate the reliability of failure proposed by the software for the fiber reinforced concrete which is the research objective.

2.2.3.1 H500FRC50

The experimental curve of H500FRC50 [Fig. 34] shows a linear branch up to 50 kN which continues with a nonlinear long branch up to the bars' yielding, followed by a horizontal plateau until the failure. The authors report that the final failure is caused by a combined action of shear and bending. The long nonlinear branch is representative of the fibers contribution which allows the development of a dense damage, bridged by them, before the flexural failure. The numerical model setting allows to capture perfectly the pre yielding behaviour while is not able to provide good prediction of the post yielding. The post-crack behaviour is governed by the steel capacity which is modelled as a perfect elasto-plastic relationship which can lead to problems in the correct capacity prediction.

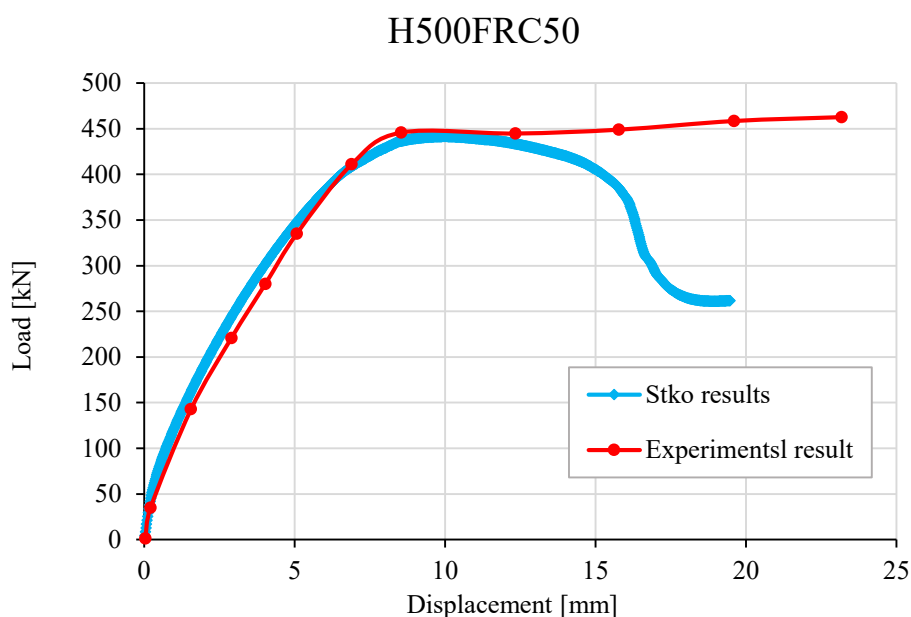


Fig. 34 - Comparison between numerical and experimental load - displacement curve for H500FRC50

Moreover, considering the final deformed shape of the beams, it refers to a mixed failure due to the flexural and the shear cracks as it is reported by the authors. In Table 13, the control parameters for the H500FRC50 are reported: as it is possible to notice there is a good agreement for the P_u , S_1 and S_2 , with a maximum error of 7% while there are differences between the ultimate displacements. As far as P_{cr} is concerned, it must be admitted that in the evaluation of the FRC experimental curve it is quite difficult to detect the change of stiffness graphically. This is due to the fact that the behaviour follows a high non-linearity and the scale plot is not able to clarify the point where the slope changes. Hence, the P_{cr} value comparison is not worthy to consider and comment on as the PC concrete. Nonetheless, in this case we have a good relation between the experimental and numerical P_{cr} .

Table 13 - Control parameters for H500FRC50

H500FRC50	P_{cr} [kN]	P_u [kN]	δ [mm]	S_1 [-]	S_2 [-]
Experimental results	35	472	23.18	197	54
STKO predictions	37	441	10.56	210	54
Manual evaluations	39	394	-	-	-
STKO predictions/Experimental results	1.06	1.07	0.46	1.07	1.00
Manual evaluation/Experimental results	1.11	0.83	-	-	-

The crack pattern shows a clear shear-flexural damage quite similar to the real one with the presence of a diagonal and vertical cracks. The latter determines the final failure of the element.

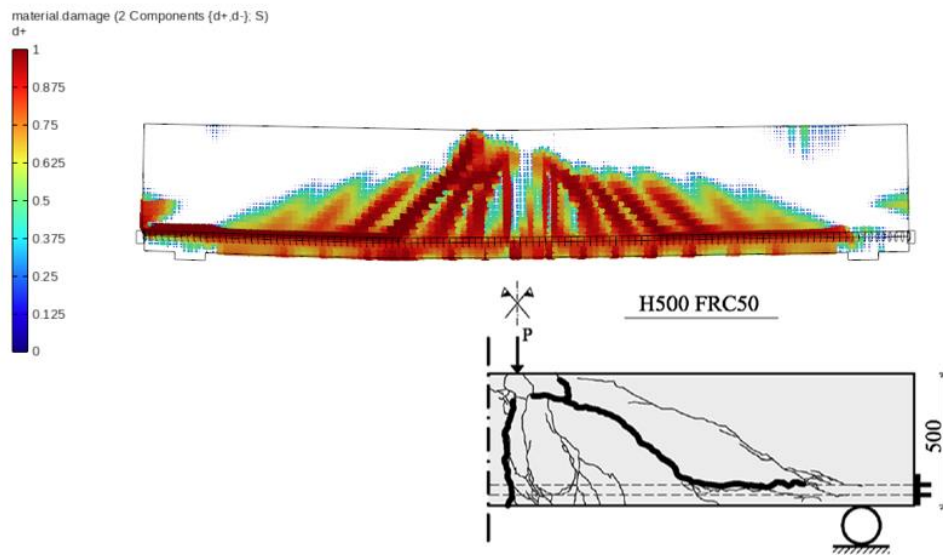


Fig. 35 - Comparison between numerical (upper figure) and experimental (bottom figure) crack pattern for H500FRC50

2.2.3.2 H1000FRC50

The authors report that the beam H1000FRC50 shows a lower shear capacity. In fact, they demonstrate that it is out of the trend which takes in account the ratio between the experimental results and MC2010 previsions. Hence, also the numerical predictions give a load-displacement curve very different from the experimental one.

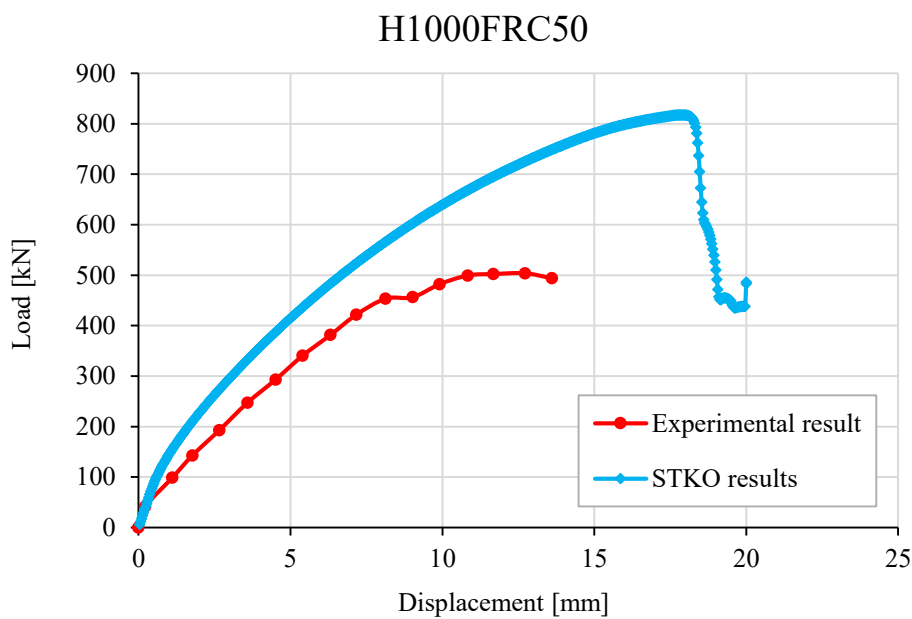


Fig. 36 - Comparison between numerical and experimental load - displacement curve for H1000FRC50

In Table 14, the control parameters show that the numerical analysis gives results which are very far from the real ones, apart from the S_1 .

Table 14 - Control parameters for H1000FRC50

H1000FRC50	P_{cr} [kN]	P_u [kN]	δ [mm]	S_1 [-]	S_2 [-]
Experimental results	41	528	11.68	187	55
STKO predictions	71	818	17.83	179	40
Manual evaluations	70	722	-	-	-
STKO predictions/Experimental results	1.73	0.64	1.53	0.96	0.73
Manual evaluation/Experimental results	1.71	1.37	-	-	-

Indeed, the crack pattern, in Fig. 37, does not show a final failure for shear as the final crack which determines a bending failure is a vertical one. Hence, the numerical prediction provides a behaviour that is totally detached from reality.

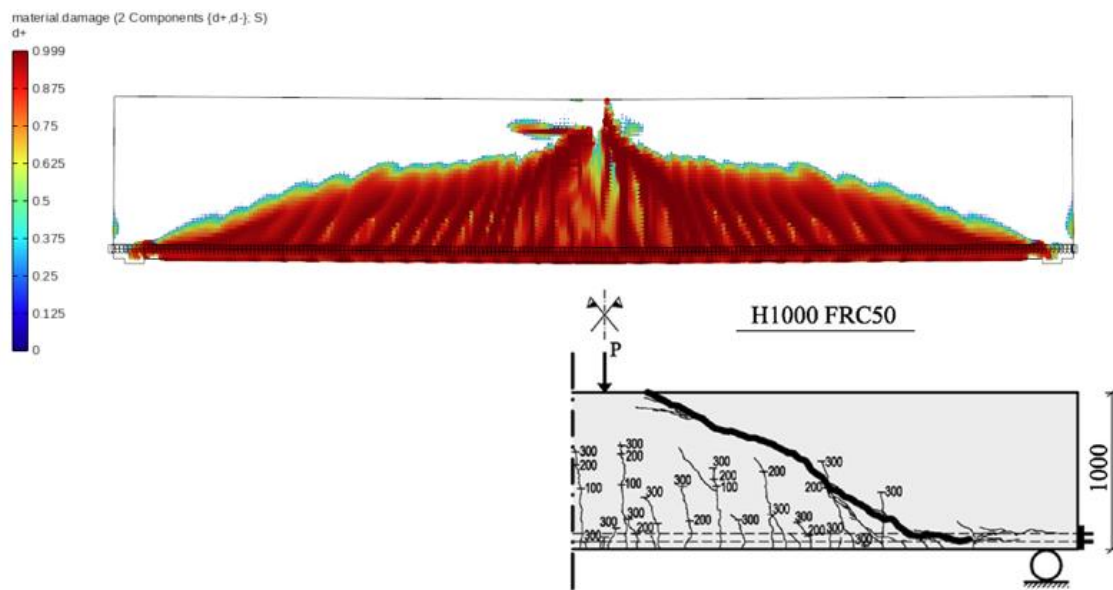


Fig. 37 - Comparison between numerical (upper figure) and experimental (bottom figure) crack pattern for H1000FRC50

Therefore, as reported before, there are several doubts about the reliability of the experimental behaviour which induces the writer not to take this comparison into account.

2.2.3.3 H1500FRC50

The H1500FRC50 experimental curve is dominated by the nonlinear behaviour which is able to reach a high ultimate load and displacement. The numerical prediction completely detects the elastic behaviour but shows a more stiffened branch in the nonlinear stage.

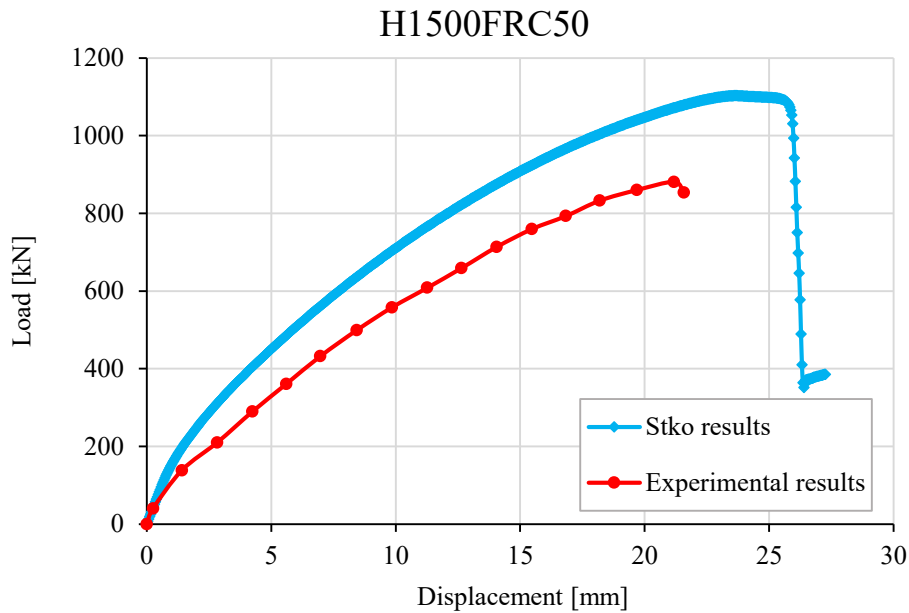


Fig. 38 - Comparison between numerical and experimental load - displacement curve for H1500FRC50

Furthermore, the ultimate load has an error of 12%, higher than the error value obtained for the other previous cases.

Table 15 - Control parameters for H1500FRC50

H1000FRC50	P_{cr} [kN]	P_u [kN]	δ [mm]	S_1 [-]	S_2 [-]
Experimental results	39	943	21.18	158	38
STKO predictions	101	1103	21.18	164	43
Manual evaluations	104	1019	-	-	-
STKO predictions/Experimental results	2.59	0.86	1.00	1.04	1.13
Manual evaluation/Experimental results	2.67	1.08	-	-	-

Nonetheless, the crack pattern shows a shear failure in Fig. 39. The pattern seems not to be very close to the real one, especially for the localization of the final diagonal crack which determines the failure.

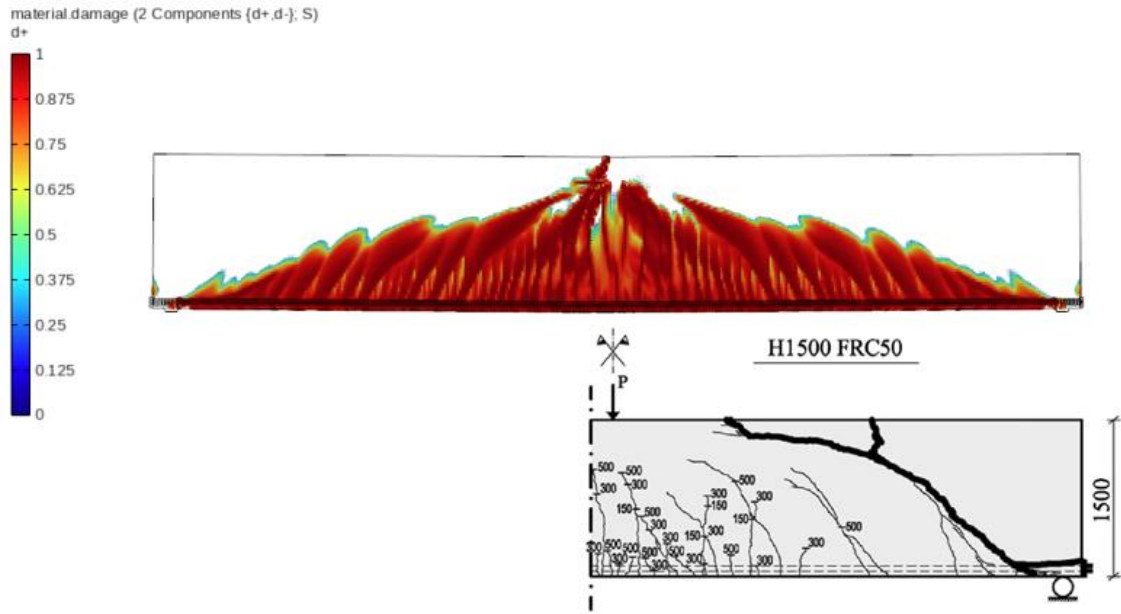


Fig. 39 - Comparison between numerical (upper figure) and experimental (bottom figure) crack pattern for H1500FRC50

2.2.3.4 H500FRC75

The H500FRC75 experimental P- δ curve seems to have a linear behavior up to 53 kN, followed by a nonlinear stage until the failure which happens before the rebars' yielding as shown in Fig. 40. The numerical curve matches the experimental curve. Moreover, it shows a softening behavior which is not reported by the experimental results.

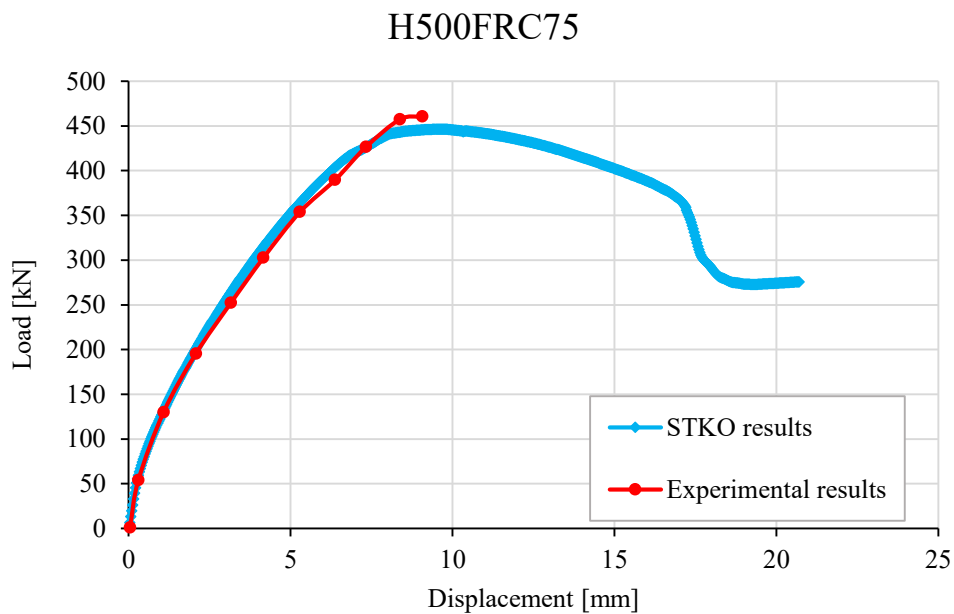


Fig. 40 - Comparison between numerical and experimental load - displacement curve for H500FRC75

Considering the control parameters in Table 16, they show a good agreement for what concerned the P_u , the S_1 and δ with a maximum error of 11%. The slope of the nonlinear branch has a higher error, 19%, with respect to the previous evaluations.

Table 16 - Control parameters for H500FRC75

H500FRC75	P_{cr} [kN]	P_u [kN]	δ [mm]	S_1 [-]	S_2 [-]
Experimental results	35	462	9.07	205	48
STKO predictions	39	441	9.60	182	57
Manual evaluations	39	416	-	-	-
STKO predictions/Experimental results	1.13	1.05	1.06	0.89	1.19
Manual evaluation/Experimental results	1.11	0.90	-	-	-

The crack pattern reports a shear failure but the final diagonal crack results to be less high than the real one, as it is shown in Fig. 41.

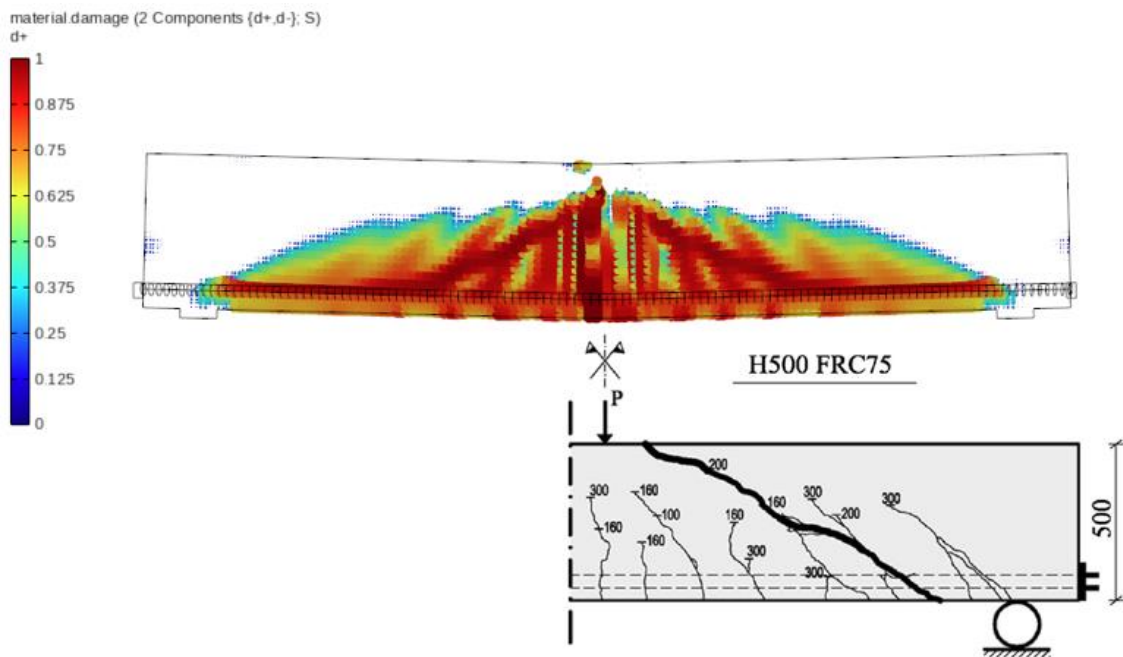


Fig. 41 - Comparison between numerical (upper figure) and experimental (bottom figure) crack pattern for H500FRC75

2.2.3.5 H1000FRC75

The experimental curve describes an elastic behavior up to 104 kN and it continues with the nonlinear stage. The numerical curve is close to the experimental one but, as the previous case, it has a higher stiffness.

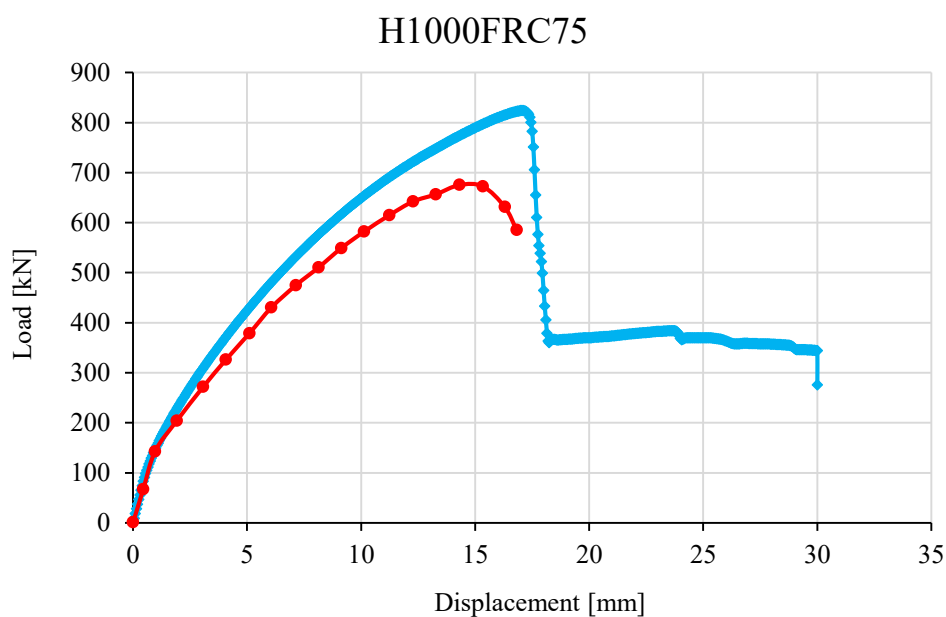


Fig. 42 - Comparison between numerical and experimental load - displacement curve for H1000FRC75

Furthermore, as the H1000FRC50, the ultimate load presents an elevated error of 12%. Indeed, due to the different stiffness, there is an important error also in S_1 and S_2 ratio (26% and 15%).

Table 17 - Control parameters for H1000FRC75

H1000FRC75	P_{cr} [kN]	P_u [kN]	δ [mm]	S_1 [-]	S_2 [-]
Experimental results	67	686	14.31	147	40
STKO predictions	71	824	17.10	186	46
Manual evaluations	70	762	-	-	-
STKO predictions/Experimental results	1.06	0.83	1.20	1.26	1.15
Manual evaluation/Experimental results	1.04	1.11	-	-	-

Finally, the damage pattern shows a shear failure, with a final crack localized very close to the real one, as it is shown in Fig. 43.

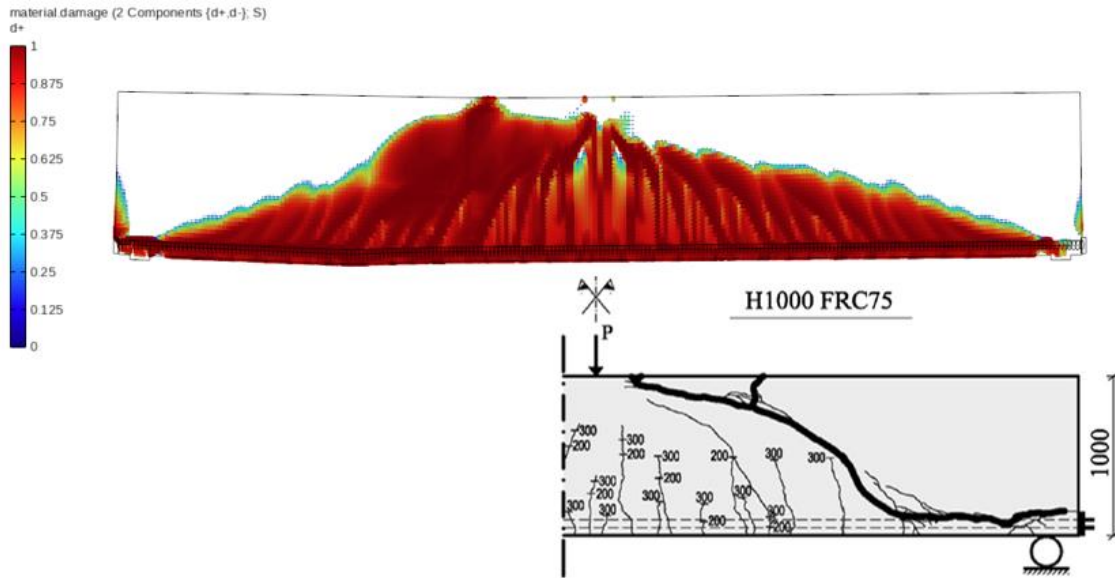


Fig. 43 - Comparison between numerical (upper figure) and experimental (bottom figure) crack pattern for H1000FRC75

2.2.3.6 H1500FRC75

The experimental curve is linear up to 111 kN and it reaches with a nonlinear branch the ultimate load of 1161 kN. The numerical curve is able to predict a similar P- δ relationship but, as H1000FRC75, it is more stiffened than the experimental one [Fig. 44].

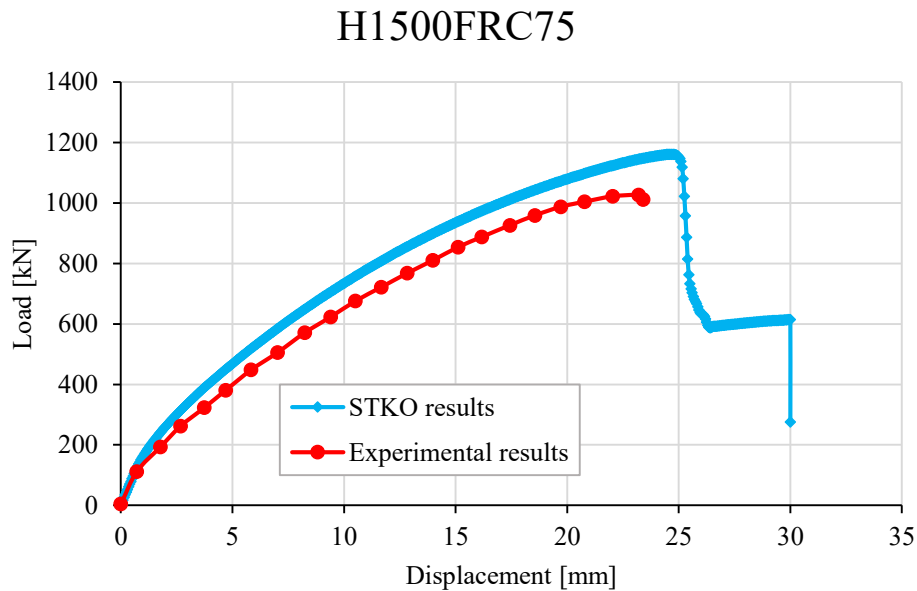


Fig. 44 - Comparison between numerical and experimental load - displacement curve for H1500FRC75

Moreover, in Table 18 the control parameters show a great agreement both for the S_1 and S_2 as also for the displacement.

Table 18 - Control parameters for H1500FRC75

H1500FRC75	P_{cr} [kN]	P_u [kN]	δ [mm]	S_1 [-]	S_2 [-]
Experimental results	111	1083	23.20	151	45
STKO predictions	101	1103	24.65	176	42
Manual evaluations	104	1073	-	-	-
STKO predictions/Experimental results	0.91	0.98	1.06	1.16	0.93
Manual evaluation/Experimental results	0.94	0.99	-	-	-

The crack damage pattern shows a bending failure due to the vertical cracks which is totally different from what was expected as shown in Fig. 45.

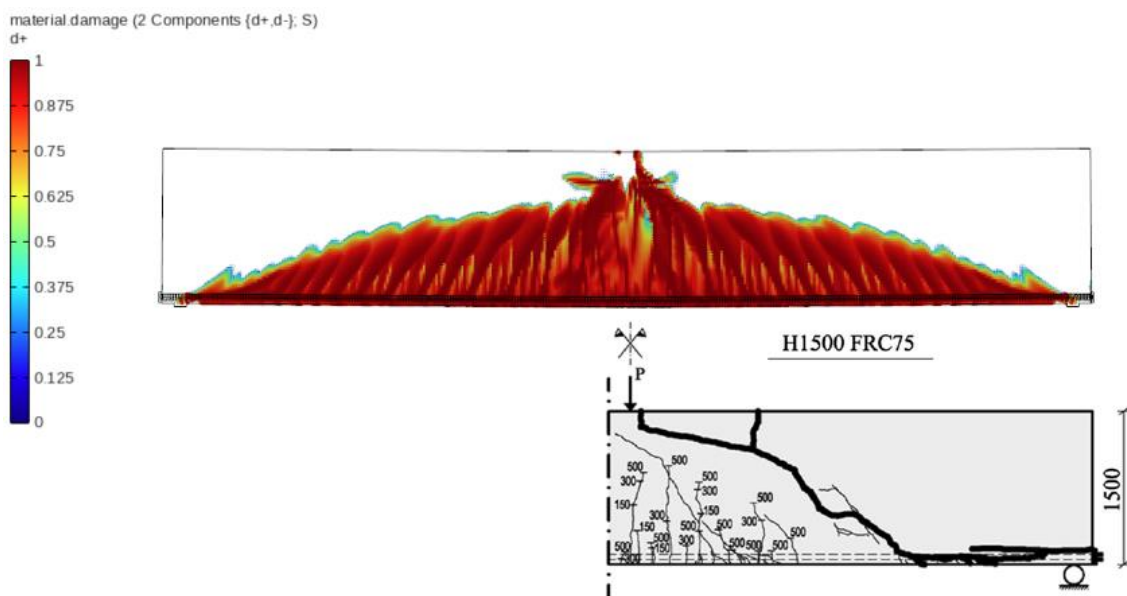


Fig. 45 - Comparison between numerical (upper figure) and experimental (bottom figure) crack pattern for H1500FRC75

2.2.3.7 Final results and comments for FRC beams

In this section, the final overview of the comparisons between the numerical predictions and the experimental results for the FRC beams is reported.

- FRC50

In Table 19, the mean value error for the ultimate P_u is equal to 12%, with a high dispersion (8.98%). Furthermore, there is also a high dispersion around the mean value error for the δ as S_2 . Therefore, there are some doubts about the reliability of experimental tests considering H1000FRC50 specimen taken into account.

Table 19 - Control parameters overview for FRC50

STKO predictions / Experimental results					
ID	P_{cr}	P_u	δ	S_1	S_2
H500FRC50	1.06	1.07	0.46	1.07	1.00
H1000FRC50	1.73	0.64	1.53	0.96	0.73
H1500FRC50	2.59	0.86	1.00	1.04	1.13
μ	1.79	0.86	0.99	1.02	0.95
SD	118.00%	8.98%	57.36%	0.65%	8.51%

The differences on the predicted P_u and the real one have suggested investigating the G_t influences, which leads to some uncertainties about the determination of its values. Indeed, after different trials, the most promised predictions are given by a G_t value equal to the half of the one recommended by MC2010. In the following part, there are reported the final control parameters evaluations for the H500FRC50, H1000FRC50 and H1500FRC50 with the adjusted G_t , while all the curves and the new crack patterns are reported in the Annex 1.

Table 20 – Control parameters for the FRC50 with the G_t adjusted

STKO predictions / Experimental results					
ID	P_{cr}	P_u	δ	S_1	S_2
H500FRC50	1.06	1.10	0.46	1.07	1.00
H1000FRC50	1.73	0.72	1.27	0.96	0.82
H1500FRC50	2.59	0.99	0.89	1.08	1.18
μ	1.79	0.93	0.87	1.03	1.00
SD	118.00%	7.72%	32.96%	0.87%	6.70%

In Table 20, it should be noticed that for the beam H500FRC50, there were already promising results with the first assumption of G_t . Moreover, considering the adjusted value the numerical behavior is not greatly affected by the changes and it still produces reliable predictions. Furthermore, as far as the H1000FRC50 and H1500FRC50 is concerned, considering the adjusted G_t value, the analyses give results which are in better agreement with the experimental ones. This evidence could be explained assuming a size effect for the highest beams. According to Carpinteri [40], the increasing of beam's height can lead to a decreasing of tensile strength as well as consequently the G_t . Hence, the dimension leads to a brittleness in the element that could be represented lowering the G_t .

Therefore, considering the crack pattern, the final deformed shape and crack failure is more attached to the experimental one for the H1000FRC50 and H1500FRC50, as shown in the following Fig. 46 and Fig. 47, while for H500FRC50 is quite the same.

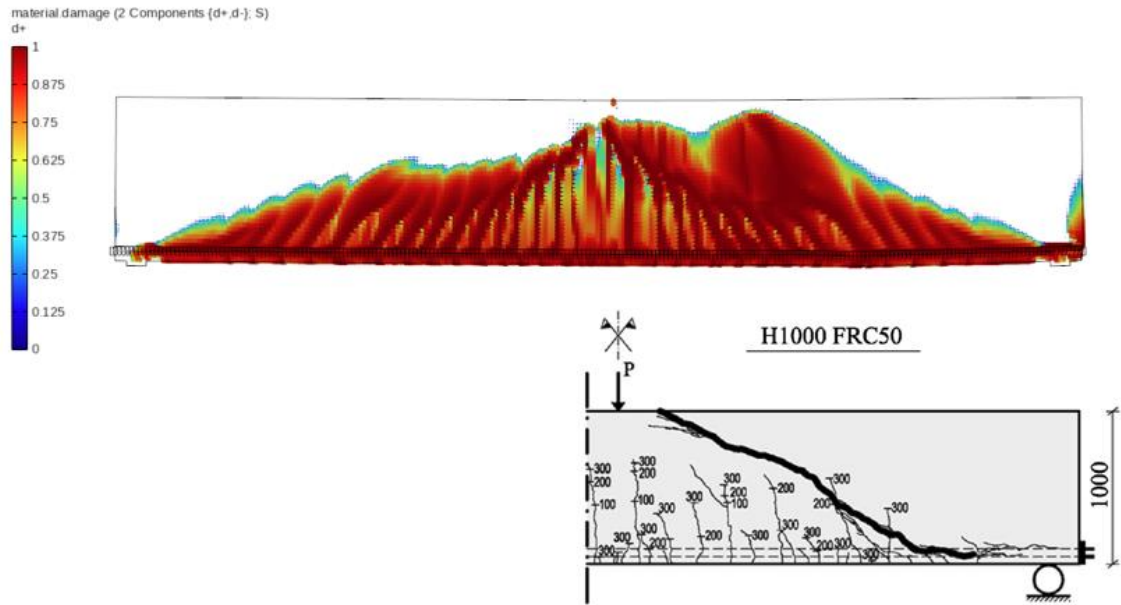


Fig. 46 - Comparison between numerical (upper figure) and experimental (bottom figure) crack pattern for H1000FRC50 with adjusted G_t

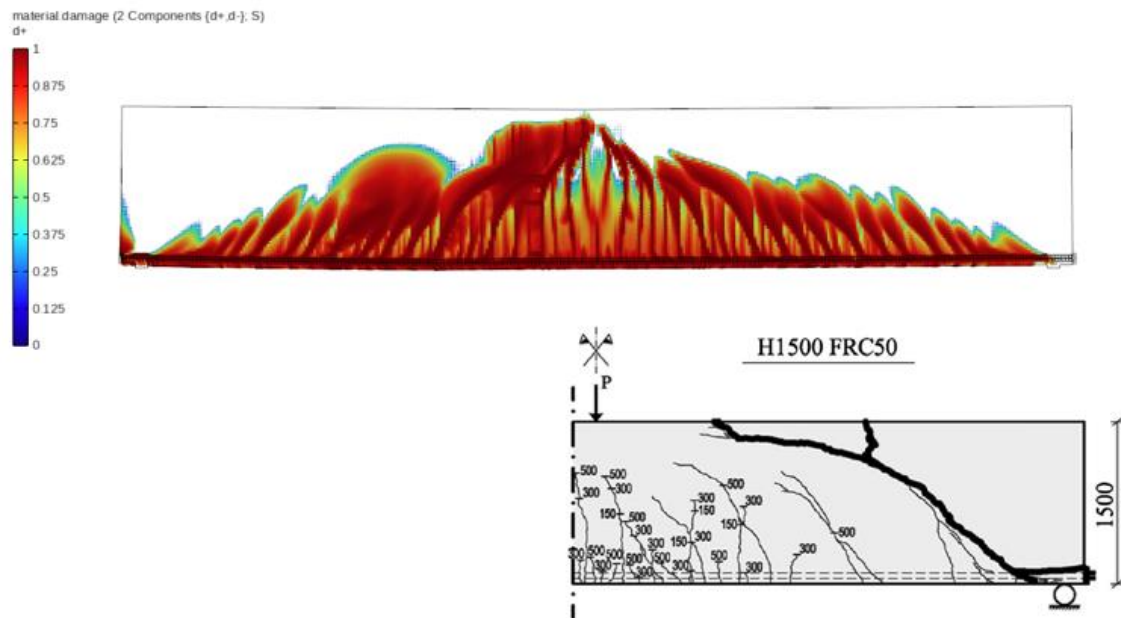


Fig. 47 - Comparison between numerical (upper figure) and experimental (bottom figure) crack pattern for H1500FRC50 with adjusted G_t

- FRC75

Table 21 reports all the control parameters for the FRC75.

Table 21 - Control parameters for FRC75

STKO predictions / Experimental results					
ID	P_{cr}	P_u	δ	S_1	S_2
H500FRC75	0.98	1.03	1.06	0.87	1.19
H1000FRC75	1.06	0.83	1.19	1.25	1.15
H1500FRC75	0.91	0.93	1.06	1.16	0.93
μ	0.98	0.93	1.10	1.09	1.09
SD	1.10%	2.05%	1.15%	7.74%	3.77%

As for the FRC50, there is a high dispersion for the S_1 and for S_2 . Hence, the numerical analysis was performed again considering a G_t equal to the half of the one reported in Table 1.

Table 22 - Control parameters for the FRC75 with the G_t adjusted

STKO predictions / Experimental results					
ID	P_{cr}	P_u	δ	S_1	S_2
H500FRC75	0.98	1.05	1.06	0.70	1.19
H1000FRC75	1.06	0.91	1.20	1.24	1.15
H1500FRC75	2.59	0.92	1.06	1.16	0.91
μ	1.54	0.96	1.11	1.03	1.08
SD	164.34%	1.23%	1.18%	17.08%	4.50%

Table 22 shows a worsening in the accuracy of the numerical predictions with respect to the previous analysis for what concerns the S_1 but a better prediction for the ultimate load. Moreover, as for FRC50, the H500FRC75 does not show changes in the final ultimate load. Furthermore, there are improvements in the prediction for the beam H1000FRC75 and H1500FRC75 as far as their crack patterns are more attached to reality [Fig. 47 and Fig. 48]

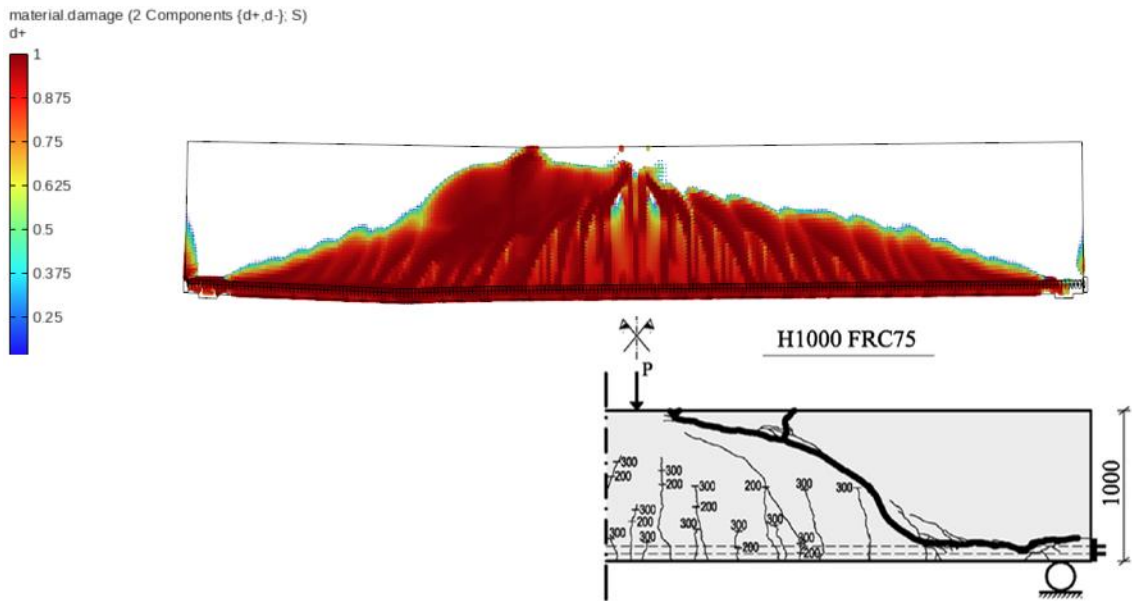


Fig. 48 - Comparison between numerical (upper figure) and experimental (bottom figure) crack pattern for H1000FRC75 with adjusted G_t

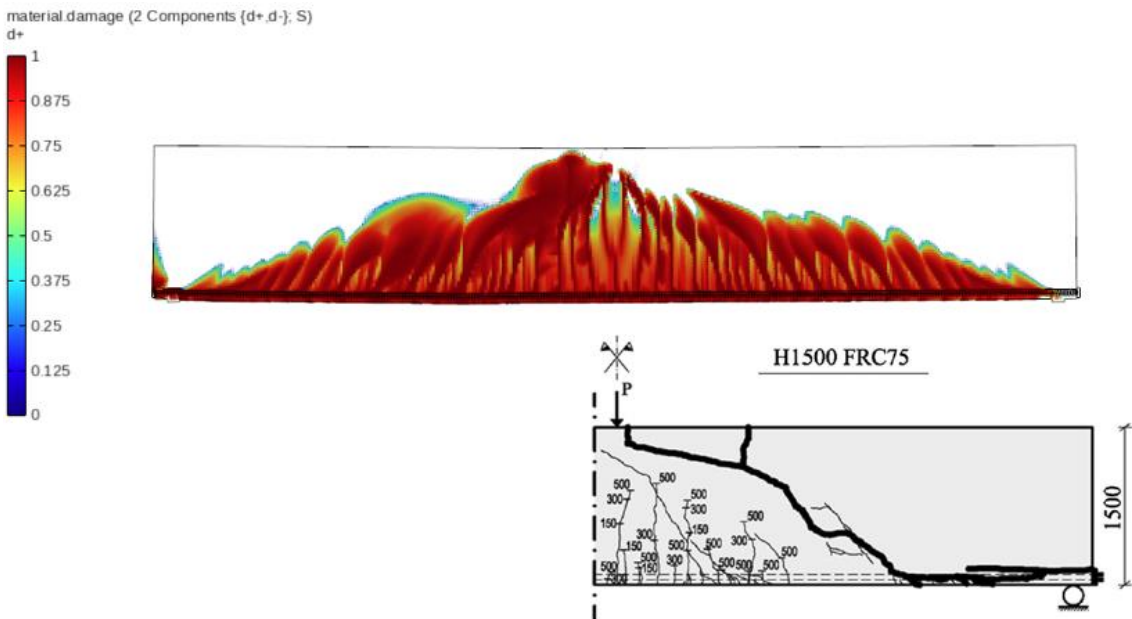


Fig. 49 - Comparison between numerical (upper figure) and experimental (bottom figure) crack pattern for H1500FRC75 with adjusted G_t

The following charts report the general overview of the ratio between FRC beams STKO predictions and experimental results for the control parameters.

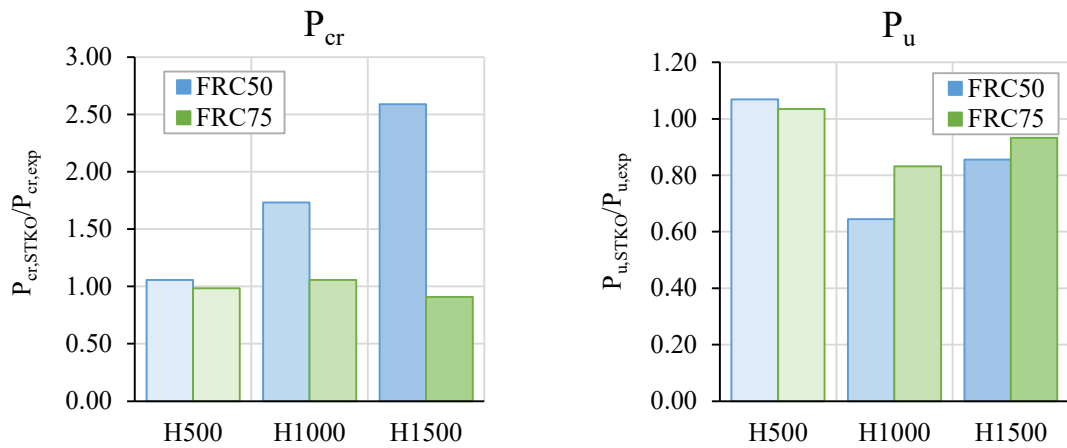


Fig. 50 - P_{cr} (right figure) and P_u (left figure) trends for FRC beams

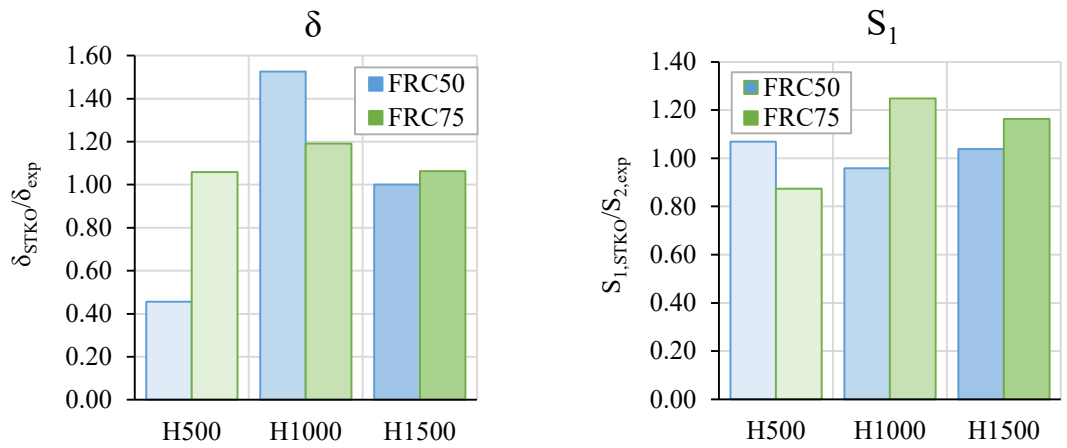


Fig. 51 - δ (right figure) and S_1 (left figure) trends for FRC beams

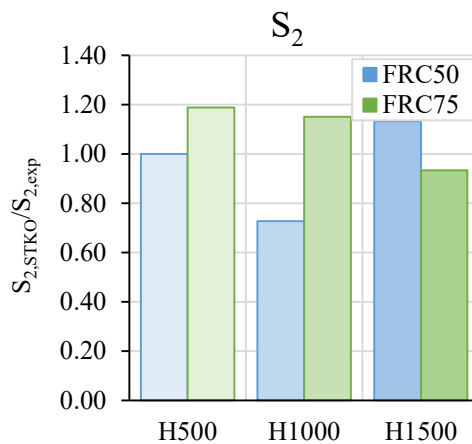


Fig. 52 - S_2 trend for FRC beams

In Fig. 50, the P_{cr} shows a very high dispersion, especially for the H1000FRC50 and H1500FRC50 while it is observed a stability of the results for FRC75. As the behaviour of FRC beams is dominated by nonlinearity, the graphically localization of the P_{cr} is

difficult to clearly detect. As a consequence, the P_{cr} and S_1 are less significant in the discussion. In Fig. 50, the P_u values are in good agreement for all beams with both FRC50 and FRC75 except for the H1000FRC50. Furthermore, the authors report that H1000FRC50 is out of the trend which considers the ratio between analytical evaluation (according to MC2010) and experimental results. Hence, this comparison is not reliable and it is not taken into account in the document final evaluation § 5.1.2.

The prediction of δ is valuable for all the beams with FRC75 while they are not accurate for H500FRC50 and H1000FRC50, as reported in Fig. 51. For the H500FRC50, the model is not able to predict the nonlinear plateau due to the constitutive law adopted.

Finally, the S_1 and S_2 present a higher dispersion of the results, especially for the S_1 . Furthermore, the most important aspect to take into account is the nonlinear slope S_2 which presents a general error of $\pm 20\%$. The results are considerably good as the nonlinear branch of FRC beams is determined by the fiber orientations and dispositions which are quite random variables. Furthermore, the only value with an error over the 20% is of H1000FRC50 in accordance with the previous control parameters analysed.

2.3 Case study 2: Cuenca's Experimentation

The second beams' set is represented by the experimental tests realized by Estefania Cuenca at University of Brescia [41]. In particular, it is composed of nine pre-stressed I-beams with asymmetric flange dimensions. The aim of Cuenca's work was the analysis of the fiber contribution to the shear capacity. The nine beams are all six meter long with an a/d ratio equal to 3, except for beam H400h/6, and a distance of 5 m between the supports. The concrete properties could be assimilated to a high strength concrete with a characteristic compressive strength value, f_{ck} , of 60 MPa. The pre-stressed beams are over reinforced longitudinally to force a shear failure. The amount of reinforcement is composed of 11 bonded tendons (nominal cross section equal to 140 mm^2) of 7 wires (Y 1860 S7). The initial tension was 1354 MPa and the pre-stressed losses are set at 26.2%. In particular, into the experimental campaign some variables such as the top flange, the type of concrete, the beams' depth and the presence of stirrups or the additional reinforcement are taken into account in order to control the second failure. Moreover,

with the aim to fulfil the research purpose of this work, the FRC beams without any other shear additional reinforcement have been modelled. The latter's ID specimens are HF600/5, HF400h/6, HF400/7 and HF260/9 where the first number refers to the flange width in millimeters. In Fig. 53, the typical cross section is reported and the black boxes indicate the geometrical data for the beams considered.

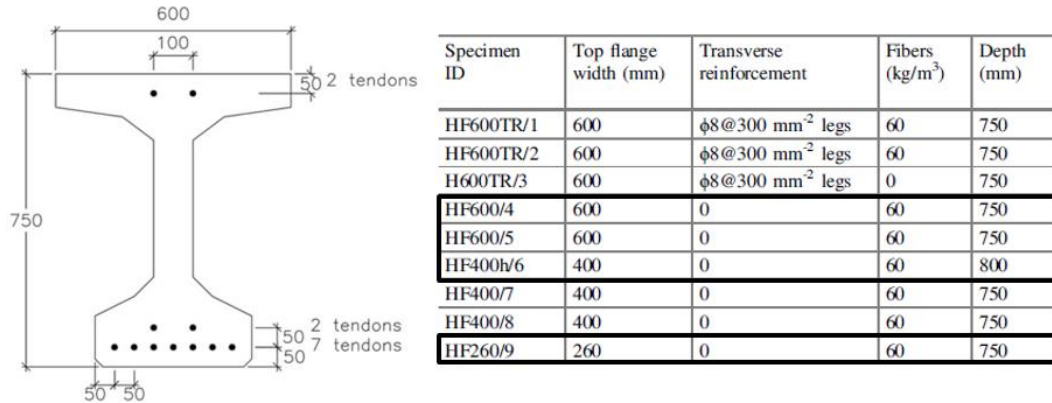


Fig. 53 - Geometric characteristics of Cuenca's specimens

As far as the concrete properties are concerned, the author carried a cylindrical compressive strength test (EN 12390-3) and three points bending test on notched specimens (EN 14651). In Fig. 54, the concrete properties are reported. The flexural test gave the tensile properties as the flexural tensile strength, f_{ctf} , and the residual flexural tensile strength, $f_{R,j}$, of the CDOM at 0.5, 1.5, 2.5 and 3.5 mm. It must be noticed that the author does not report the value of the elastic modulus E .

Specimen ID	f_c (MPa)	f_{ctf} (MPa)	f_{R1} (MPa)	f_{R2} (MPa)	f_{R3} (MPa)	f_{R4} (MPa)
HF600TR/1	61.1	3.36	5.26	5.13	–	–
HF600TR/2	65.7	4.39	9.36	9.56	6.89	4.96
H600TR/3	52.4	3.64	–	–	–	–
HF600/4	65.4	4.70	10.46	7.99	6.24	5.12
HF600/5	65.9	4.20	8.55	8.43	5.55	3.92
HF400h/6 ^a	59.5	4.45	8.96	7.49	5.96	4.57
HF400/7	63.5	4.08	6.64	6.70	4.77	3.41
HF400/8	70.0	4.33	8.10	7.02	4.68	3.13
HF260/9	65.0	3.11	6.45	4.38	–	–
Average	63.17	4.03	7.97	7.09	5.68	4.18
SD	4.75	0.51	1.61	1.59	0.79	0.75
CoV (%)	8	13	20	22	14	18

Fig. 54 - Concrete properties of Cuenca's beams

The beams' supports configuration reproduced a simply supported condition and the test set resulted in four points bending tests. The two loads were applied by one 2500 kN hydraulic jack.

2.3.1 FEM modelling strategies

The FEM modelling strategies are the same used for the Minelli's beams and extensively explained in § 2.2.1. Moreover, the following part reports the differences from the previous models in terms of geometry definitions, material properties and analysis setting.

2.3.1.1 Geometry

The IPE section is characterized by the different thickness of its part. The Cuenca's beam cross section is composed of two rectangular flanges which are linked to the web by trapezoidal elements. In the FEM model, the trapezoidal elements are represented by a rectangular box with an area equal to the original one. In the Annex 2 the Finite Element equivalent sections are reported. The tendons layout is simplified by assigning a unique equivalent cable with a concrete cover of 50 mm for both upper and bottom flange. The support plate dimensions are supposed equal to 150x30x1000 mm. In Fig. 55 the different colors detect the change of thickness.

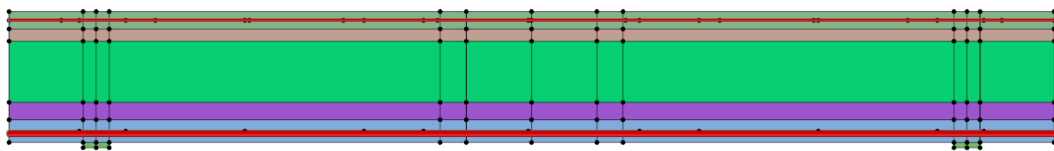


Fig. 55 - Element properties plot for Minelli's beams in STKO Opensees

2.3.1.2 Physical properties

- Material properties for concrete

In Table 23 and Table 24, the concrete compressive parameters inputs are reported - the E modulus is assumed equal to the one proposed by the MC2010 for the C60.

Table 23 - Concrete compressive parameters inputs of Cuenca 's beams

Concrete type	E [MPa]	f_{c0} [MPa]	f_{cp} [MPa]	f_{cr} [MPa]	G_c [N/mm]
H600/5	40700	26.36	65.9	8.57	38.7
H400/7	40700	25.40	63.9	8.26	39.8
H400h/6	40700	23.80	59.5	7.73	38.0
H260/9	40700	26.00	65.0	8.45	38.7

Table 24 - Concrete tensile parameters inputs of Cuenca's beams

Concrete type	f_t [MPa]	f_{Ftu} [MPa]	G_t [N/mm]
H600/5	2.80	1.85	4.63
H400/7	2.72	1.59	3.98
H400h/6	2.97	1.99	4.97
H260/9	2.07	1.89	4.73

- Material properties for pre-stressed steel

In Table 25, the input for the tendons' steel are indicated.

Table 25 - Steel tendons parameters input of Cuenca's beams

E [MPa]	f_y [MPa]
210000	1860

The pre-stressed condition is given by assigning a new material property, *InitStressMaterial*, in which is defined the material that will be pre-stressed and the initial stress equal to 999 MPa.

2.3.1.3 Analysis steps

The pre-stressing action is given by adding a new analysis step before the loading of structures. The analysis steps are:

- Recorder
- First pattern: applying of boundary conditions
- Analysis Step 1

The analysis features are set in the *AnalysesCommand* which allows the user to define the different linear and nonlinear available analysis tools. For the analysis step 1, it has been defined the followed option:

- *Analysis type command*: static analysis;
- *Constrain command*: *PenaltyMethod* with default penalty values has been set;
- *Numberer Command*: *Parallel Reverse Cuthill-McKee Numberer* because the analysis is split in more than one processor;
- *System Command*: *Mumps*;
- *Algorithm Command*: *Newton Algorithm*;
- *Test Command*: *Norm Displacement Increment*;
- *Integrator Command*: *Load control* with duration equal to 1;
- *Analyze*: *Fixed Time Step* with a number of step equal to 1;
- Second pattern: applying of load as distributed *edgeload* on a length equal to 150 mm;
- Analysis Step 2: setting as explained in § 2.2.1.6.

2.3.2 Pre-stressed fiber reinforced concrete: result and discussion

The author does not report a detailed description of the experimental results. In particular, the ultimate shear resistances V_u are indicated while the P- δ curves are plotted only for two of the models realized (H600/5 and H400/7). For this reason, the reliability of the model prediction has been tested considering manual checking on:

- δ_i uplift displacement at t_0 (t_0 is the time at the application of pre-stressing action);
- σ_b at t_0 which is the stress induced by the pre-stressing action at the bottom fiber;
- σ_t at t_0 which is the stress induced by pre-stressing action at the top fiber;
- P_{de} which is the load able to decompress the bottom fiber of concrete.

Furthermore, a further description of final crack damage is reported instead of the images. The author writes that the final crack configuration presents diagonal cracks, induced by shear actions, and low and small flexural cracks in the bottom parts.

The evaluation of uplift displacement is possible considering that at t_0 the beam carries a uniform moment. The well-known formula (19) for the evaluation of the displacement in

the middle point is of a simply supported beam subjected to a constant bending moment is:

$$y_{max} = -\frac{M_a x}{6 EI} (L - x) \left[1 + \frac{L - x}{L} + \frac{M_a}{M_b} \left(1 + \frac{x}{L} \right) \right] \quad (19)$$

- x is the beam point at which the displacement is evaluated;
- L is the beam length;
- M_a is the moment at the first extreme point while M_b is at the second extreme point. In this case $M_a = M_b$.

The simplified formulation is (20):

$$y_{max} = -\frac{M_a L}{8 EI} \quad (20)$$

As far as the σ_b and σ_t is concerned, it has been applied the *Saint Venant - Navier* formulation (21) for the axial-flexural stresses considering as action the pre-stressing one and the moment induced due to the eccentricity. The stresses due to the self-weight have been neglected.

$$\sigma = \frac{P}{A} + \frac{M_p}{I} y \quad (21)$$

- P is the total pre-stressed force, considering the prestressing losses;
- A is the cross section area;
- M_p is the moment induced by the P eccentricity;
- I is the second moment of inertia;
- y is the depth at which it is evaluated σ .

Finally, assuming a stress equal to zero, the external moment which decompresses the section has been evaluated. Consequently, known M_{ext} as (22), the P_{de} has been estimated as (23):

$$M_{ext} = \left(-\frac{P}{A} \right) \cdot \frac{I}{y_G} \quad (22)$$

$$P_{de} = \frac{M_{ext}}{a} \quad (23)$$

In the following part, the results are reported while the calculations are in Annex 2.

2.3.2.1 HF600/5

In Table 26, the δ_i , σ_b , σ_t , P_{de} and V_u are reported and the ratio between the *STKO Opensees*© prediction, manual evaluation and experimental results.

Table 26 - Control parameters for HF600/5

HF600/5	δ_i	σ_b	σ_t	P_{de}	V_u
Manual evaluations	1.81	-17.22	0.50	308.00	-
Experimental results	-	-	-	-	347.50
STKO predictions	1.77	-16.68	0.30	296.50	352.53
Ratio STKO predictions/Manual evaluations	0.97	0.97	0.60	0.96	-
Ratio STKO predictions/Experimental results	-	-	-	-	1.01

The comparison between the numerical and manual parameters is useful to assess the theoretical reliability of the models. As it is shown, the STKO predictions are in good agreement with the manual evaluations except for the σ_t . Furthermore, the ratio between numerical and experimental σ_t is high due to the small values of the stresses. Therefore, the V_u predicted and tested are in quite perfect agreement.

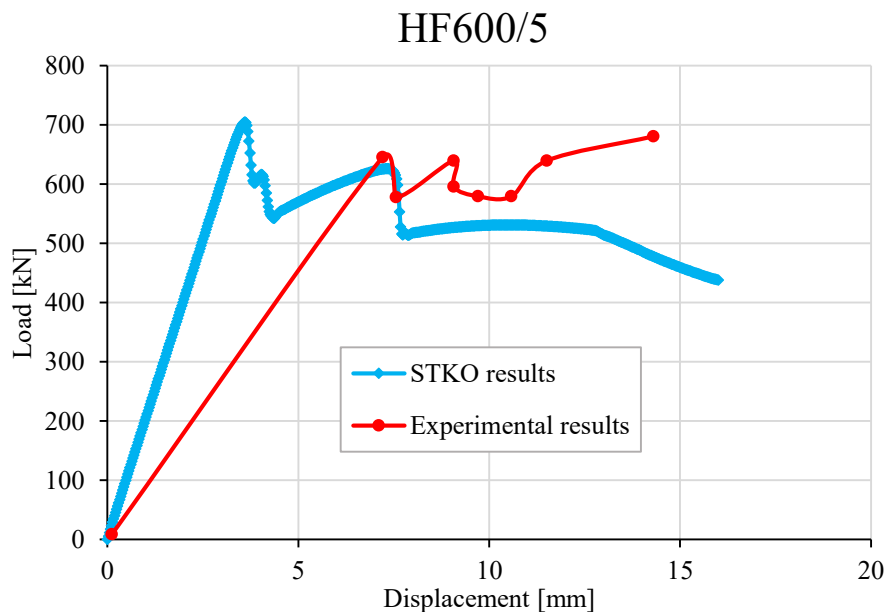


Fig. 56 - Comparison of experimental and numerical curve Load - displacement curve for HF600/5

For the HF600/5 the author reports the $P-\delta$ experimental curve. Furthermore, E. Cuenca did not specify how this curve was measured and it starts from 0, not reporting the initial uplift induced by the pre-stressing action. Hence, the numerical curve has been shifted by δ_i to make the comparison as shown in Fig. 56. The numerical prediction shows a more stiffened behaviour with respect to the experimental one. This could happen due to the assumption of Elastic modulus reported in § 2.3.1.2. Nonetheless, the curve shape after the crack is similar to the experimental one. Considering the crack pattern, in the web, a perfect shear failure is shown at the peak point and it is in perfect accordance with the Cuenca crack damage description [Fig. 56].

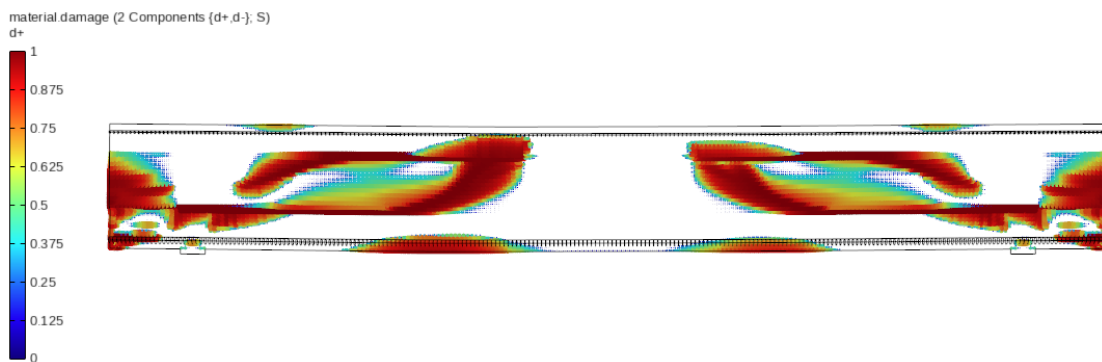


Fig. 57 - Final crack damage of HF600/5

2.3.2.2 HF400/7

Table 27 - Control parameters for HF400/7

HF400/7	δ_i	σ_b	σ_t	P_{de}	V_u
Manual evaluations	1.79	-17.22	0.33	286.03	-
Experimental results	-	-	-	-	389.50
STKO predictions	1.73	-16.63	0.06	274.50	352.53
Ratio STKO predictions/manual evaluations	0.97	0.97	0.18	0.96	-
Ratio STKO predictions/Experimental results	-	-	-	-	0.86

The HF400/7 differs from the HF600/5 for the flange width and its concrete presents small differences as reported in Fig. 53. As the previous case, the manual evaluations are in agreement with the numerical ones. Furthermore, the ultimate V_u capacity is higher than the HF600/5 which is not reasonable. However, the results are reported in Table 27. The comparison between the curves of HF400/7 is reported in the Annex 2, but they are not explainable physically speaking, according to theoretical considerations.

2.3.2.3 HF400h/6

Table 28 - Control parameters for HF400h/6

HF400h/6	δ_i	σ_b	σ_t	P_{de}	V_u
Manual evaluations	2.03	-18.53	1.32	300.93	-
Experimental results	-	-	-	-	420.00
STKO predictions	1.63	-16.21	0.57	301.17	379.44
Ratio STKO predictions/manual evaluations	0.80	0.87	0.43	1.00	-
Ratio STKO predictions/Experimental results	-	-	-	-	0.90

The HF400h/6 beam has a height higher than the other elements. As Table 28 shows, the STKO – manual results comparison provides worse results than the HF400/7 and HF600/5. Furthermore, V_u comparison with the experimental presents an error of 10% which refers to a good prediction.

2.3.2.4 HF260/9

Table 29 - Control parameters for HF260/9

HF260/9	δ_i	σ_b	σ_t	P_{de}	V_u
Manual evaluations	1.77	-17.21	0.14	262.46	-
Experimental results	-	-	-	-	325.58
STKO predictions	1.70	-16.17	0.22	255.00	286.72
Ratio STKO predictions/manual evaluations	0.96	0.94	1.57	0.97	-
Ratio STKO predictions/Experimental results	-	-	-	-	0.88

The HF260/9 shows the smallest flange and as a consequence the minimum ultimate shear capacity. The numerical model provides a lower value of V_u respect to the experimental one but good agreement for the manual evaluations as reported in Table 29.

2.3.2.5 Final results and comment for pre-stressed beams

Table 30 - Overall view for the Cuenca's pre-stressed beams

Cuenca's beams	δ_i	σ_b	σ_t	P_{de}	V_u
H600/5	0.97	0.97	0.60	0.96	1.01
H400/7	0.97	0.97	0.18	0.96	0.91
H400h/6	0.80	0.87	0.43	1.00	0.80
H260/9	0.96	0.94	1.57	0.97	0.88
μ	0.93	0.94	0.70	0.97	0.90
SD	2.03%	0.57%	110.98%	0.11%	2.32%

In Table 30, the overall view is reported. The model shows a good theoretical reliability according to the manual calculation except for the σ_t , but this parameter presents high dispersion and high error due to the very low values which it assumes. As far as the ratio between STKO prediction and experimental results is concerned, there is a mean error value of 10% and a SD of 2.3 %. Furthermore, the damage prediction presents for all four beams a pattern absolutely attached to reality and physically explainable. The final conclusion is that the numerical models are able to predict reasonable behaviour and ultimate shear capacity for the bonded pre-stressed HPFRC beams.

3.FEA: numerical representation of experimental results with *JCONC*

JCONC is a nonlinear Finite Element program to model the behavior of two-dimensional reinforced concrete structures. The *JCONC* program implements the *Elastic-Plastic Stress Field method* (EPSF) developed by M. Fernandez Ruiz and Muttoni [42].

The EPSF method allows to generate a stress field solution in equilibrium with the external forces, respecting the plastic material properties and the negative influence of transverse cracking on concrete compressive strength. The exact solution represents the theoretical maximum load carrying capacity which can be calculated using the stress field. The method verifies the system equilibrium and the compatibility condition of the failure mechanism satisfying the lower and the upper bound plasticity theorem.

The *JCONC* approach is obtaining a stress field iteratively for each load step by assessing the stress in concrete and reinforced based on constitutive relationship and imposed deformation. Furthermore, *JCONC* determines the ultimate conditions in terms of displacement, load and stresses and consequently, it does not allow to obtain the load-displacement curve automatically.

Unlike *STKO Opensees*®, *JCONC* can run as a standalone application and requires the recent version of the *Java runtime* environment as far as the path to the *Java* environment. The program does not have a graphical interface for the input, but the user has to code the entire model in *Java* coding language.

3.1 Case study 1: Minelli's experimentations

3.1.1 FEM Modelling strategies

In the following section, the main characteristics of the models in terms of geometry, mesh, material properties, boundary conditions, loads, and the numerical algorithm used to model Minelli's beams are described.

3.1.1.1 Geometry

The geometry is defined by a *Java* code. In particular, the input data are the coordinates of each node which define the discretization of the element. For simplification purposes, it has been chosen to model only a half of the beam and apply the symmetry conditions. The geometry has been created in order to obtain a mesh size of 250 mm for H500 while of 100 mm for H1000 and H1500. The final result is a bidimensional model made of triangular elements as shown in Fig. 58. The bar is defined between consecutive nodes which are the same used to create the beam body, in order to assure the bond between the two elements.

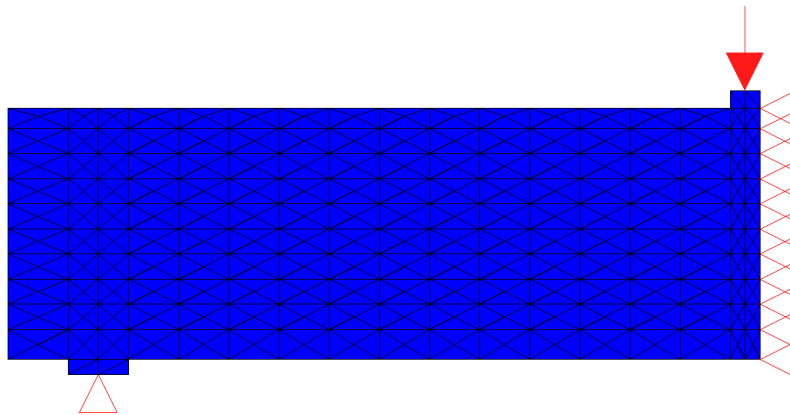


Fig. 58 - JCONC geometry for H500FRC50

3.1.1.2 Material properties

- Concrete

The concrete behavior is considered orthotropic in the two principal directions. The concrete stress-strain relationship considered is elasto-plastic both in traction and compression, as it is shown in Fig. 59.

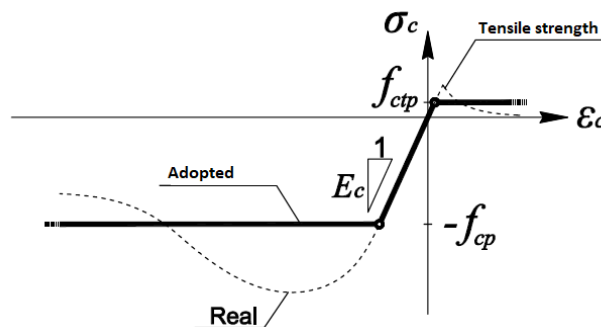


Fig. 59 - Concrete stress-strain relationship in JCONC

The command is *conc3N* and the compression input data are:

- f_{cp} : plastic resistance strength;
- E: elastic modulus.

In particular, the f_{cp} is reduced by a η coefficient evaluated as (24):

$$\eta = \left(\frac{f_{c0}}{f_{cm}} \right)^{1/3} \quad (24)$$

- f_{c0} is set equal to 30 MPa as reported in [42];
- f_{cm} is equal to the mean characteristic compressive strength reported in Fig. 12.

In Table 31, the η , f_{cp} and the E values are reported:

Table 31 - Compressive input data for Minelli's beams in JCONC

Concrete type	η [-]	f_{cp} [MPa]	E [MPa]
FRC50	0.97	31	30800
FRC75	0.96	32	32100

The tension input datum is f_t . In particular, the f_t is considered equal to the $\frac{1}{3}$ of $f_{R,3}$ for the FRC50 and FRC75. In Table 32, the f_t is reported for the Minelli's beams.

Table 32 - Tensile input data for Minelli's beams in JCONC

Concrete type	f_t [MPa]
FRC50	1.67
FRC75	2.00

- Steel

The steel stress - strain relationship is considered elasto-plastic as for the concrete [Fig. 60].

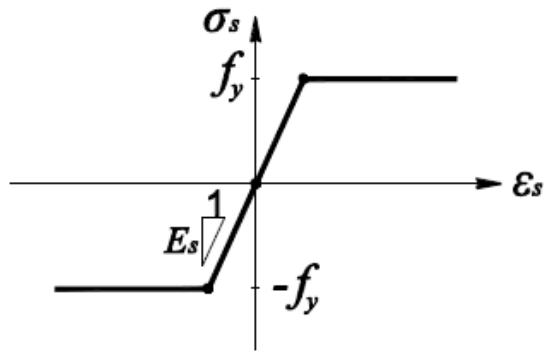


Fig. 60 - Steel stress-strain relationship in JCONC

The input data are:

- f_y : yielding stress;
- E : elastic modulus.

The values are the same reported in Table 3. The bars are considered perfectly adherent to the concrete.

3.1.1.3 Elements properties

The reinforcement bars are modeled using the link 1D finite elements with uniaxial behavior. The strain state is obtained based on a given displacement and the FE length. The concrete is modelled using constant strain triangles and the strain state is obtained imposing the displacement, as for the rebars. Considering the principal strain parallel to the principal stresses, the concrete stresses can be directly obtained considering the stress-strain relationship.

3.1.1.4 Boundary conditions

The boundary conditions are assigned by applying to the support plates middle node the displacement value in y and x direction (U_y and U_x) equal to 0 in both directions in order to simulate a pin. Furthermore, the symmetric condition is imposed to assign a U_x equal to zero to the node of the symmetry axes.

3.1.1.5 Load

JCONC allows the input only concentrated force. In the Minelli's beam a concentrate force is applied at the extreme node of the upper plate for H500 and H1000. Therefore, the load is discretized in 5 concentrate forces for H1500 to avoid numerical instabilities

induced by the beam dimensions with respect to the plate ones. The force is equal to 500 kN for H500 and 1500 kN for H1000 and H1500.

3.1.1.6 Analysis

The EPSF are developed based on the imposed displacement fields by 250 iterations. The process starts with a linear elastic FEM calculation for the steel and the concrete, considering an infinite strength in tension and compression. Once it is obtained, the initial displacement field, the materials assume elasto-plastic behavior. Afterwards, the stress, strain and nodal force are obtained assuring the equilibrium in each node. The equilibrium always results in having some residual forces which are used to correct the initial displacement field. The correction consists of moving the node at a certain rate by the *Newton-Raphson algorithm*. The analysis diverges if the applied load is higher than the model's strength. The relative error based on the un-equilibrated residual force is plotted at the end of the analysis. The final error accepted was set equal to 3 kN.

3.1.2 Fiber Reinforced Concrete: result and discussion

The JCONC results consist of the stress and strain state at the ultimate failure condition. In Table 33, $V_{u, JCONC}$ is the numerical ultimate shear strength $V_{u, test}$ is the experimental one while $d_{u, JCONC}$ and $d_{u, test}$ are respectively the ultimate numerical and experimental displacement.

Table 33 - JCONC's results for the Minelli's FRC beams

ID	$V_{u, test}$	$V_{u, JCONC}$	$V_{u, JCONC}/V_{u, test}$	$d_{u, test}$	$d_{u, JCONC}$	$d_{u, JCONC}/d_{u, test}$
H500FRC50	236	231	0.98	23.18	7.42	0.32
H1000FRC50	264	392	1.48	11.68	13.2	1.13
H1500FRC50	471.5	560	1.19	21.18	18.6	0.88
H500FRC75	231	238	1.03	9.07	7.38	0.81
H1000FRC75	343	409	1.19	14.31	12.7	0.89
H1500FRC75	541.5	570	1.05	23.2	17.3	0.75
μ	-	-	1.15	-	-	0.80
SD	-	-	16.83%	-	-	35.61%

The ratio $V_{u, JCONC}/V_{u, test}$ presents a general error between the $\pm 20\%$. In particular, the JCONC analysis presents an outlier for the H1000FRC50 while the others values are

acceptable. Besides, also the predictions of the ultimate displacement lead to an error of $\pm 20\%$ with an out of trend value for the H500FRC50.

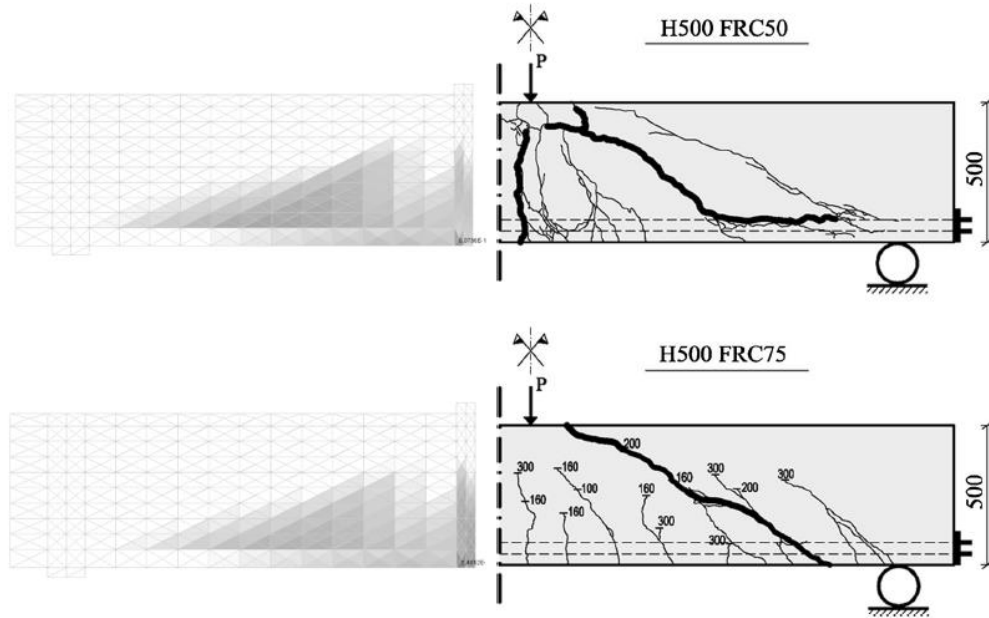


Fig. 61 - Comparison between numerical (left figure) and experimental (right figure) crack pattern for H500

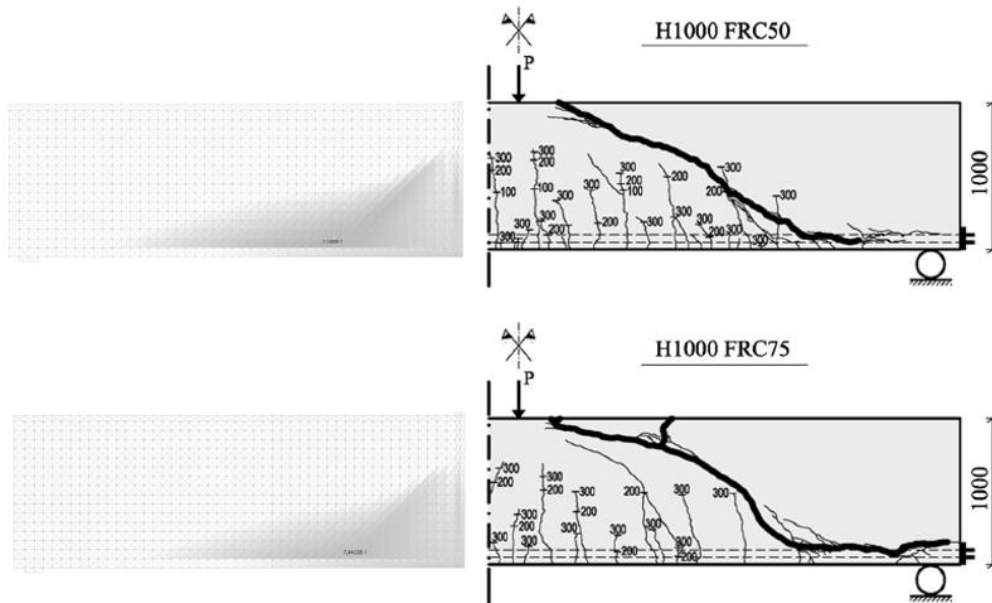


Fig. 62 - Comparison between numerical (left figure) and experimental (right figure) crack pattern for H1000

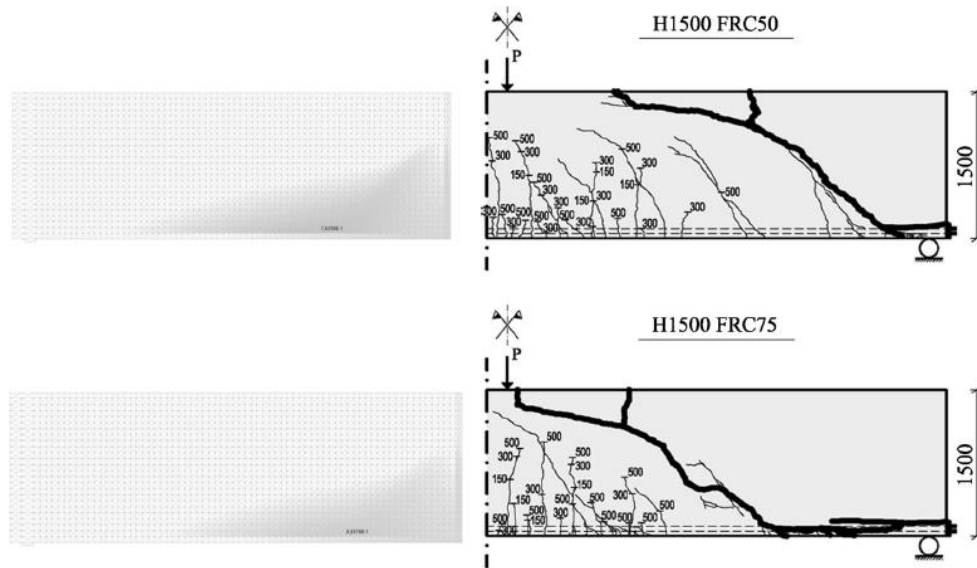


Fig. 63 - Comparison between numerical (left figure) and experimental (right figure) crack pattern for H1500

Fig. 61, Fig. 62 and Fig. 63 present the comparison between the final *JCONC* crack pattern and the experimental one for FRC50 and FRC75 beams. The *JCONC* plots show a mixed flexural-shear failure for both the H500FRC50 and H500FRC75 as the authors assert. The H1000FRC50, H1000FRC75, H1500FRC50, H1500FRC75 develop diagonal cracks which refer to a shear failure as the reference underlines reports. Moreover, the numerical pattern is not completely attached to the experimental one since the principal failure cracks are located in different positions.

It must be underlined that *JCONC* is a plastic model which might not be adequate for discrete failures. Despite this, it is able to predict a reasonable shear strength compared to the experimental results for the Minelli's beams.

3.2 Case study 2: Cuenca's experimentations

3.2.1 FEM modelling strategies

The FEM modelling strategies for the Cuenca's beams is almost the same used for the Minelli's beams except for the introduction of pre-stressing. Afterwards, in the following section, the variation of the model strategies from the case study 1 are reported. Hence, the missing information is consultable in §3.1.1. The experimentation data to which it refers are reported in § 2.3.

3.2.1.1 Geometry

The geometry is defined by a *Java* code. As for *STKO Opensees*© modelling, the tendons' layout has been simplified, defining a unique equivalent cable for the bottom and upper flange. The variation of thickness is reproduced with the same strategies presented in §3.1.1.1. In Fig. 64 the colours refer to the different thickness. The geometry has been created in order to obtain a mesh size of 250 mm for HF600/5, HF400/7, HF400h/6 and HF260/9. The cable nodes are connected to the concrete one in order to define the bonded condition.

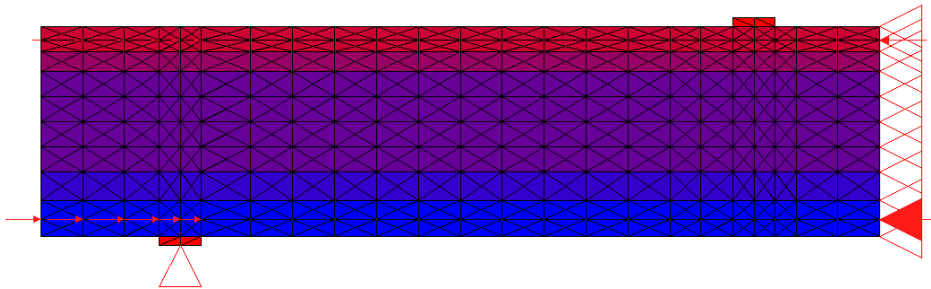


Fig. 64 - JCONC geometry for HF600/5

3.2.1.2 Material properties

In Table 34, the η , f_{cp} and the E values are reported:

- Concrete

Table 34 - Compressive input data for Cuenca's beam in JCONC

Concrete type	η [-]	f_{cp} [MPa]	E [MPa]
HF600/5	0.77	51	40700
HF400/7	0.78	50	40700
HF400h/6	0.79	47	40700
HF260/9	0.77	51	40700

The tension input datum is f_t . In Table 35, the f_t is reported for the Cuenca's beams.

Table 35 - Tensile input data for Cuenca's beams in JCONC

Concrete type	f_t [MPa]
HF600/5	1.85
HF400/7	1.59
HF400h/6	1.99
HF260/9	1.89

- Pre-stressed steel

The steel stress - strain relationship is considered elasto-plastic as for the concrete. Moreover, the presence of pre-stressing requires the reduction of yielding strength to take in account the initial stress $\sigma_{p,inf}$ imposed, equal to 999 MPa. Based on the previous consideration the input data for the cable steel are:

- $f_{s,r}$: yielding stress (25);
- E: elastic modulus.

$$f_{s,r} = f_s - \sigma_{p,inf} \quad (25)$$

In Table 36, the $f_{s,r}$ and E are reported for the tendons.

Table 36 - Steel input data for Cuenca's beams in JCONC

Steel type	$f_{s,r}$ [MPa]	E [MPa]
Y 1860 S7	861	210000

The cables are considered perfectly bonded to the concrete.

3.2.1.3 Elements properties

The tendons are modeled using the link 1D finite *cable* instead of *bars*. The two elements work in the same manner but the first element requires an additional input which is the *sigma_0* equal to the initial stress $\sigma_{p,inf}$. Afterwards, the program integrates the $\sigma_{p,inf}$ on the cable cross section in order to obtain the final pre-stressing force acting on concrete.

3.2.1.4 Load

The pre-stressing action is simulated by applying a concentrated load on the element surface to act as an anchorage force and modifying the yielding strength as previously explained in § 3.1.1.2. The anchorage forces are obtained by the integration of the initial stress on the cable cross sections. Hence, for the bottom equivalent cable the force is equal to 1258.74 kN while for the upper equivalent cable is equal to 279.75 kN. Finally, the vertical load is applied as a concentrate force equal to 2500 kN on a steel plate of 150x30x1000 mm.

3.2.2 Pre-stressed fiber reinforced concrete: result and discussion

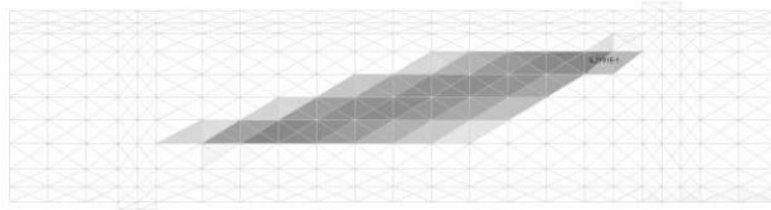
The *JCONC* results consist of the stress and strain state at the ultimate failure condition. In Table 37, $V_{u, JCONC}$ is the numerical ultimate shear strength $V_{u, test}$ is the experimental one while $d_{i, JCONC}$ and $d_{i, manual}$ are respectively the ultimate numerical and manual initial uplift displacement evaluated as reported in Annex 2.

Table 37 - *JCONC*'s results for the Cuenca's HPFRC beams

ID	$V_{u, test}$	$V_{u, JCONC}$	$V_{u, JCONC}/V_{u, test}$	$d_{i, manual}$	$d_{i, JCONC}$	$d_{i, JCONC}/d_{i, manual}$
HF600/5	347.5	535	1.54	1.81	1.68	0.93
HF400/7	389.5	580.00	1.38	1.79	1.65	0.80
HF400h/6	420	502.00	1.29	2.03	1.63	0.92
HF260/9	325.58	515.00	1.58	1.77	1.58	0.89
μ	-	-	1.45	-	-	0.89
SD	-	-	5.61%	-	-	1.00%

The ratio between $V_{u, JCONC}/V_{u, test}$ has a high general error of 45% and a low dispersion of values which refers to the inability of the model to predict the ultimate shear capacity for all the four beams. Considering that *JCONC* is a plastic model, it is possible to understand why the program provides unadequate results. In fact, it tries to model the concrete as an elasto - plastic material when in reality it is a quasi-brittle one. The solution could be more attached to the experimental one if the transversal reinforcement is added since the final reinforced concrete has a behaviour closer to the elasto-plastic law. Furthermore, the uplift predictions are in good agreement with the experimental results. This consideration demonstrates the previous statement because the uplift is a displacement developed in the elastic stage when the nonlinearity of concrete is not dominant. Hence, the concrete has a behaviour more attached to the elastic one represented by the first branch of *JCONC*'s concrete material model, reported in Fig. 59.

HF600/5



HF400/7

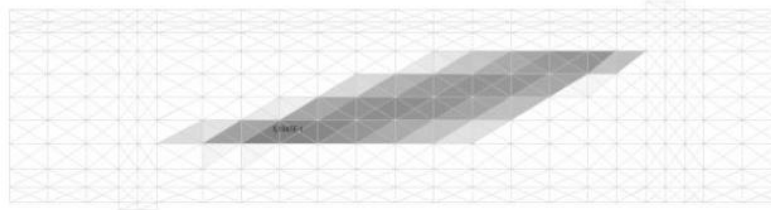
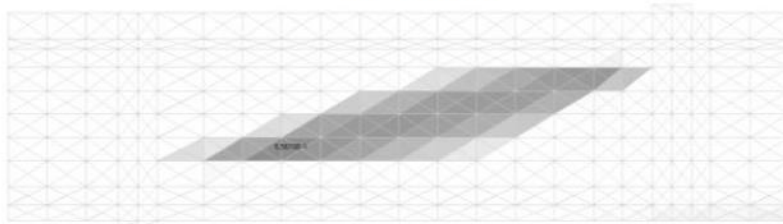


Fig. 65 - JCONC crack pattern for HF600/5 (upper figure) and HF400/7 (lower figure)

HF400h/6



HF260/9

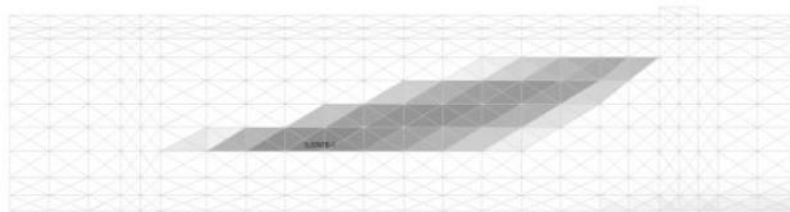


Fig. 66 - JCONC crack pattern for HF400h/6 (upper figure) and HF260/9 (lower figure)

In Fig. 65 and Fig. 66, JCONC crack damage is reported. The pictures show a clear shear failure as it was expected. Thus, the program permits to predict the final failure even though the ultimate shear strength has an unacceptable approximation. Moreover, reducing the f_{cpt} or limiting the tensile strain, better results could be obtained.

4. FEA: prediction of experimental results with *STKO Opensees*©

The modelling of the previous experimental results of Minelli and Cuenca's beams has been useful to calibrate and provide a good modelling to obtain reliable results. Hence, the final step of this work is to predict blindly the behaviour of HPFRC beams designed by Universidad Politécnica de Madrid (UPM), partnered with Acciona S.A, during the test stage. In the following section, the FEM strategies modelling and results are presented.

4.1 Case study 3: UPM and Acciona S.A. beams

The object of the UPM research project is the design of structural elements with a new HPFRC mix design. The new material will be used in U girders for continuous unbonded prestressed bridge in order to avoid the adoption of transversal reinforcement. Hence, in order to pursue the final research project aim, an experimental campaign will be carried out to measure the shear capacity of HPFRC in UPM structural LAB.

The eight beams being tested have a symmetric IPE cross section with a height of 800 mm and a a/d ratio of 3.42, designed to fail due to shear. The layout of the reinforcement is composed of 11 tendons of 7 wires (equal cross section of 150 mm²), 9 in the bottom flange disposed on 3 layers, and 2 in the upper flange (these latter are always bonded). The longitudinal cables' layout differs from each other for the length of the bonded and unbonded portion and for the level of prestressing action. The prestressing stress is equal to 1116 MPa which already takes into account the prestressing losses.

The prediction of the experiment results is provided for the BMI12 and UMI12 which present the highest level of prestressing. The BMI12 tendons are bonded for all the length, Fig. 67.

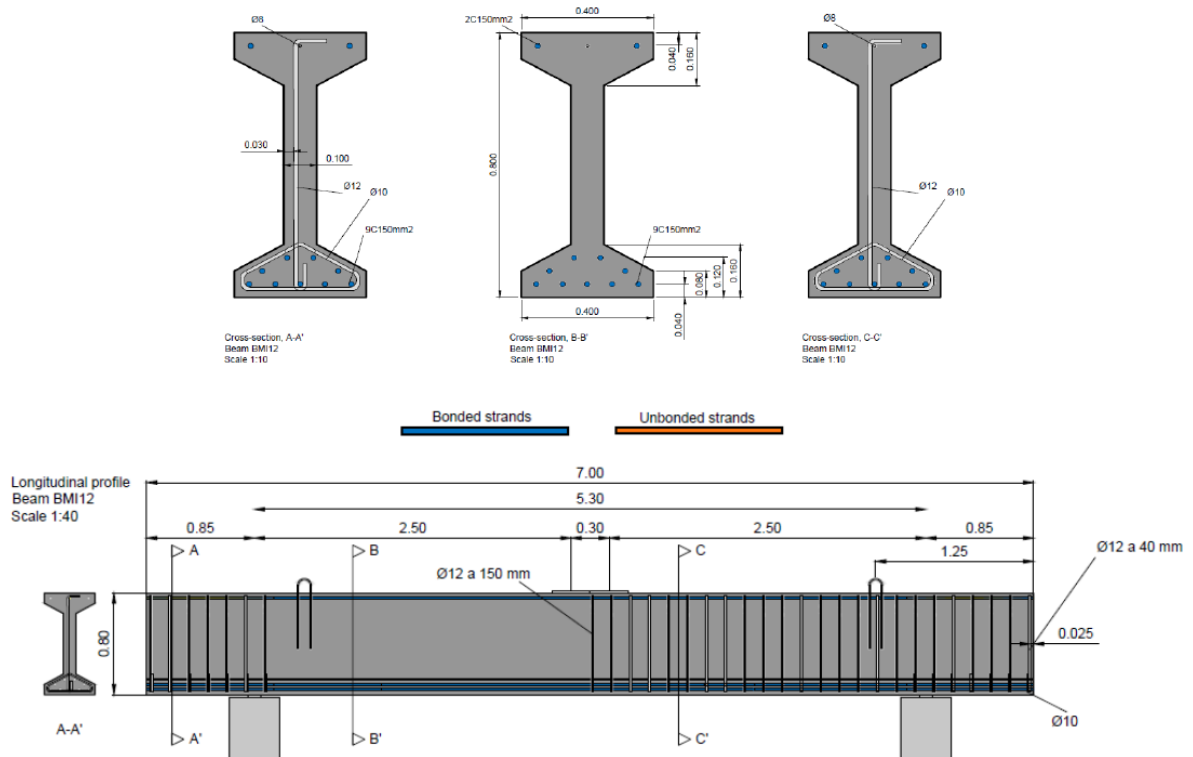


Fig. 67 - BMI12 cross section (upper figure) and longitudinal profile (bottom figure)

The UMI12 presents unbonded tendons inside the shear span, Fig. 68. The unbonded parts have different lengths for the three layouts of the bottom tendons.

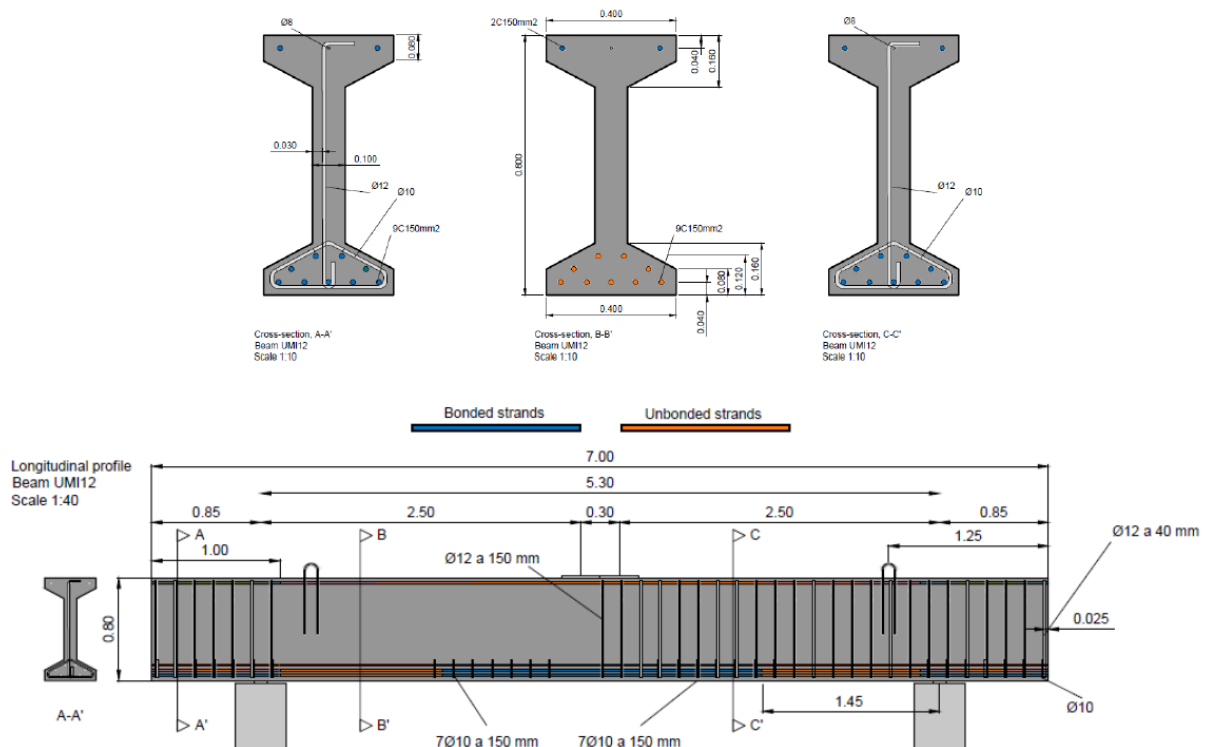


Fig. 68 - UMI12 cross section (upper figure) and longitudinal profile (bottom figure)

The test set-up consists of a four points bending test realized by the imposition of load on two steel plates of 250x10x500 mm. The static scheme is simply supported since the supports are designed to have the kinematic characteristic of a pin and a roller, through the use of steel cylinders on steel plates of 75x10x500 mm [Fig. 67 and Fig. 68].

As far as the concrete properties are concerned, the UPM researchers carried a cylindrical compressive strength test (UNE-EN 12390-3), the Young modulus test (UNE-EN 12390-13) and three points bending test on notched specimens (UNE-EN 14651). The results are reported in Table 38.

Table 38 - Concrete properties of HPFRC

Concrete properties	HPFRC
f_{cm} [MPa]	120
f_{ctm} [MPa]	5.33
$f_{R,1}$ [MPa]	17.8
$f_{R,3}$ [MPa]	16
E [MPa]	46250

4.1.1 FEM modelling strategies

The FEM modelling strategies are the same used for the case studies 1 and 2 and explained in § 2.2.1 and in §2.3.1. Moreover, the following part reports the differences from the previous models in terms of geometry definitions, material and element properties, conditions and analysis setting.

4.1.1.1 Geometry

The IPE section is characterized by the different thickness of its part. The UPM's beams' cross section is composed of two rectangular flanges which are linked to the web by trapezoidal elements. In the FEM model, the trapezoidal elements are represented by a rectangular box with an area equal to the original one. In the Annex 2 the Finite Element equivalent sections are reported. The tendons layout is simplified by assigning a unique equivalent cable with a concrete cover of 40 mm for both upper and bottom flange. The different unbonded lengths are solved considering the weighted average between the different tendons.

In the pretensioned member, a transfer length is needed to restore the strain compatibility between the steel and concrete due to the prestress action. Along this length, the prestress force increases from 0 to the maximum value equal to the integration of initial stress on the cable cross section. The models simulate the real distribution of prestressing force by the discretization of cross section area. In particular, the transfer length is equal to 500 mm, divided in 10 parts of 10 mm in both UMI12 and BMI12. The small lengths have been unified with the command *Wire* which assures the connection of extreme nodes of two consecutive elements in a final one.

4.1.1.2 Interaction

In these models, the interactions are used to assign the bond between cable and concrete only for the bonded portion of cable. In particular, the interaction has been realized for each part of the wire.

4.1.1.3 Physical properties

- Material properties for concrete

In Table 39, the values used for the HPFRC are reported.

Table 39- Concrete compressive parameters inputs of Minelli's beams

Concrete type	E [MPa]	f_{c0} [MPa]	f_{cp} [MPa]	f_{cr} [MPa]	G_c [N/mm]
HPFRC	46250	48	120	24	43

In Table 40, there are reported f_t , f_{Ftu} and G_t for each material.

Table 40 - Concrete tensile parameters inputs of Minelli's beams

Concrete type	f_t [MPa]	f_{Ftu} [MPa]	G_t [N/mm]
HPFRC	3.55	5.33	13.33

- Material properties for cable's steel

The stress-strain relationship of the steel has been modelled with the material model *Steel01* which considers an elastoplastic law. The parameters inputs are the yielding stress f_y and the elastic modulus E. In these models, the prestressing action is assigned as an

external horizontal distributed force. Hence, the yielding steel strength must be reduced to take the initial stress equal to 1116 MPa into account.

$$f_y = f_{pk} - \sigma_{p0} \quad (26)$$

where:

- f_{pk} : is the yielding stress equal to 1860 MPa;
- σ_{p0} : is the initial prestressing stress equal to 1116 MPa.

In Table 41, the value input datum is reported.

Table 41 - Steel tendon parameters input of UPM's beams

Steel type	E [MPa]	f_y [MPa]
Y 1860 S7	195000	744

- Rebars section

The rebars section has been created with the command *sections>Fibers* which allows the creation of a general shaped section and the assignment of the material property which, in this case, is the steel for reinforcement. In the bottom tendon the transfer length presents 10 different cross sections with a diameter between 6.6 to 20.7 mm which corresponds to the equivalent area of 9 tendons. Indeed, in the upper tendons the transfer length is discretized in 10 cross sections with a diameter from 3.09 to 9.77 mm [Fig. 69 and Fig. 70].

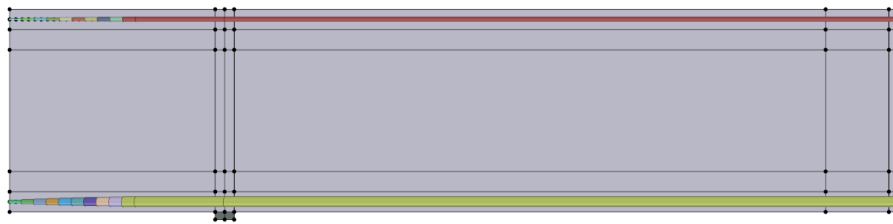


Fig. 69 - Physical properties of BMI12

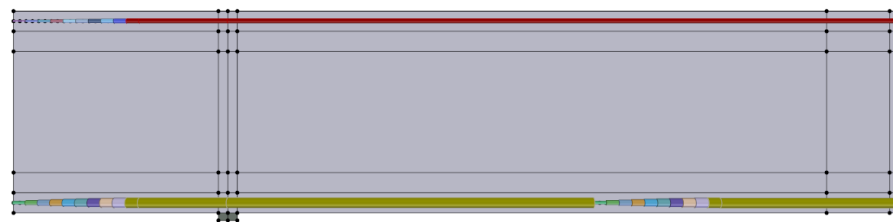


Fig. 70 - Physical properties of UMI12

- Special purpose for Physical Properties

In the UPM's models, a special purpose has been created for the rebars with the command *BeamSectionProperty* because the aim was to create subsequently an 1D Finite Element.

4.1.1.4 Element properties

Unlike the case study 1 and 2, the cable is modelled as a FE beam with the command *beam_column_elements.dispBeamColumn* due to the presence of an unbounded part which is not connected to the concrete matrix. In particular, the truss element generates a numerical singularity of the stiffness matrix because the extreme unconnected points of the unbounded part have no stiffness. The *beam_column_elements.dispBeamColumn* develops 5 integration points on its length and it constructs a *forceBeamColumn* element object which applies the *Gauss-Lobatto* integration [43].

4.1.1.5 Conditions

Under the folder *Condition*, the constraints, the restraints and the load have been defined. The constraints and restraints are the same used for case study 1 and 2 reported in § 2.2.1.5

- Load

The load is applied as distributed on a length equal to the plate width (250 mm) with the command *EdgeForce* equal to 5000 N/mm. The prestressing action is assigned as a uniform distributed horizontal load on the transfer length with the command *EdgeForce*. The prestressing forces have been evaluated considering the integral of initial stresses, σ_p , on the cable equivalent cross section A_p (27). Afterwards, the force has been distributed uniformly on the transfer length, l_T , equal to 500 mm (28).

$$F_p = A_p \cdot \sigma_{p0} \quad (27)$$

$$f_p = \frac{F_p}{l_T} \quad (28)$$

In Table 42, the F_p and f_p are reported for the bottom and upper cable.

Table 42 - Horizontal distributed prestressing force for UPM's beams

Cable	F_p [N]	f_p [N/mm]
Bottom	1506600	3013.2
Upper	334800	670

However, the forces assume opposite signs if they are applied on the left transfer length (+) or the right one (-) to assure symmetry condition.

4.1.1.6 Analysis steps

The pre-stressing action is given by adding a new analysis step before the loading of structures. The analysis steps are:

- Recorder
- Patterns

The first pattern applied is the boundary condition one. Consequently, the load pattern has been added for the prestressing forces, assigning a constant time series previously defined in the section *definitions*.

- Analysis step 1

The analysis features are set in the *AnalysesCommand* which allows the user to define the different linear and nonlinear available analysis tools. For the analysis step 1, the following options have been defined:

- *Analysis type command*: static analysis;
- *Constrain command*: *PenaltyMethod* with default penalty values has been set;
- *Numberer Command*: *Parallel Reverse Cuthill-McKee Numberer* because the analysis is split in more than one processor;
- *System Command*: *Mumps*;
- *Algorithm Command*: *Newton Algorithm*;
- *Test Command*: *Norm Displacement Increment*;
- *Integrator Command*: *Load control* with duration equal to 1;
- *Analyze*: *Fixed Time Step* with a number of step equal to 50;
- Second pattern: applying of the vertical load previously defined in Conditions.

- Analysis Step 2: setting as explained in § 2.2.1.6.

4.1.2 Result and discussion

The post-processing of UPM beams has taken in account the evaluation of the load - displacement curve, the bottom fiber concrete stress, σ_b , and the cable stress, σ_p , at prestressing moment, t_0 , and at the probable failure which is the peak load, t_f . These considerations are made in order to detect if the models are capable of representing an experimental behavior in agreement with analytical calculations.

4.1.2.1 BMI12

In Fig. 71, the load-displacement curve of BMI12 is plotted. The curve shows an uplift equal to 2.30 mm induced by the pre-stressing action, followed by a linear branch and a drop at maximum shear capacity equal to 475 kN. The peak load should be the point of beam failure.

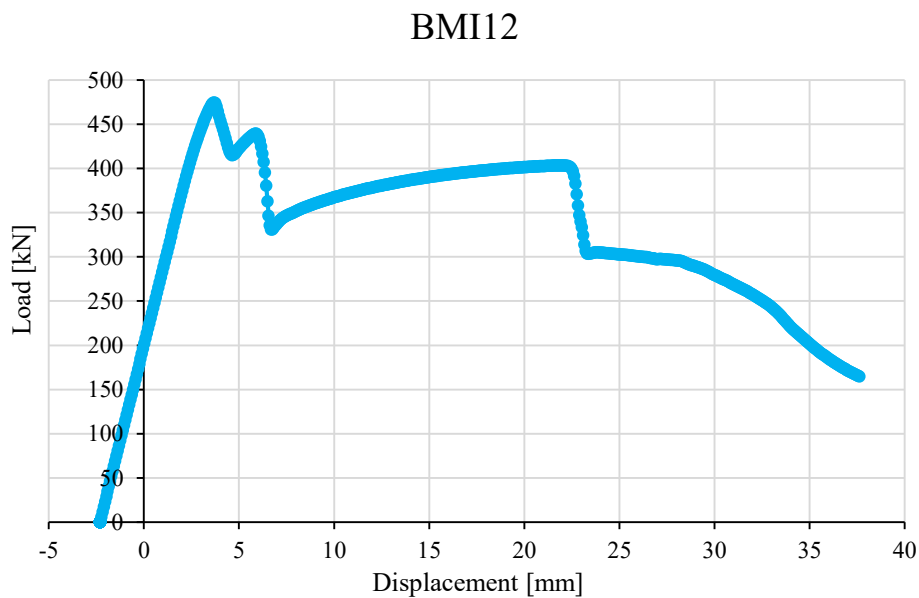


Fig. 71 - Load-displacement curve for BMI12

Table 43 - Control parameters for BMI12 for STKO Opensees

BMI12	δ_0	σ_b	σ_p	V_u
Manual evaluations	2.37	-23.92	1020.38	-
STKO predictions	2.30	-23.27	1022.20	475
Ratio STKO predictions/Manual evaluations	0.97	1.00	1.00	-

In Table 43, the manual evaluations are compared against the STKO predictions for the uplift δ_0 , the σ_b and σ_p in the midspan. The comparisons are in good agreement. Finally, the ultimate shear capacity, V_u , is reported. In Table 44, the displacement δ , the σ_b , the σ_p at t_0 are reported. The evaluations are made on 12 points at t_0 at x distance from the extreme vertex. The box cell colour cyan is for the transfer length parts while the blue one is for the bonded portions.

Table 44 - Control parameters for BMI12 at t_0

1 st step → no vertical load				
Sections ID	x [mm]	δ [mm]	σ_b [MPa]	σ_p [MPa]
S ₁	0	-2.00	-1.08	1112.62
S ₂	250	-1.26	-21.05	1044.58
S ₃	500	-0.61	-30.78	997.82
S ₄	750	-0.14	-27.22	1017.50
S ₅ - pin	850	0.00	-9.14	1026.78
S ₆	1000	0.28	-24.15	1019.98
S ₇	1250	0.66	-23.19	1022.40
S ₈	1575	1.10	-23.21	1022.17
S ₉	2300	1.83	-23.21	1022.43
S ₁₀	2800	2.14	-23.27	1022.43
S ₁₁	3300	2.29	-23.27	1022.43
S ₁₂ - midspan	3500	2.30	-23.27	1022.22

In Table 45, the δ , σ_b , σ_p at t_f (139th step load) are reported which corresponds to the maximum load equal to 475 kN.

Table 45 - Control parameters for BMI12 at t_f

139 th step → vertical load				
Sections ID	x [mm]	δ [mm]	σ_b [MPa]	σ_p [MPa]
S ₁	0	0.35	-1.08	1112.62
S ₂	250	0.40	-20.93	1044.92
S ₃	500	0.29	-30.17	998.52
S ₄	750	0.09	-29.58	1012.59
S ₅ - pin	850	0.00	-8.84	1034.61
S ₆	1000	-0.26	-22.48	1022.95
S ₇	1250	-0.67	-16.73	1044.33
S ₈	1575	-1.21	-12.64	1061.25
S ₉	2300	-2.43	-3.82	1100.14
S ₁₀	2800	-3.22	3.54	1126.00
S ₁₁	3300	-3.65	3.47	1186.93
S ₁₂ - midspan	3500	-3.70	3.48	1201.78

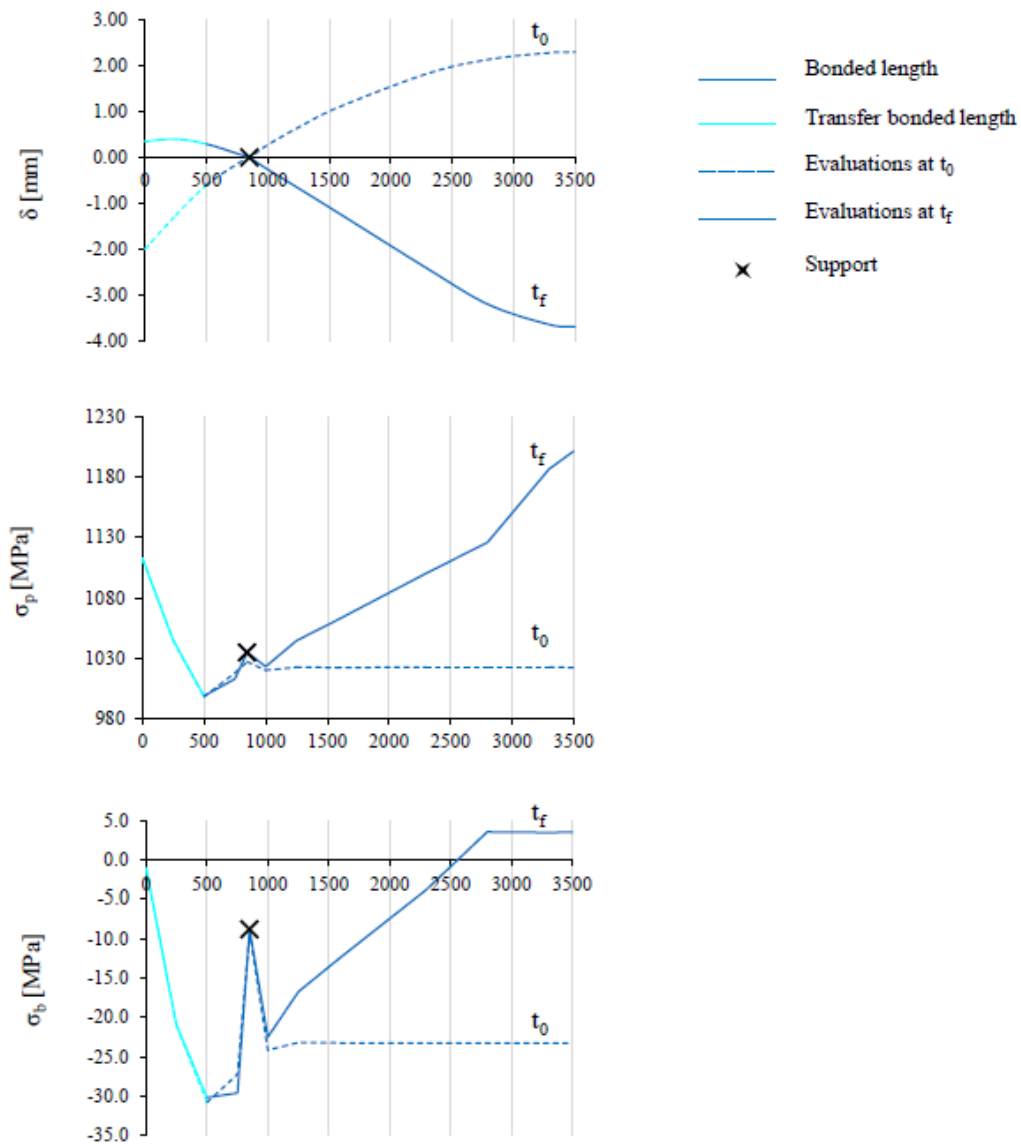
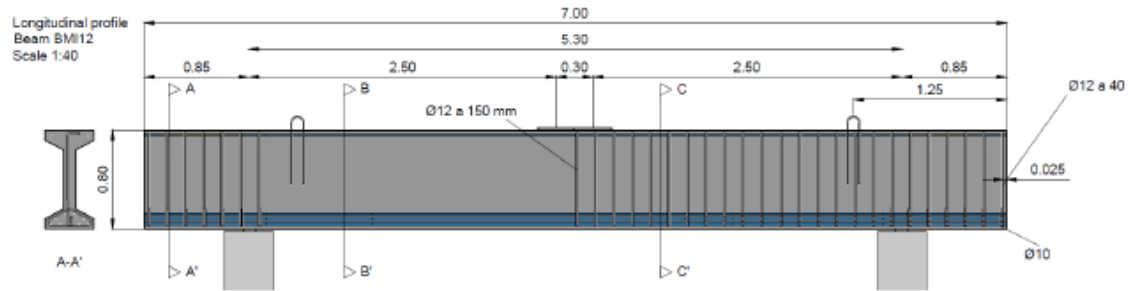


Fig. 72 - δ , σ_p , σ_b at t_0 and t_f for BMI12

In Fig. 72, the δ , σ_p , σ_b are plotted on the half beam length. The displacement defines a convex curvilinear deformed at t_0 , induced by the negative constant moment acting on the

beams. While, the deformed is a concave curve at t_f due to the positive moment induced by the vertical load.

The model is perfectly able to recognize the compatibility of the σ_p in the transfer length at t_0 and t_f . Moreover, the value is constant from the support to the middle span at t_0 and it increases due to the bonded condition at t_f .

Finally, the σ_b trend increases in the transfer length with a discontinuity in the support area caused by the restraint of horizontal displacement imposed by the pin. Furthermore, it maintains a constant value of 23.21 MPa in the support - midspan length. Considering the values at t_f , the σ_b has the same trend in the transfer part since it is not affected by the positive moment imposed, followed by a positive slope up to 2800 mm. Afterwards, it continues with a constant branch as it was expected since the beam is subjected to a four points bending test.

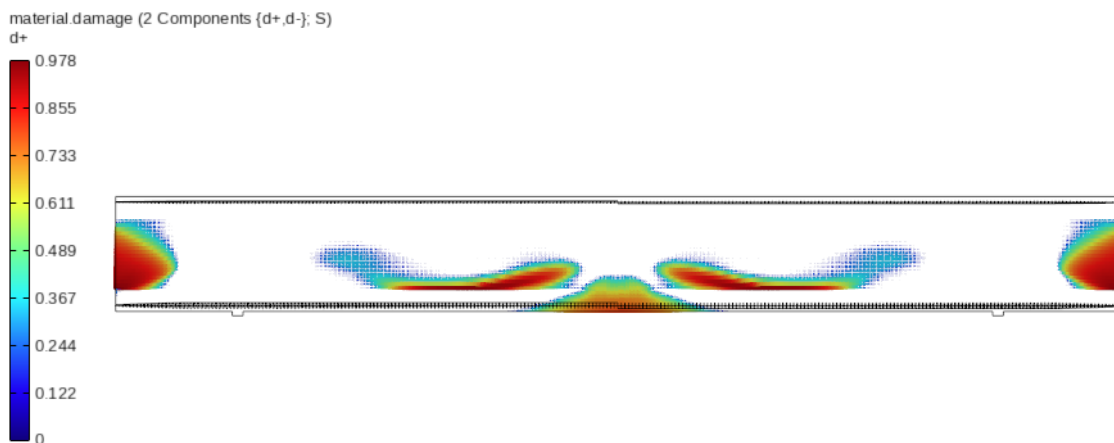


Fig. 73 - Crack damage pattern of BMI12 at t_f

Fig. 73 represents the crack damage pattern at peak load. The plot shows small flexural and diagonal cracks. Moreover, the failure can be induced by shear actions as they are more extended. The prediction reflects what was expected since the beam is designed to fail due to shear in order to analyse its final shear capacity.

4.1.2.2 UMI12

In Fig. 74, the load-displacement curve of UMI12 is plotted. The curve shows an uplift equal to 2.33 mm induced by the pre-stressing action, followed by a linear branch and a drop at maximum shear capacity equal to 467 kN. The peak load should be the point of beam failure during the test.

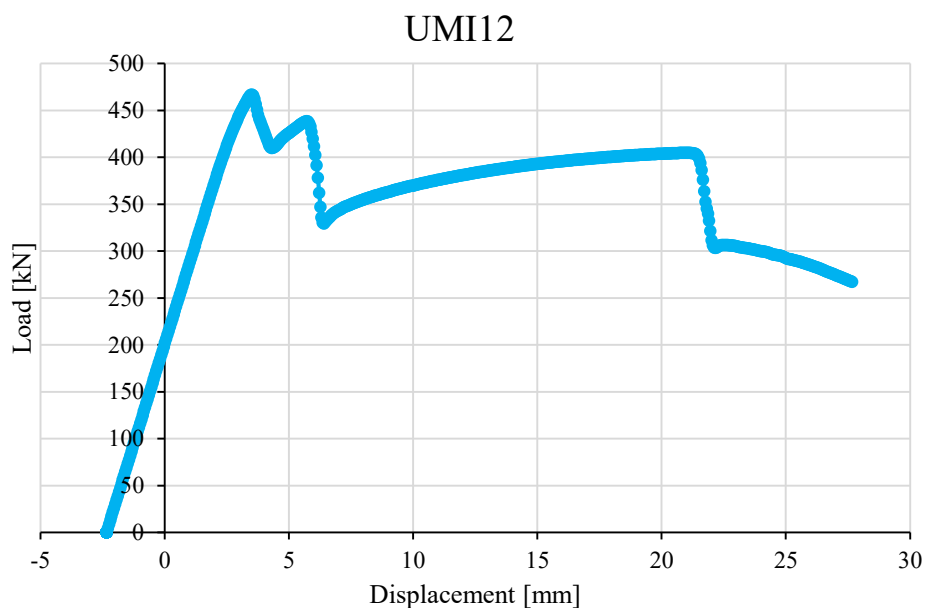


Fig. 74 - Load-displacement curve for UMI12

In Table 46, the manual evaluations are compared against the STKO predictions for the uplift δ_0 , the σ_b and σ_p in the midspan. The comparisons are in good agreement. Finally, the ultimate shear capacity, V_u , is reported.

Table 46 - Control parameters for UMI12 for STKO Opensees

BMI12	δ_0	σ_b	σ_p	V_u
Manual evaluations	2.37	-23.92	1020.38	-
STKO predictions	2.33	-23.28	1022.19	467
Ratio STKO predictions/manual evaluations	0.98	1.00	1.00	-

In Table 47, , the displacement δ , the σ_b , the σ_p at t_0 are reported. The evaluations are made on 12 points at t_0 , at x distance from the extreme vertex. The box cell colour cyan is for the transfer lengths, orange for the unbonded parts and blue is for the bonded portions.

Table 47 - Control parameters for UMI12 at t_0

1 st step → no vertical load				
Sections ID	x [mm]	δ [mm]	σ_b [MPa]	σ_p [MPa]
S ₁	0	-2.02	-1.08	1112.62
S ₂	250	-1.20	-21.06	1044.59
S ₃	500	-0.61	-30.78	997.37
S ₄	750	-0.14	-27.21	1014.49
S ₅ - pin	850	0.00	-9.21	1022.66
S ₆	1000	0.28	-24.23	1022.81
S ₇	1250	0.66	-23.21	1022.82
S ₈	1575	1.11	-23.22	1022.83
S ₉	2300	1.86	-24.43	1022.85
S ₉	2300	1.86	-25.11	1006.85
S ₁₀	2800	2.17	-23.08	1022.82
S ₁₁	3300	2.32	-23.27	1022.34
S ₁₂ - midspan	3500	2.33	-23.28	1022.21

In Table 48, the δ , σ_b , σ_p at t_f (166th step load) are reported which correspond to the maximum load of 467 kN.

Table 48 - Control parameters for UMI12 at t_f

166 th step → no vertical load				
Sections ID	x [mm]	δ [mm]	σ_b [MPa]	σ_p [MPa]
S ₁	0	0.29	-1.08	1112.62
S ₂	250	0.36	-20.93	1044.94
S ₃	500	0.27	-30.16	998.59
S ₄	750	0.08	-29.36	1010.41
S ₅ - pin	850	0.00	-8.87	1061.09
S ₆	1000	-0.25	-23.64	1061.03
S ₇	1250	-0.64	-17.53	1061.35
S ₈	1575	-1.16	-13.22	1061.30
S ₉	2300	-2.32	-3.66	1061.18
S ₉	2300	-2.32	-3.79	1094.09
S ₁₀	2800	-3.06	3.54	1125.99
S ₁₁	3300	-3.48	3.47	1178.35
S ₁₂ - midspan	3500	-3.52	3.48	1193.26

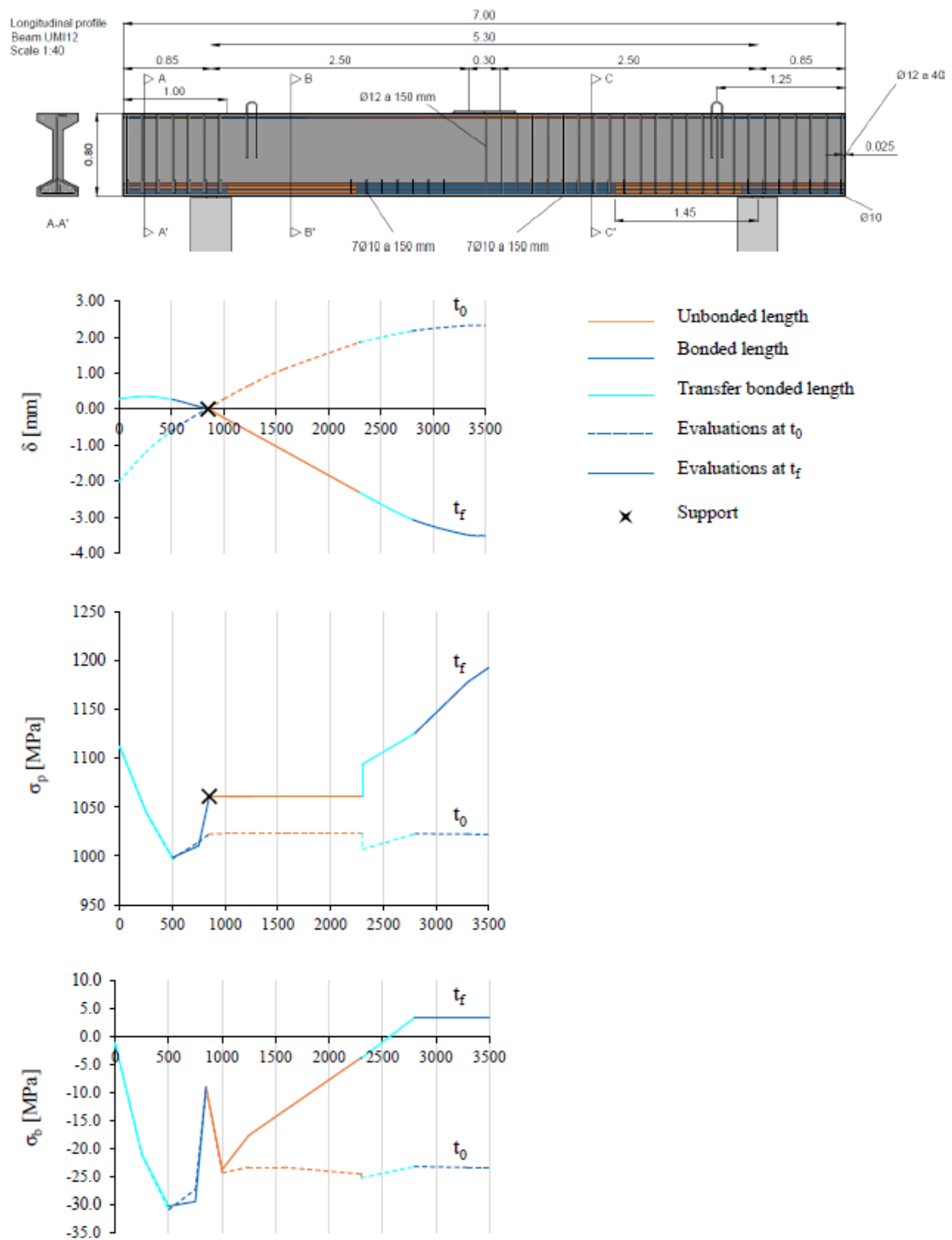


Fig. 75 - δ , σ_p , σ_b at t_0 and t_f for UMI12

In Fig. 75, the δ , σ_p , σ_b are plotted on the half beam length. The δ defines a convex curvilinear deformed at t_0 , induced by the negative constant moment acting on the beams.

While, at t_f the deformed is a concave curve due to the positive moment induced by the vertical load.

At the moment of prestressing, the σ_p increases in the extreme transfer length and remains constant in the unbonded branch on 1022 MPa. Subsequently, a discontinuity is observed at 2300 mm which corresponds to the start point of the middle transfer length which connects the unbonded part in the shear span and the bonded one in the midspan. Furthermore, to overcome the middle transfer length the σ_p resumed the previous value. At the t_f , the trend is the same unless for the values assumed for the extreme transfer length and the unbonded portion. Indeed, the middle part is characterized by a positive slope due to the bonded condition which transmits the bending stresses to the cable.

The σ_b trend increases in the transfer length with a discontinuity in the support area caused by the restraint of horizontal displacement imposed by the pin. Furthermore, it maintains a constant value of 23.20 MPa with a small discontinuity where the middle transfer length starts. Considering the value at t_f , the σ_b maintains the same trend in the extreme transfer length while it has a positive slope up to 2800 mm, followed by a constant branch. It must be noticed that, compared to the BMI12, the presence of unbonded cable does not affect the concrete stresses.

Fig. 76 -represents the crack damage patter at peak load. The plot shows small flexural and diagonal cracks. Moreover, the failure can be induced by shear actions as they are more extended. The prediction reflects what was expected since the beam is designed to fail due to shear in order to analyse its final shear capacity.

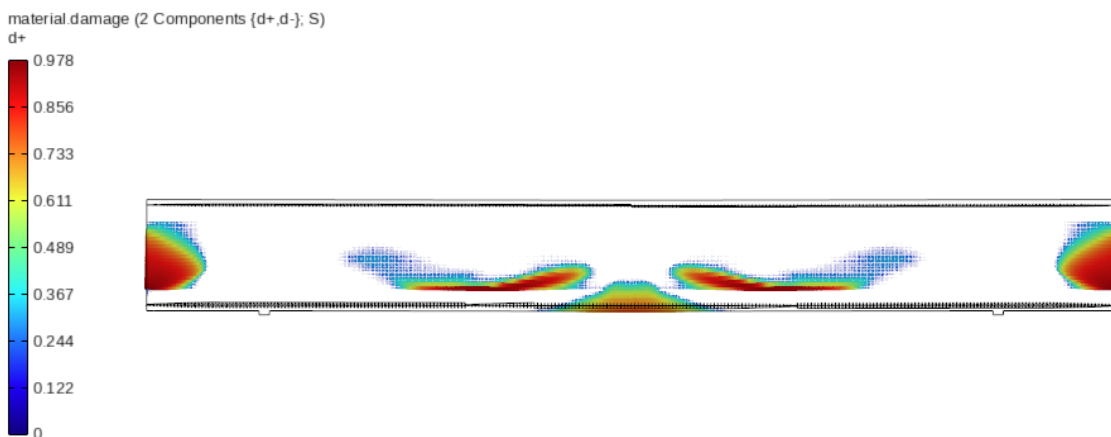


Fig. 76 - Crack damage pattern of UMI12 at t_f

5.FEA: prediction of experimental results with *JCONC*

5.1 Case study 3: UPM and Acciona S.A. beams

5.1.1 FEM modelling strategies

The FEM modelling strategies are the same used for the case studies 1 and 2 and extensively explained in § 3.1.1 and in § 3.2.1. Moreover, the following part reports the differences from the previous models in terms of geometry definitions and material properties. The experimentation data to which it refers are reported in § 4.1.

5.1.1.1 Geometry

The beam body is created by a *Java* code as the previous case studies. Moreover, the presence of the unbonded cable requires the different determination of cable geometry. In particular, the bonded strand parts are defined between several consecutive nodes which belong to the concrete matrix. Furthermore, the unbonded cable portion is defined by its two extreme nodes which belong also to the concrete and the inside portion is totally disconnected from the beam body. In this way, the unbonded condition is simulated. The geometry is reported in Fig. 77.

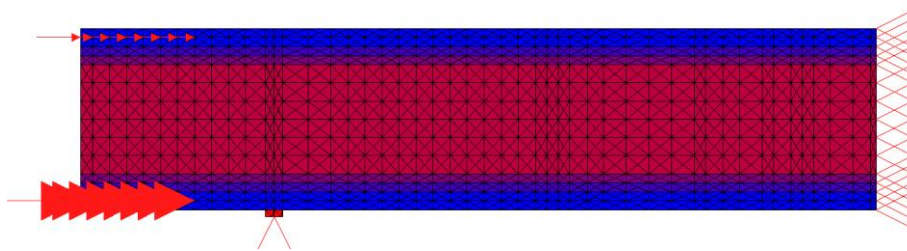


Fig. 77 - *JCONC* geometry of UMI12

5.1.1.2 Material properties

- Concrete

In Table 49, the η , f_{cp} and the E values are reported.

Table 49 - Compressive input data for UPM's beam in JCONC

Concrete type	η [-]	f_{cp} [MPa]	E [MPa]
HPFRC	0.63	76	46250

In Table 50, the f_t is reported for the UPM's beams.

Table 50 - Tensile input data for UPM's beams in JCONC

Concrete type	f_t [MPa]
HPFRC	5.33

- Pre-stressed steel

In Table 51, the $f_{s,r}$ and E are reported for the tendon.

Table 51 - Steel input data for UPM's beams in JCONC

Steel type	$f_{s,r}$ [MPa]	E [MPa]
Y 1860 S7	744	195000

5.1.2 Results and discussion

JCONC allows the evaluation of the stress and strain state at the ultimate load which corresponds to the analysis divergence. Furthermore, the uplift displacement is obtained by setting a negligible vertical load which does not influence the analysis. Hence, in the following section, the uplift δ_0 , the concrete stress at bottom fiber, σ_b , at t_0 and the ultimate shear strength $V_{u,JCONC}$ are reported.

5.1.2.1 BMI12

In Table 52, the δ_0 , σ_b , σ_p and $V_{u,JCONC}$:

Table 52 - JCONC control parameters for BMI12

x [mm]	δ_0 [mm]	σ_b [MPa]	σ_p [MPa]	$V_{u,JCONC}$ [kN]
3500	2.28	14.8	1023.3	810

The shear strength predicted is a very high value. Nevertheless, in Fig. 78, the damage pattern shows diagonal cracks which cause the failure. Hence, the program predicts a

reliable failure as it plots a traditional shear damage pattern but also provides a not reasonable ultimate shear strength.

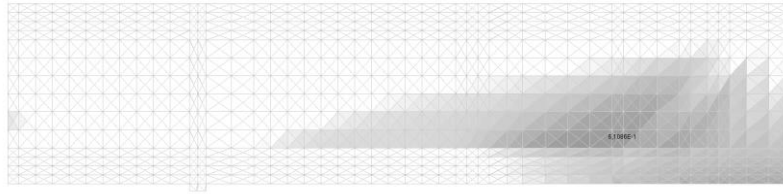


Fig. 78 - JCONC crack pattern for BMI12

5.1.2.2 UMI12

In Table 53, the δ_0 , σ_b , σ_p and $V_{u, JCONC}$:

Table 53 - JCONC control parameters for UMI12

x [mm]	δ_0 [mm]	σ_b [MPa]	σ_p [MPa]	$V_{u, JCONC}$ [kN]
3500	2.30	14.6	1024	734

The shear strength predicted is a very high value. Indeed, the failure is caused by the reaching of yielding strength since a cable element reaches the 744 MPa. Hence, the failure predicted by the software is not what was expected as the beam is designed to fail due to shear. Furthermore, a heavy shear damage is presented in Fig. 79.

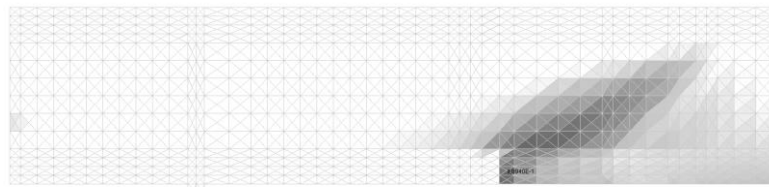


Fig. 79 - JCONC crack pattern for UMI12

6. Comparison between Experimental results, *STKO Opensees* and *JCONC* predictions

The following section details the comparison between numerical predictions and analytical evaluations against the test results for Case Study 1 and 2. The Case study 3 presents only the comparison between numerical and analytical results. The further considerations are principally made on the comparison between the ultimate shear capacity provided by numerical, analytical and the test estimations since the research aim is providing reliable prediction of UPM ultimate shear strength. Despite this, the crack damage plot correlation is realized.

The numerical prediction considers the analysis of *STKO Opensees* and *JCONC*. Moreover, the analytical evaluations of shear capacity consider the two formulations proposed by MC2010 [1] and the EC2 [44] for FRC elements without transversal reinforcement. The first assumes that as the fibers provide a distributed reinforcement, the shear contribution of fibers is modelled as a modifier of longitudinal displacement ratio. The factor takes into account the toughness properties of FRC as in the (29). It is proposed by Minelli et al.:

$$V_{Rd,F} = \left\{ \frac{0.18}{\gamma_c} \cdot k \left[100 \cdot \rho_l \left(1 + 7.5 \cdot \frac{f_{Ftuk}}{f_{ctk}} \right) \cdot f_{ck} \right]^{\frac{1}{3}} + 0.15 \sigma_{CP} \right\} \cdot b_w \cdot d \quad (29)$$

where:

- γ_c : is the concrete safety factor;
- k : is equal to $1 + \left(\frac{200}{d}\right)^{0.5}$ and it take into account the size effect;
- ρ_l : is the longitudinal reinforcement ratio (limited to 2%);
- f_{Ftuk} : is the characteristic values of the ultimate residual tensile strength for FRC, considering the rigid-plastic approach;
- f_{ctk} : is the characteristic concrete tensile strength;
- f_{ck} : is the characteristic concrete compressive strength;
- σ_{CP} : is the average axial stress on the cross section induced by prestressing;

- b_w : is the web thickness;
- d : is the effective depth.

Awareness of the medium value of characteristic properties allows the writer to use them instead of the characteristic value and the γ_c equal to 1.

The new EC2 draft proposes another formulation which considers the relation between the aggregate size and the effective depth (31). For the prestressed element the term 0.15 σ_{CP} is added to $\tau_{Rd,cf}$.

$$V_{Rd} = \tau_{Rd,cf} \cdot b_w \cdot z \quad (30)$$

$$\tau_{Rd,cf} = \eta \cdot \frac{0.6}{\gamma_c} \left(100 \cdot \rho_l \cdot f_{ck} \cdot \frac{d_{dg}}{d} \right)^{1/3} + f_{Ftud} \geq \eta \cdot \tau_{Rdc,min} + f_{Ftud} \quad (31)$$

$$f_{Ftud} = f_{Ftuk} / \gamma_F \quad (32)$$

$$\eta = \max \left(\frac{1}{1 + 0.43 f_{Ftuk}^{2.85}}; 0.4 \right) \quad (33)$$

$$d_{dg} = \begin{cases} 16 + D_{lower} \leq 40 [mm] & \text{if } f_{ck} \leq 60 MPa \\ 16 + D_{lower} \left(\frac{60}{f_{ck}} \right)^2 \leq 40 [mm] & \text{if } f_{ck} \geq 60 MPa \end{cases} \quad (34)$$

$$\tau_{Rd,min} = \frac{11}{\gamma_V} \cdot \sqrt{\frac{f_{ck} \cdot d_{dg}}{f_{yd} \cdot d}} \quad (35)$$

where:

- γ_F : is the partial factor for actions, also accounting for model uncertainties and dimensional variations;
- D_{lower} : is the smallest value of the upper sieve size D in an aggregate for the coarsest fraction of aggregates in the concrete permitted by the specification of concrete;
- γ_V : is the partial factor for shear and punching resistance without shear reinforcement;
- f_{yd} : is the design yield strength of reinforcement;
- z : is the mechanical arm.

6.1 Case study 1: Minelli's experimentations

In Table 54, the shear capacity for MC2010 formula ($V_{u,MC10}$) and for the EC2 draft one ($V_{u,EC2-draft}$), are reported. As far as the numerical predictions are concerned, the ultimate shear strength is reported from the *STKO OpenSees* analysis ($V_{u,STKO}$) and the *JCONC* one ($V_{u,JCONC}$). Table 54 also presents the comparison with the test results.

Table 54 - Comparison between MC10, EC2-draft, STKO Openses and JCONC results for Minelli's beams

Minelli's beams	H500 FRC50	H1000 FRC50	H1500 FRC50	H500 FRC75	H1000 FRC75	H1500 FRC75
$V_{u, test}$ [MPa]	236	264	472	231	343	542
$V_{u, MC10}$ [MPa]	201	369	520	212	389	547
$V_{u, EC2-draft}$ [MPa]	194	400	601	228	472	712
$V_{u, STKO}$ [MPa]	221	409	552	223	412	581
$V_{u, JCONC}$ [MPa]	231	392	560	238	409	570
$V_{u, MC10}/V_{u, test}$	0.85	1.40	1.10	0.92	1.13	1.01
$V_{u, EC2-draft}/V_{u, test}$	0.82	1.51	1.28	0.99	1.38	1.32
$V_{u, STKO}/V_{u, test}$	0.93	1.55	1.17	0.97	1.20	1.07
$V_{u, JCONC}/V_{u, test}$	0.98	1.48	1.19	1.03	1.19	1.05

The results of the four analyses show a good prediction of ultimate shear capacity for the shallowest beams H500FRC50 and H500FRC75 as the error is within the $\pm 15\%$ range. The H1000FRC50 represents an outlier as the error exceeds $+40\%$ in all the four evaluations. Moreover, the author already reports the H1000FRC50 is out of the trend which considers the ratio between the experimental results and the MC2010 estimations. Hence, H1000FRC50 is not considered in the final evaluations. Furthermore, for the H1000FRC75, H1500FRC50 and H1000FRC75 the provided values are in good agreement with the experimental results as the error is around $\pm 20\%$ unless for the EC2-draft estimations which is out of the previous range.

Table 55 - Statistical evaluation on result's comparison for Minelli's beams

μ_{MC10}	1.00
SD_{MC10}	5.72%
$\mu_{EC2-draft}$	1.15
$SD_{EC2-draft}$	22.93%
μ_{STKO}	1.07
SD_{STKO}	5.65%
μ_{JCONC}	1.09
SD_{JCONC}	3.73%

In Table 55, the μ and SD stay for mean value and standard deviation. The μ_{MC10} is equal to zero with a dispersion up to 6%. Thus, the proposed formula of Minelli (29) has a high reliability in the shear behaviour prediction of beams without transverse reinforcement. Indeed, the second formula (31) proposed by EC2 provides worse results since the mean error value of 15% and a high dispersion of 23%. Even though an error of 15% may be accepted, the analytical estimations should be lower than the real on the safety side. As far as the numerical predictions are concerned, both *STKO Opensees* and *JCONC* provide good estimations since the mean error is up to 7% and 9% and the SD is less than 6%.

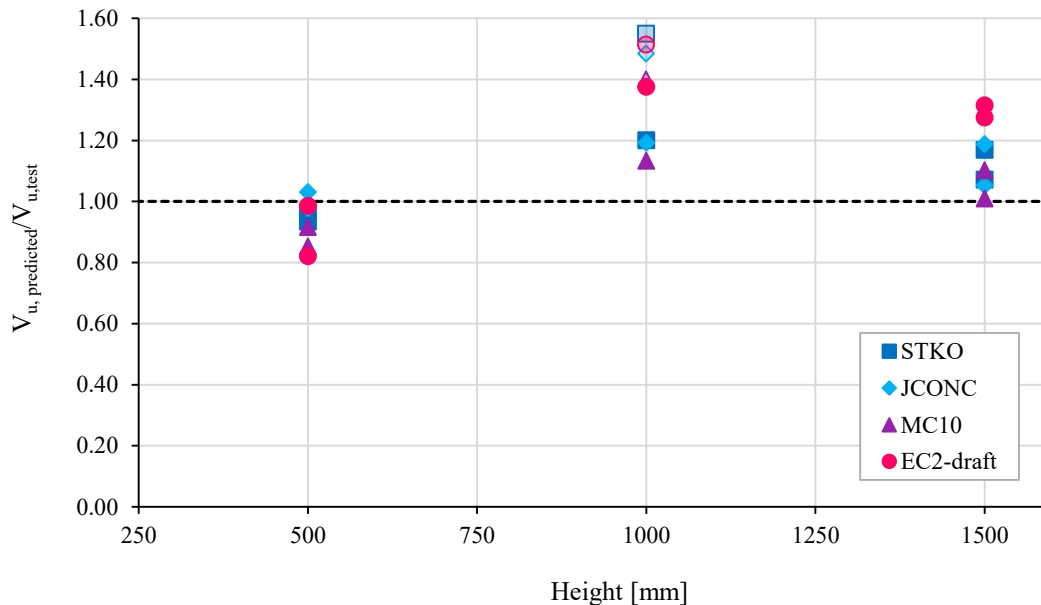


Fig. 80 - Ratio overview of results' comparison for Minelli's beams

Fig. 80 proposes a graphical overview of the ratio between analytical and numerical evaluation against the test results. The chart also reports in transparency the values for H1000FRC50 which are not taken into account in the results presented in Table 55.

The chart clearly shows that results of *JCONC* and *STKO Opensees*© present close ratios since their dots are almost in the same positions. On the contrary, the previous consideration is not true for the analytical evaluations.

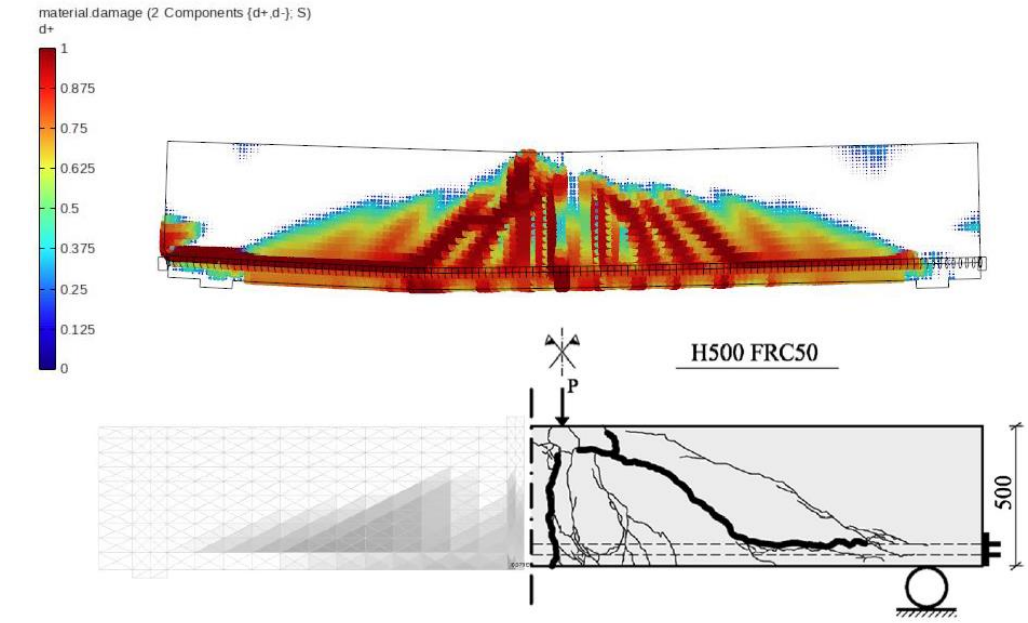


Fig. 81 - Numerical and experimental damage pattern comparison for H500FRC50

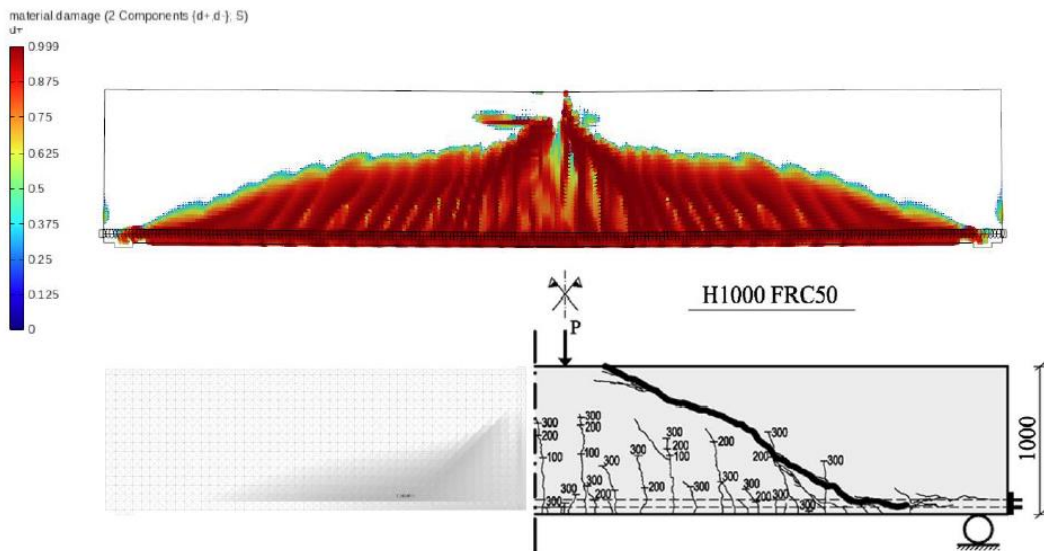


Fig. 82 - Numerical and experimental damage pattern comparison for H1000FRC50

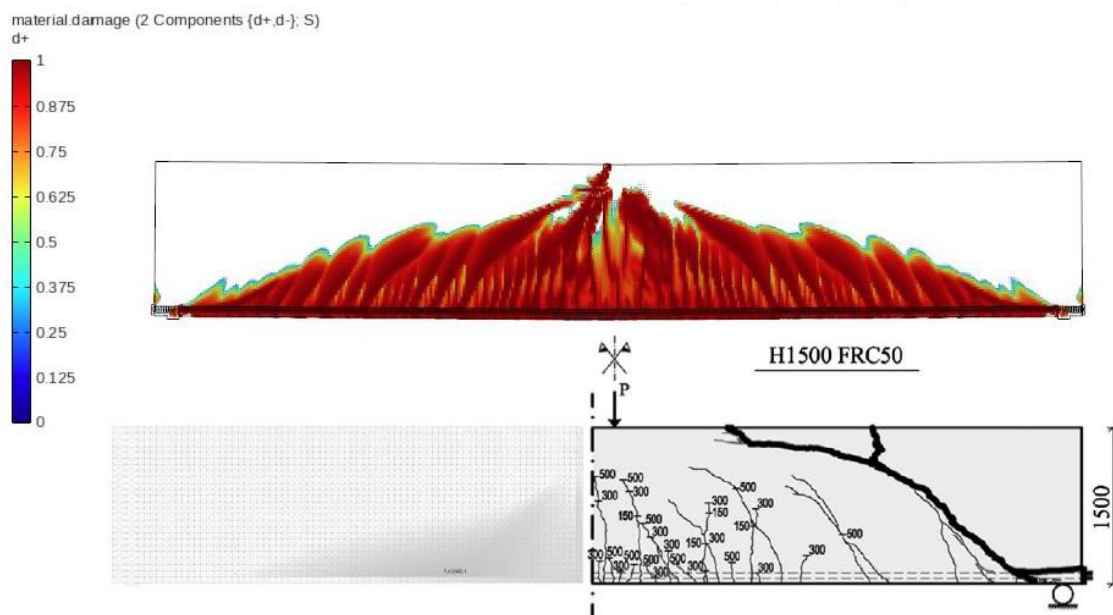


Fig. 83 - Numerical and experimental damage crack comparison for H1500FRC50

Finally, Fig. 81, Fig. 82 and Fig. 83 show the comparison between cracks patterns. The numerical, developed by the two FEM programs, and experimental patterns are comparable as the principal diagonal cracks are located in the same position for H500FRC50. Furthermore, they presented some differences from the experimental damage plot for H1000FRC50 and H1500FRC50. In particular, in the final test configuration the failure cracks are more inclined and in a different position. Despite the differences, both softwares are capable of predicting the failure as all the beams fail by the same causes explained in the experimental report.

6.2 Case study 2: Cuenca's experimentations

Table 56 - Comparison between MC10, EC2-draft, STKO Opensees and JCONC results for Cuenca's beams

Cuenca's beams	HF600/5	HF400/7	HF400h/6	HF260/9
$V_{u, test}$ [MPa]	348	390	420	326
$V_{u, MC10}$ [MPa]	180	176	182	198
$V_{u, EC2-draft}$ [MPa]	219	212	242	239
$V_{u, STKO}$ [MPa]	353	353	337	287
$V_{u, JCONC}$ [MPa]	535	502	580	515
$V_{u, MC10}/V_{u, test}$	0.52	0.45	0.43	0.61
$V_{u, EC2-draft}/V_{u, test}$	0.63	0.54	0.58	0.73
$V_{u, STKO}/V_{u, test}$	1.01	0.91	0.80	0.88
$V_{u, JCONC}/V_{u, test}$	1.54	1.29	1.38	1.58

In Table 56, the MC10, EC2-draft, *STKO OpenSees* and *JCONC* results are presented. The analytical estimations provide low shear capacity compared to the test results for all the four beams. In particular, the highest error is around -32% for both MC10 and EC2-drafts. Hence, considering the analytical evaluation, the shear strength is heavily underestimated. Furthermore, the *STKO* predictions result to be in good agreement with the test behaviour as the final maximum error is $\pm 20\%$. On the contrary, *JCONC* strongly overestimates the ultimate shear capacity as the error is up to +58%. As explained in § 3.2.2, *JCONC* assumes an elasto-plastic behaviour for concrete which in reality is a quasi-brittle material. Hence, due to the high value of compressive strength, the model is not able to detect the damage and the capacity losses induced by the cracking. The solutions could be more attached to the reality if the model is provided by transversal reinforcement since the final behaviour of the reinforced concrete is closer to the elasto-plastic one.

Table 57 - Statistical evaluation on result's comparison for Cuenca's beams

μ_{MC10}	0.50
SD_{MC10}	1.89%
$\mu_{EC2-draft}$	0.62
$SD_{EC2-draft}$	2.09%
μ_{STKO}	0.90
SD_{STKO}	2.32%
μ_{JCONC}	1.45
SD_{JCONC}	5.61%

Table 57 reports a statistical overview of the final comparison between the different evaluations. The μ and SD of analytical estimations confirms that the analytical formulations provide an underestimation of 50% for MC10 and 37% for the EC2-draft. Moreover, the numerical *STKO OpenSees* results have a mean error of 10% and a low dispersion of values. In contrast, *JCONC* presents a general overestimation of 45% and, finally, it is not able to provide valuable results for HPFRC prestressed beams.

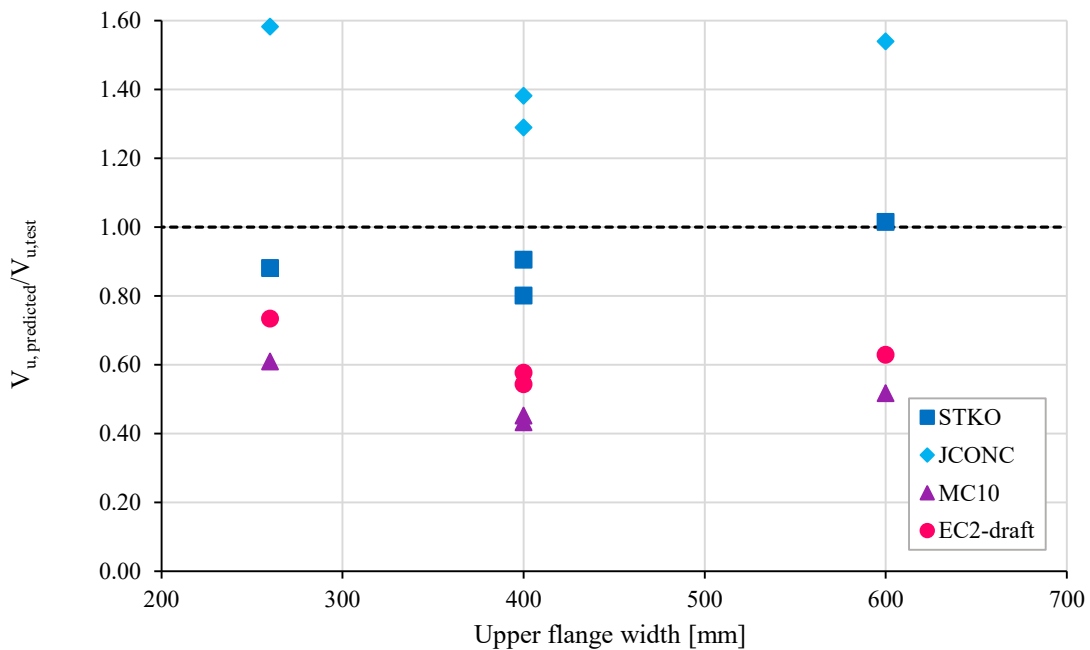


Fig. 84 - Ratio overview of results' comparison for Cuenca's beams

The Fig. 84 shows a graphical overview of the final comparison. The chart clearly demonstrates that the closest predictions are made by *STKO* analysis. Moreover, the *STKO OpenSees*, *MC10* and *EC2-draft* provide lower results with respect to the real values, while *JCONC* is given higher values, being out from the safe side.

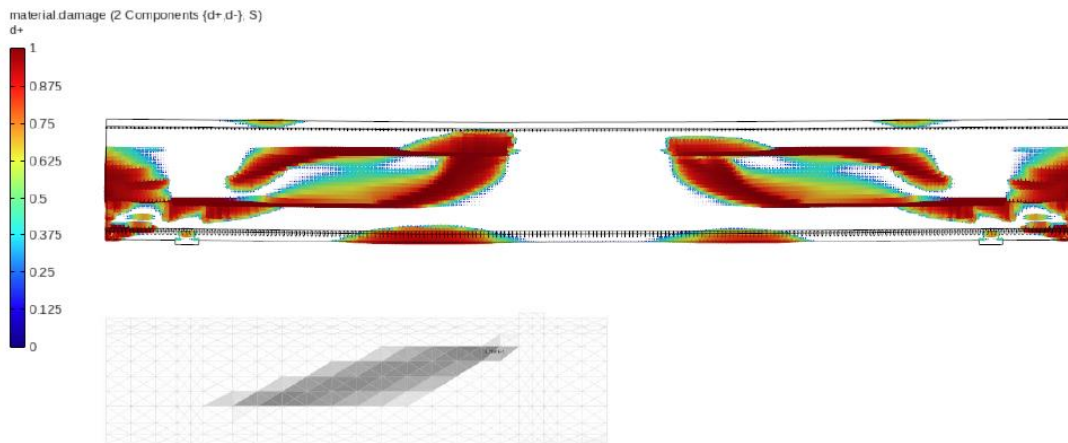


Fig. 85 - Numerical and experimental damage crack pattern comparison for HF600/5

In Fig. 85, the numerical crack damage comparisons are presented. Despite providing wrong estimation of ultimate shear strength, *JCONC* defines a shear failure attached to the real one and located in the same position of *STKO OpenSees*© plot. Consequently,

even though *JCONC* is not capable of correctly detecting the ultimate shear strength, it develops a right failure.

6.3 Case study 3: UPM and Acciona S.A. beams

The *STKO OpenSees* and *JCONC* σ_p at t_0 are compared in order to detect the equivalence between the prestressing actions simulated by FEM analyses.

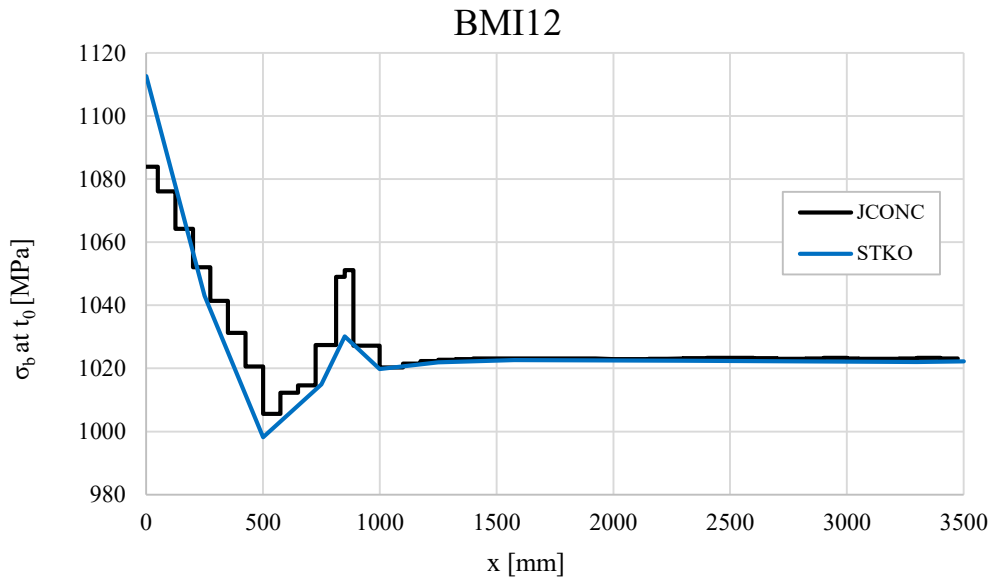


Fig. 86 - STKO and JCONC σ_p comparison for BMI12

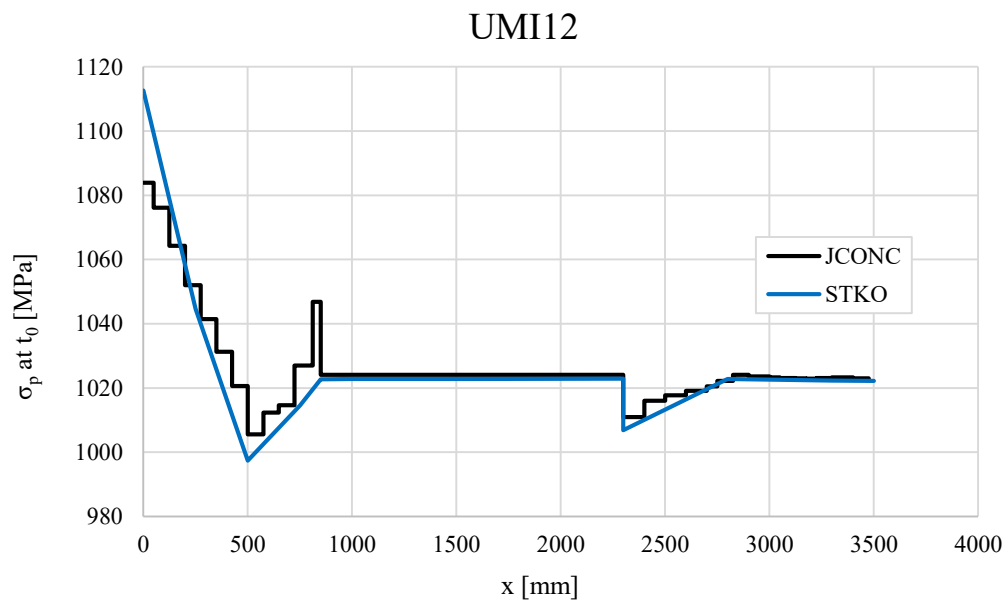


Fig. 87 - STKO and JCONC σ_p comparison for UMI12

The two numerical models are in good agreement as the trends is approximately the same both for BMI12 and UMI12, as Fig. 86 and Fig. 87. Hence, the numerical results are comparable since the prestressing action develops the same effects.

The numerical predictions for Case study 3 are compared against the MC10 and EC2-draft estimations since the test results are not available.

Table 58 - MC10, EC2-Draft, STKO and JCONC results for UPM's beams

Cuenca's beams	BMI12	UMI12
$V_{u, MC10}$ [MPa]	303	303
$V_{u, EC2-draft}$ [MPa]	517	517
$V_{u, STKO}$ [MPa]	475	467
$V_{u, JCONC}$ [MPa]	810	734

In Table 58, the MC10 formulation provides low shear strength compared to numerical predictions of *STKO OpenSees* and *JCONC*. On the contrary, the EC2-draft gives higher results with respect to numerical simulations. Moreover, considering the numerical predictions, the most promising may be the STKO one since they detect a reasonable value of ultimate shear capacity. The previous consideration is based on the similarity with the Cuenca's beams in terms of geometry and prestressing.

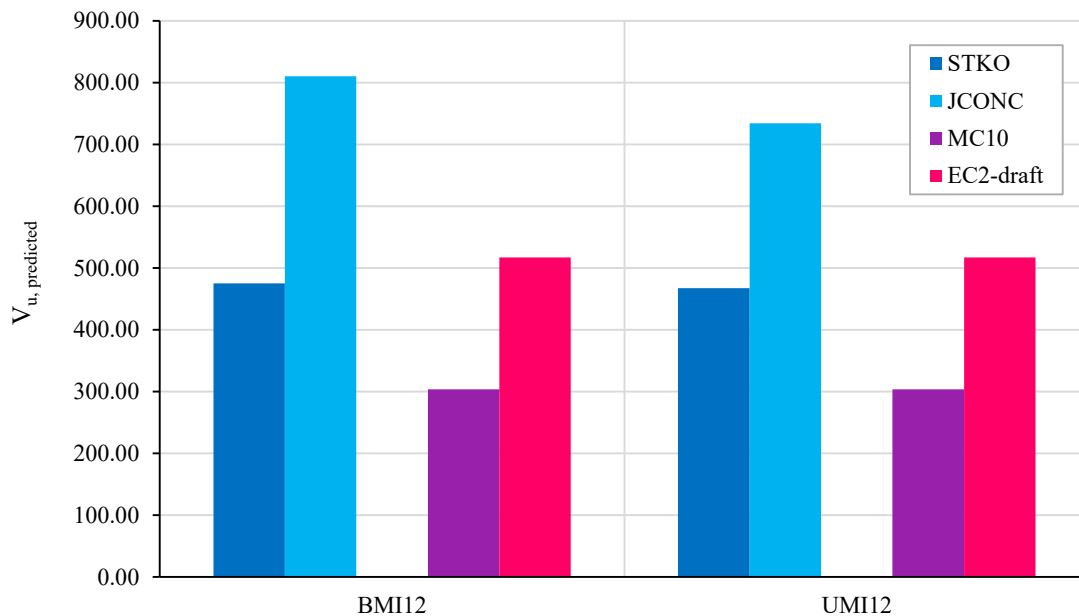


Fig. 88 - Overview of UPM's beam final shear strength

Fig. 88 presents a graphical comparison between the four estimations. The chart clearly shows the *JCONC* out of trend prediction compared to the other estimations. Furthermore, values remain in a reasonable range compared to the previous case study.

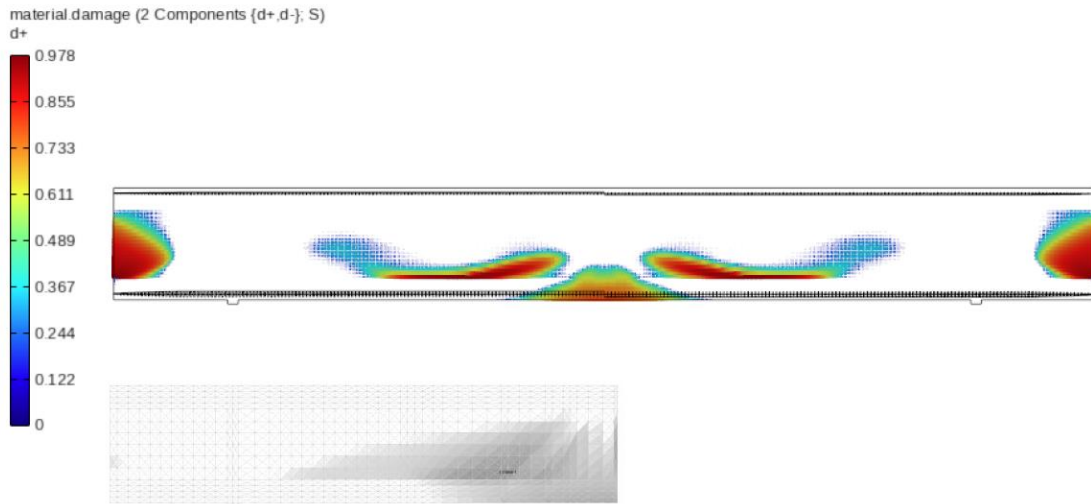


Fig. 89 - Numerical and experimental damage crack pattern comparison for BMI12

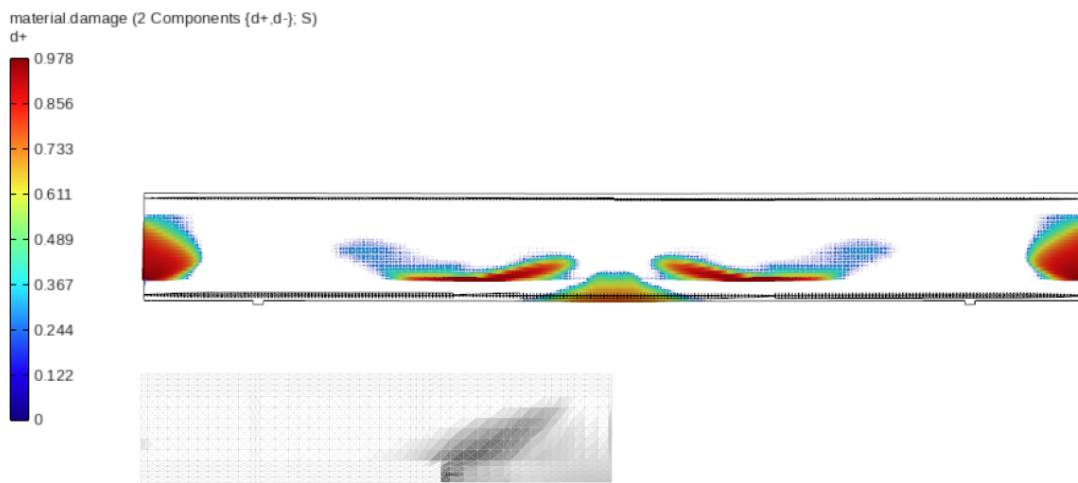


Fig. 90 - Numerical and experimental damage crack pattern comparison for UMI12

Finally, Fig. 89 and Fig. 90 compare the *STKO Opensees*© crack damage against the *JCONC* plot. The *STKO* presents a shear failure for both beams while *JCONC* provides a flexural failure for BMI12 and a shear one for UMI12. Nonetheless, the damage developed by both the programs localize the diagonal and vertical cracks in the same positions.

7. Conclusions

This thesis has dealt with the numerical simulation of FRC, HPFRC and prestressed HPFRC mechanical behaviour during experimental tests of critical shear beams.

Firstly, a literature review has been carried out in order to understand the physics of the problem and the main variables that significantly affect mechanical behaviour. The parameters that result to be decisive for the determination of FRC and HPFRC elements capacity are the structural geometry, with particular attention for a/d ratio, and the fiber quantitative, represented by V_f . Considering the FRC shear capacity which is the focus of this research work, the works of Meda et al. [28] demonstrated that beams reinforced with the minimum fibers content had a similar or better post cracking behaviour respect to the ones with the minimum transverse reinforcement. Furthermore, considering the study realized by J. A. Torres et al. [29], fiber content higher than 1.2% changes the failure mode from shear to shear-flexural cracks.

Furthermore, the state of the art of experimentations provided by Minelli et al. [30] has been analysed. The modelling has required careful evaluations of the load-displacement curve and the damage crack patterns in order to understand the physics of the failure. Afterwards, the *STKO Opensees*© has been chosen to reproduce experimental behaviour. A good representation of numerical results hunts for a setting process which must be provided by the knowledge of the damage model implied by the software. In particular, this is crucial in the simulation of shear failure since it is caused by the development of diagonal crack patterns due to the achievement of ultimate tensile concrete stress.

In order to evaluate the input setting and provide the basis for the FRC beams modelling, firstly numerical reproductions of experimental reinforced normal concrete results have been performed. The first objective has been obtaining an acceptable match between numerical and experimental load - displacement curve. Furthermore, as the curve provides different development of stiffness losses, the investigation of numerical crack pattern evolution has been realized in order to detect if the software develops a physical explainable behaviour. The reason for differences stays in the damage evolution. In particular, at the cracking first stage, the damage model develops horizontal diffuse cracks

instead of deep vertical ones. Hence, the heavy stiffness losses induced by flexural stresses are delayed.

The worst estimations have regarded the P_{cr} and the displacement as the general error is over 40% for the first parameters and 22% for the second. Nonetheless, the reliability of numerical predictions has been proved taking into account some control parameters such as the load at crack stage P_{cr} , the ultimate load P_u , the ultimate displacement δ and the slope of the linear and nonlinear branch, S_1 and S_2 . The evaluations have proved a good agreement with the experimental prediction as the mean value of the ratio between STKO predictions and experimental results is equal to 1.02 with a low dispersion of value equal to 1.37% for P_u , S_1 and S_2 . The previous consideration confirms the reliability of results even though the experimental curve is not completely attached to the numerical one, following a different crack development. Subsequently, the applied strategy has been implied for the FRC beams. The results have confirmed the previous trend for P_u , S_1 and S_2 with a mean error of 0.06% and a low dispersion of 5%. Moreover, the FRC numerical curves are more attached to the experimental ones as well as for the crack damage patterns. Furthermore, it has been proved that the G_t has been affected by scale effect and the correct evaluation requires a parametrization which can improve the numerical attachment to reality. However, the models are able to represent the test results especially for FRC elements which are the main aim of the research work.

The following step provides the numerical simulation for a different experimental campaign carried out by Estefania Cuenca [41]. The models approached a new typology of beams as they presented the HPFRC with bonded prestressing. The predictions have provided results even attached to the test result with a P_u mean error of 10% and a dispersion of 2.32%. Indeed, the crack patterns show clearly a shear failure comparable to what described by the authors. Therefore, the models also present reasonable results against the manual checking performed to verify if the prestressing actions induced effects physically explainable.

STKO OpeenSees© is an advanced software whose calibration requires the input of several parameters that can be affected by measuring uncertainties or physical phenomena such as size effect. The application in practitioner everyday work can require an advanced knowledge of FEA and it is time consuming for the calibration of the models. The

previous considerations have suggested adopting another software, *JCONC*, which assumes an *EPSF* approach and few input data which are easy to collect and with low uncertainties. Furthermore, the formulation proposed by MC2010 [1] and EC2 Draft [44] have been tested to prove the capability of providing good estimation of shear capacity for FRC elements.

The comparison between numerical, analytical and experimental values have exhibited the same order of magnitude for the first case study. Furthermore, for the second case study, both the analytical formulations have provided a mean underestimation of 23% while the *JCONC* predictions overestimate the results of 45%. The most attached prediction has been given by *STKO OpenSees*© with a mean error of -10% a dispersion of 2.32%. Thus, *JCONC* has proved the inability to provide good estimates for HPFRC due to the strong assumption on the elasto-plastic constitutive laws of the material.

Afterwards, the analysis of the previous results, the prediction of experimental behaviour of UPM beams has been modelled. Due to the complexity of beams' tendons design, a stage of detailed analysis of stresses induced by the prestressing actions has been fulfilled for *STKO OpenSees*© which has presented the expected results. Furthermore, as far as the ultimate load and the damage evolutions is concerned, the comparison between analytical evaluation and numerical prediction shows the same order of magnitude for *STKO OpenSees*© predictions while *JCONC* results are out of the trend.

The adoption of an advanced software as *STKO OpenSees*© requires deep knowledge of the physics of the problems. Indeed, the representation of the experiment is hunting for the perfect reproduction of the test setup, which is not always reported in the scientific literature. The consequence is that the user must be able to detect if the geometry or numerical instabilities affect the results. Therefore, the approach of an easy software such as *JCONC* could be useful in the further predictions of normal strength materials as provided with Case study 1. Furthermore, the strong basic assumption on material stress-strain relationship should be carefully evaluated for high strength materials such as HPFRC which are affected by a different toughness since it can provide wrong previsions as proved for Case study 2 and 3. Hence, the analysis of advanced material sometimes requires the users to deal with complex nonlinear FEA.

Therefore, making blind predictions is a really ambitious goal to achieve since the complexity of nonlinear behaviour is affected by several model uncertainties and physical phenomena which the FEM software are not always able to reproduce. Furthermore, the models of the state of the art case studies realized have shown the FEM capability of giving approximate solutions of the ultimate shear capacity, taking into account the available data even though the load-displacement curve presents non negligible differences. Indeed, the final aim of the research has been pursued as the main objective was providing a reliable method to help professionals to understand the physics behaviour and the final capacity of the elements, laying the foundations for the practice applications. However, the work remarks that nonlinear finite element analysis are only numerical predictions and not the reality of physical behaviour. This assumption must guide practitioners' criteria in a preliminary design phase to avoid rough mistakes in the final project.

8. Future developments

The research work presented in this document can find future development in both numerical and experimental fields.

The numerical reproduction of experimental results for case study 1 has shown the randomness of some physical input parameters such as the fracture energy (G_f) in tension and the concrete axial tensile strength, f_t . In particular, the evaluation of G_f by standard code formulations does not complain about the overall physical phenomena which affects the parameters. Indeed, the f_t is estimated by empirical formulation due to complications induced by the direct uniaxial tensile test on concrete. The previous consideration suggests the necessity of a structured parametrization on these parameters to better match the experimental curve.

The formulation considered for the evaluation of G_f in this work is based on the MC2010 recommendations. In particular, it bases the evaluation only on the flexural tensile strength for PC and residual strength for FRC. Thus, the parametrization could consider different formulations presented in literature which take into account other mix design characteristics as the maximum aggregate size. Moreover, the *STKO OpenSees*© Python interface could be helpful to provide a model updating, iteratively increasing the chosen parameters. The application of this method could contribute to understanding and quantifying the impact of unknown variabilities on the analysis with the aim to provide a better attachment to the reality. Furthermore, a statistical regression on a bigger data set could be the basis for new more accurate empirical relation to predict the value for tested elements.

Therefore, the parametrization could also involve the numerical setting of FEA. In particular, the parameters that can be changed is the mesh size and the iterations for each step load. In this case, the aim would be checking the stability of the analysis results against the setting choice. The results are of certain importance because they could prove the possible sensitivity of analysis with respect to the users' choice.

Moreover, the final blind predictions are based on simplification of the real tendons layout. An interesting improvement could be a more detailed modelling of them in order to detect its impact on the overall behaviour of the beams.

Finally, the future of this research work is to prove the validity of blind prediction with the experimentation campaign that will take place next month at the Structural Laboratory of UPM. The results provided by the test can confirm the already realized analysis based only on the material characteristics. On the other hand, they will be the basis for the model updating, outlining the final FEM model strategy. In particular, the definition of a promising FEM analysis strategy for HPFRC with unbonded prestressing can help practitioners to perform reliable analysis in everyday practice.

9. Bibliography

- [1] Fédération internationale du béton., Fib model code for concrete structures 2010, Lausanne, Switzerland : Ernst & Sohn, a Wiley brand,, 2013.
- [2] C. M. D. D. Di Prisco M., «Fiber-reinforced concrete in fib Model Code 2010: principles, models and test validation,» *Structural Concrete* , n. 4, 2013.
- [3] ACI 544, «Design Considerations for Steel Fiber Reinforced Concrete,» *ACU Journal Proceedings*, vol. 1, n. 2003 , 2003.
- [4] V. Titiksh, «Evaluating the Performance of Hybrid Fiber Reinforced Self Compacted Concrete (HFRSCC) Using Steel and Banana Fibers,» 2016.
- [5] S. Ribakow, «Recent trends in steel fibered high-strength concrete,» 2011.
- [6] L. B. a. T. O. Vahid Afroughsabet, «High-performance fiber-reinforced concrete: a review».
- [7] L. T. a. H. C. Rafael Ruiz, «Conceptual design of HPFRC and UHPFRC road girder bridges,» Switzerland, 2021.
- [8] C. E. C. f. Standardization, “Eurocode 2: Design of concrete structures - Part 1-1: General rules and rules for buldings., 2013.
- [9] Fédération internationale du béton (fib), Model Code for Concrete Structures 2020 (Draft),, Lausanne, Switzerland, 2020.
- [10] AFNOR P18B, NF P18-710 - National addition to Eurocode 2 - Design of concrete structures: specific rules for Ultra-High Performance Fibre-Reinforced Concrete, France,, 2016.

- [11] SIA 2052, Béton fibré ultra-performanc (BFUP): Matériaux, dimensionnement et exécution, Zurich, Switzerland, 2016.
- [12] American Society for Testing and Materials, ASTM C1856/C1856M Standard Practice for Fabricating and Testing Specimens of Ultra-High Performance Concrete, 2016.
- [13] Japan Society of Civil Engineers (JSCE), Recommendations for Design and Construction of High Performance Fiber Reinforced Cement Composites with Multiple Fine Cracks (HPFRCC), Japan, 2008.
- [14] H. Singh, Steel Fiber Reinforced Concrete Behavior, Modelling and Design, Singapore: Springer Nature Singapore Pte Ltd., 2017.
- [15] I. Lofgren, Fibre-reinforced Concrete for Industrial Construction, Göteborg: Chalmers University of Technology, 2005.
- [16] F. Z. R.S. Olivito, «An experimental study on the tensile strength of steel fiber reinforced concrete,» *Elsevier Ltd*, 2009.
- [17] F. F. J. L. Y. X. Xiuling Wang, «Steel fiber reinforced concrete: A review of its material properties and usage in tunnel lining,» *Structures*, vol. 34, n. pp 1080-1098, pp. 1080-1098, 12 2021.
- [18] L. H. P.-T. F. a. J. S. Ding Y, «Experimental investigation on the mechanical behaviour of the fiber reinforced high-performance concrete tunnel segment,» *Composite structure*, vol. 93, n. 4, p. 1284–1289, 2011.
- [19] L. B. a. T. O. Vahid Afroughsabet, «High-performance fiber-reinforced concrete: a review,» *J Mater Sci*, vol. 51, p. 6517–6551, 2016.

- [20] M. M. P. P. Hillerborg A, « Analysis of crack formation and crack growth in concrete by means of fracture mechanics and finite elements,» *Cement and Concrete Research*, vol. 6, pp. 773-780, 1976.
- [21] J. C. Walraven, « High performance fiber reinforced concrete: progress in knowledge and design codes,» *Materials and Structures*, vol. 42, pp. 1247-1260, 2009.
- [22] D. D. S. G. L. T. C. R. Joost Walraven, «Self-compacting high-performance fiber concrete for foundations: Part 1 -experimental verification and design considerations,» *Structural Concrete*, pp. 1-15, 2021.
- [23] M. I. K. S. M. Wasim Abbass, «Evaluation of mechanical properties of steel fiber reinforced concrete with different strengths of concrete,» *Construction and Building Materials*, vol. 168, pp. 556-569, 2018.
- [24] B. C. E. C. Jong-Han Lee, «Flexural capacity of fiber reinforced concrete with a consideration of concrete strength and fiber content,» *Construction and Building Materials*, vol. 138, pp. 222-231, 2017.
- [25] C. E. C. a. C. G. K. Violetta K. Kytinou, «Analysis of Residual Flexural Stiness of Steel Fiber-Reinforced Concrete Beams with Steel Reinforcement,» *Materials*, vol. 13, n. 12, p. 2698, 2020.
- [26] A. M. a. M. F. Ruiz, «Shear strength of members without Transverse Reinforcement as Function of Critical Shear Crack,» *ACI Structural Journal*, vol. 105, p. 17, 2008.
- [27] P. R. a. P. T., Reinforced Concrete Structures, New York: Wiley-Interscience Publications, 1975.
- [28] F. M. G. P. a. P. R. A. Meda, «Shear behaviour of steel fibre reinforced concrete beams,» *Materials and Structures*, vol. 38, pp. 343-351, 2005.

- [29] J. A. T. a. E. O. Lantsoght, «Influence of Fiber Content on Shear Capacity of Steel Fiber-Reinforced Concrete Beams,» *Fibers*, vol. 7, p. 102, 2019.
- [30] A. C. E. C. G. P. F. Minelli, «Are steel fibres able to mitigate or eliminate size effect in shear?,» *Materials and Structures*, vol. 47, pp. 459-473, 2017.
- [31] D. T. T. L. N.-M. ., A. Y. N. Tung D. Dang, «Shear resistant capacity of steel fibres reinforced concrete deep beams: An experimental investigation and a new prediction model,» *Structures*, vol. 33, pp. 2284-2300, 2021.
- [32] T. N. N. Y. S. J. D. U. J. W. Withit Pansuk, «Shear capacity of high performance fiber reinforced concrete I-beams,» *Construction and building materials*, vol. 157, pp. 182-193, 2017.
- [33] J. M. a. B. Z. P., *Inelastic Analysis of Structures*, Baffins Lane, Chichester: John Wiley & Sons, Ltd, 2002.
- [34] R. T. a. J. Z. O.C. Zienkiewicz, *The Finite Element Method: Its Basis and Fundamentals*, Linacre House, Jordan Hill, Oxford OX2 8DP: Elsevier Butterworth-Heinemann, 2005.
- [35] C. G. Petracca M., *STKO User Manual*, Pescara: Asdea software technology,, 2021.
- [36] L. P. R. R. S. Z. G. C. E. S. Massimo Petraccaa, «Micro-scale continuous and discrete numerical models for nonlinear analysis of masonry shear walls,» *Construction and Building Materialsjournal homepage: www.elsevier.com/locate/conbuildmat*, vol. 149, pp. 296-314, 2017.
- [37] Q. H. X. X. N. X. Zhenpeng Yu, «Experimental study and failure criterion analysis of plain concrete under combined compression-shear stress,» *Construction and Building Materials*, vol. 179, pp. 198-206, 2018.
- [38] M. Altilia, *Criteri di modellazione FEM*, Palermo: Grafill, 2016.

- [39] F. C. M. P. D. A. T. Antonio Maria D'Altri, «rate-dependent isotropic damage model for the seismic,» *Bulletin of Earthquake Engineering*, pp. 1573-1456, 2021.
- [40] A. Carpinteri, «Decrease of apparent tensile and bending strength with specimen size: two different explanations based on fracture mechanics,» *Solid Structure*, vol. 25, n. 4, pp. 407-429, 1989.
- [41] E. Cuenca, *On Shear Behavior of Structural Elements Made of Steel Fiber Reinforced Concrete*, New York : Springer Cham Heidelberg New York Dordrecht London, 2015.
- [42] M. F. R. F. N. F. N. A. Muttoni, «Modelling of Critical Details and Investigation of the In-Plane Shear Transverse Bending Interaction,» Bundesamt für Strassen, Lausanne, 2016.
- [43] Michael H. Scott, «Numerical Integration Options for the Force-Based-Beam-Column Element in OpenSees,» 2011.
- [44] CEN/TC 250, Eurocode 2: Design of concrete structures prEN 1992-1-1:2021-09, 2021.

Annex 1

1.1 Evaluation of control parameters for Minelli's beams

- P_{cr} : first cracking load
- P_u : ultimate load at the peak
- δ : displacement at peak load
- S_1 : linear branch slope
- S_2 : nonlinear branch slope

- *H1000PC*

- Experimental curve:

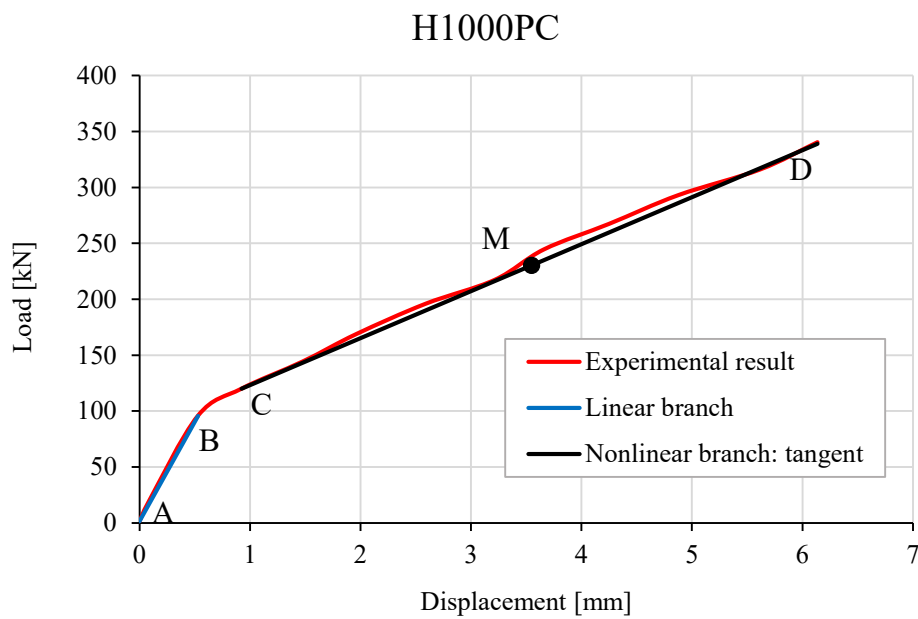


Fig. 91 - Experimental H1000PC load-displacement curve with control parameters

Table 59 - Data input for the evaluation of H1000PC experimental S_1

Points	x	y
Point A	0	1.43
Point B	0.53	95.76
Slope S_1		179

Table 60 - Data input for the evaluation of experimental H1000PC S_2

Points	x	y
Point C	0.92	120.07
Point D	6.14	340.44
Point M	3.55	230.25
Slope S_2		42

- Numerical curve:

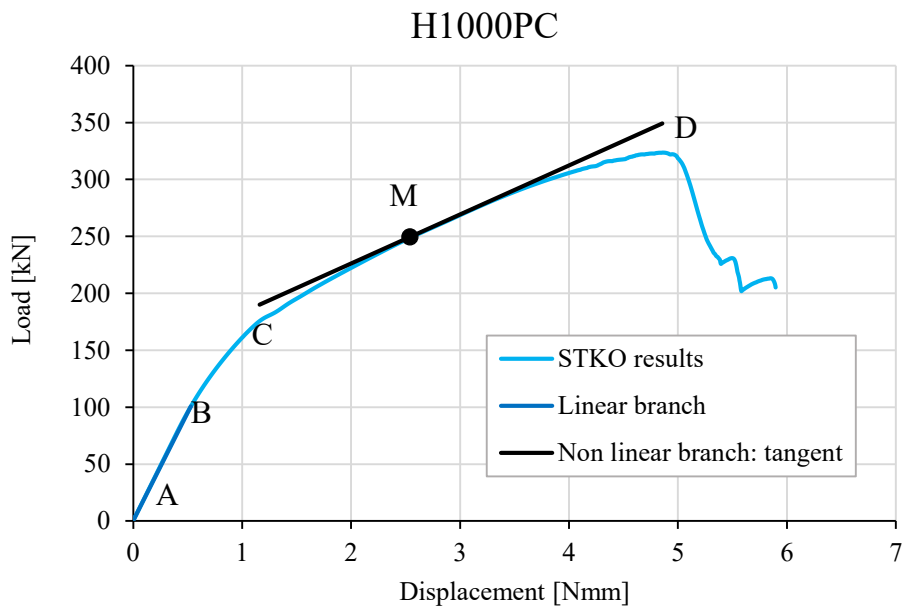


Fig. 92 - Numerical H1000PC load-displacement curve with control parameters

Table 61- Data input for the evaluation of H1000PC numerical S_1

Points	x	y
Point A	0.01	1.93
Point B	0.53	100.55
Slope S_1		190

Table 62 - Data input for the evaluation of H1000PC numerical S_2

Points	x	y
Point C	1.16	175.43
Point D	4.86	323.49
Point M	2.54	249.46
Slope S_2		43

- *H1500PC*

- Experimental curve:

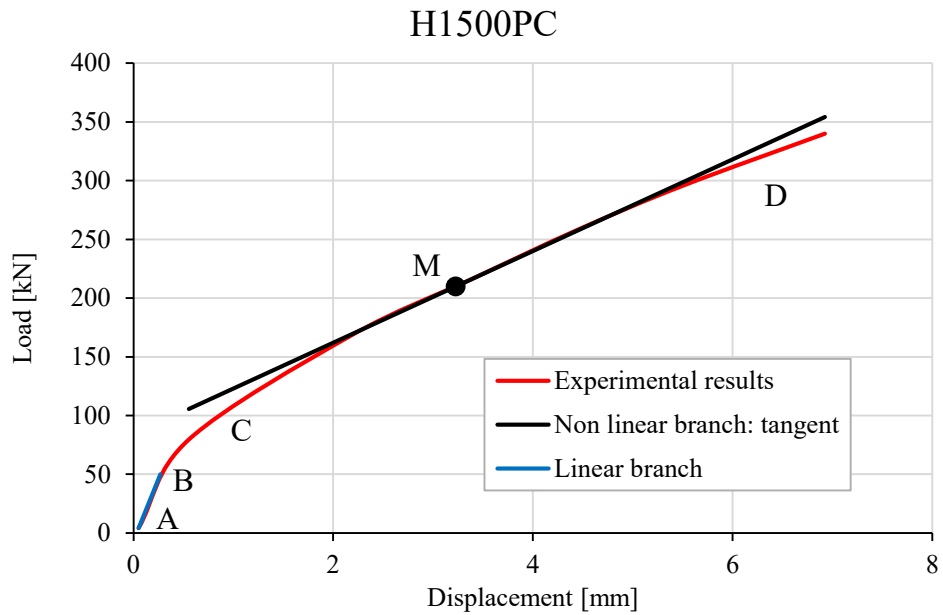


Fig. 93 - Experimental H1500PC load-displacement curve with control parameters

Table 63 - Data input for the evaluation of H1500 experimental S_1

Points	x	y
Point A	0.05	4.20
Point B	0.27	50
Slope S_1		209

Table 64 - Data input for the evaluation of experimental H1500 S_2

Points	x	y
Point C	0.56	79.72
Point D	6.92	339.86
Point M	3.23	209.79
Slope S_2		39

- Numerical curve:

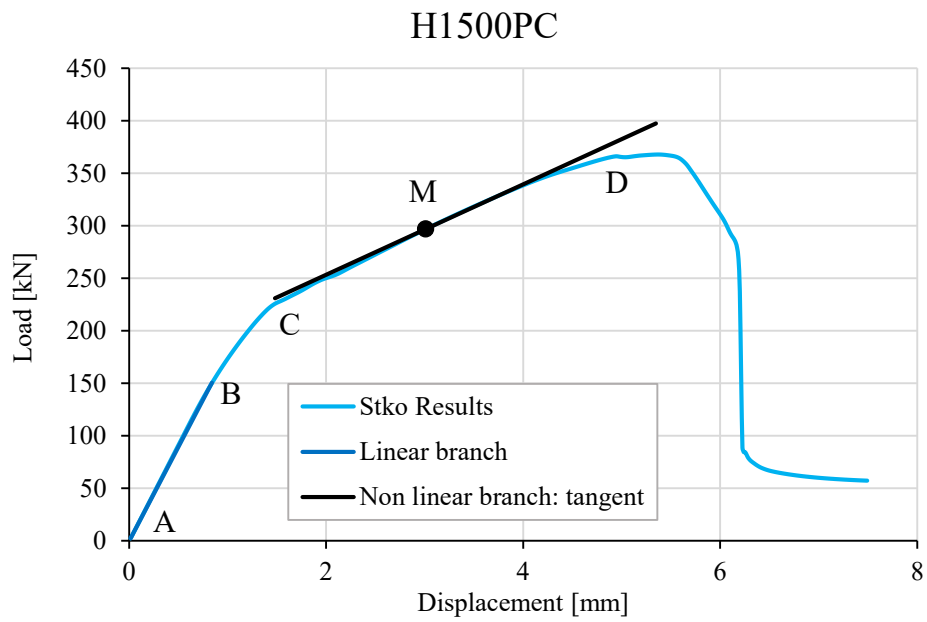


Fig. 94 - Numerical H1500PC load-displacement curve with control parameters

Table 65 - Data input for the evaluation of H1500 numerical S_1

Points	x	y
Point A	0.013	2.44
Point B	0.84	150.46
Slope S_1		179

Table 66 - Data input for the evaluation of H1500 numerical S_2

Points	x	y
Point C	1.48	225.84
Point D	5.35	367.90
Point M	3.01	296.90
Slope S_2		43

- H500FRC50
 - Experimental curve:

H500FRC50

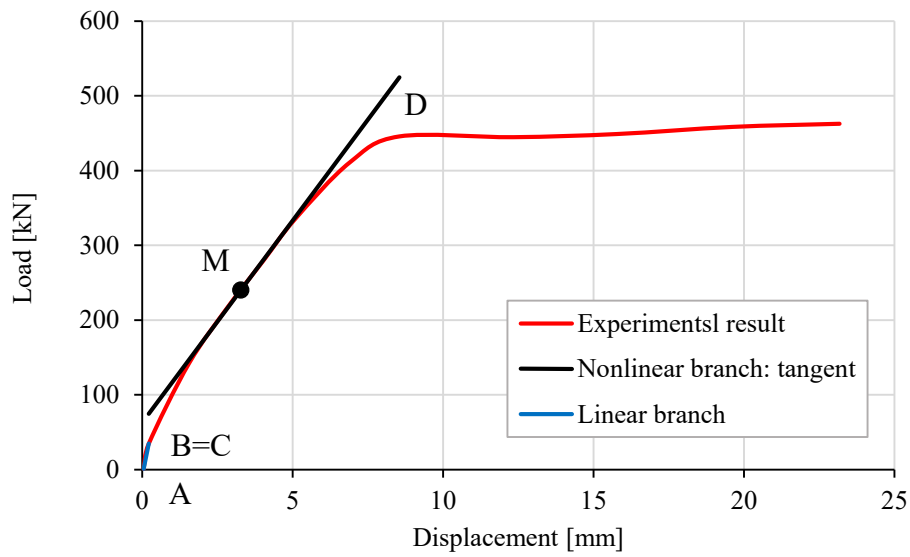


Fig. 95 - Experimental H500FRC50 load-displacement curve with control parameters

Table 67 - Data input for the evaluation of H500FRC50 experimental S_1

Points	x	y
Point A	0.04	1.06
Point B	0.22	34.86
Slope S_1		197

Table 68 - Data input for the evaluation of experimental H500FRC50 S_2

Points	x	y
Point C	0.22	34.86
Point D	8.55	445.77
Point M	3.28	240.32
Slope S_2		54

– Numerical curve:

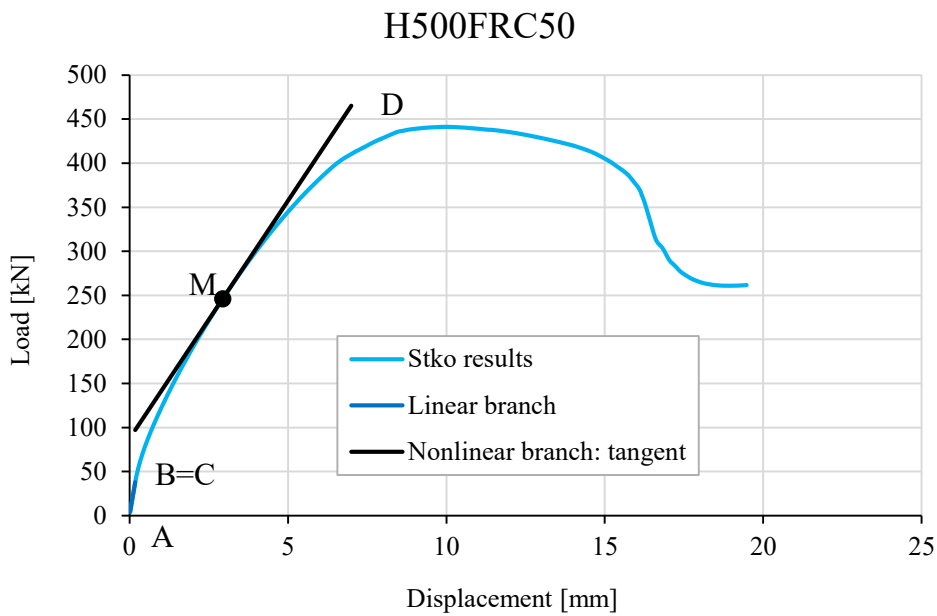


Fig. 96 - Numerical H500FRC50 load-displacement curve with control parameters

Table 69 - Data input for the evaluation of H500FRC50 numerical S_1

Points	x	y
Point A	0.02	4.21
Point B	0.18	37.87
Slope S_1		210

Table 70 - Data input for the evaluation of H500FRC50 numerical S_2

Points	x	y
Point C	0.18	37.86
Point D	8.98	439.05
Point M	2.94	246.06
Slope S_2		54

- H1000FRC50
- Experimental curve:

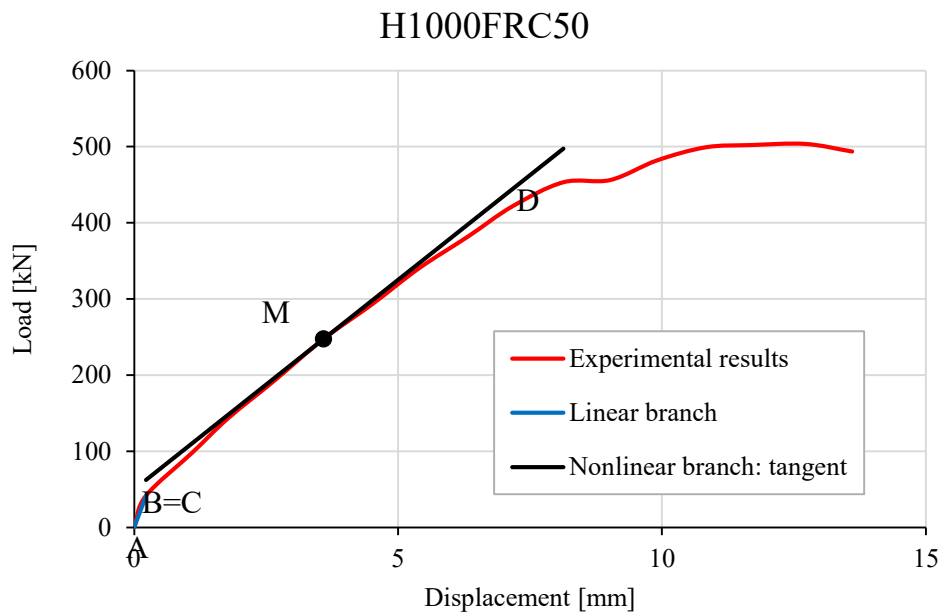


Fig. 97 - Experimental H1000FRC50 load-displacement curve with control parameters

Table 71 - Data input for the evaluation of H1000FRC50 experimental S_1

Points	x	y
Point A	0.00	0
Point B	0.22	41.44
Slope S_1		187

Table 72 - Data input for the evaluation of experimental H1000FRC50 S_2

Points	x	y
Point C	0.22	41.44
Point D	8.13	453.44
Point M	3.586805	247.4412
Slope S_2		55

– Numerical curve:

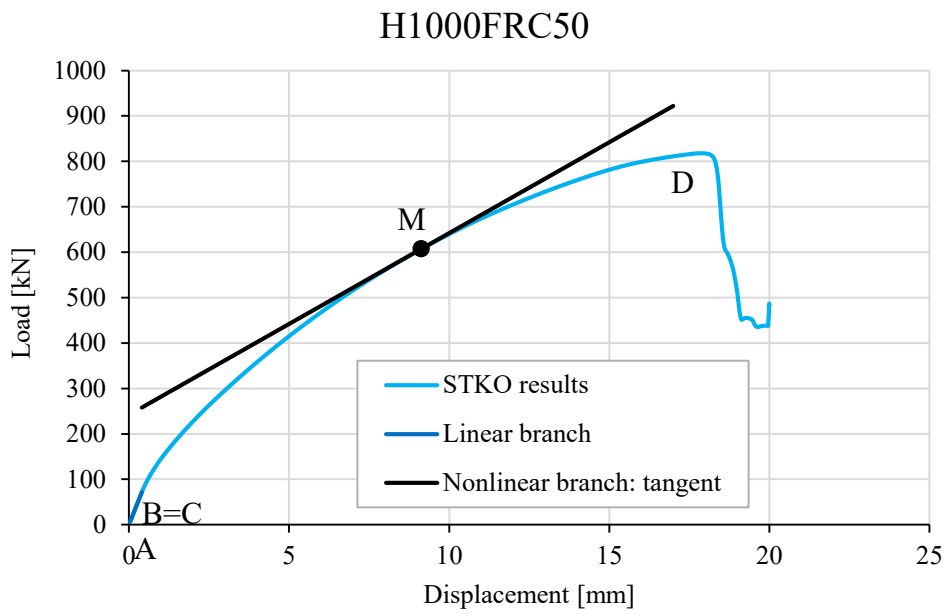


Fig. 98 - Numerical H1000FRC50 load-displacement curve with control parameters

Table 73 - Data input for the evaluation of H1000FRC50 numerical S_1

Points	x	y
Point A	0.03	5.98
Point B	0.4	71.62
Slope S_1		179

Table 74 - Data input for the evaluation of H1000FRC50 numerical S_2

Points	x	y
Point C	0.4	71.62
Point D	17.83	817.83
Point M	9.13	607.33
Slope S_2		40

- H1500FRC50
- Experimental curve:

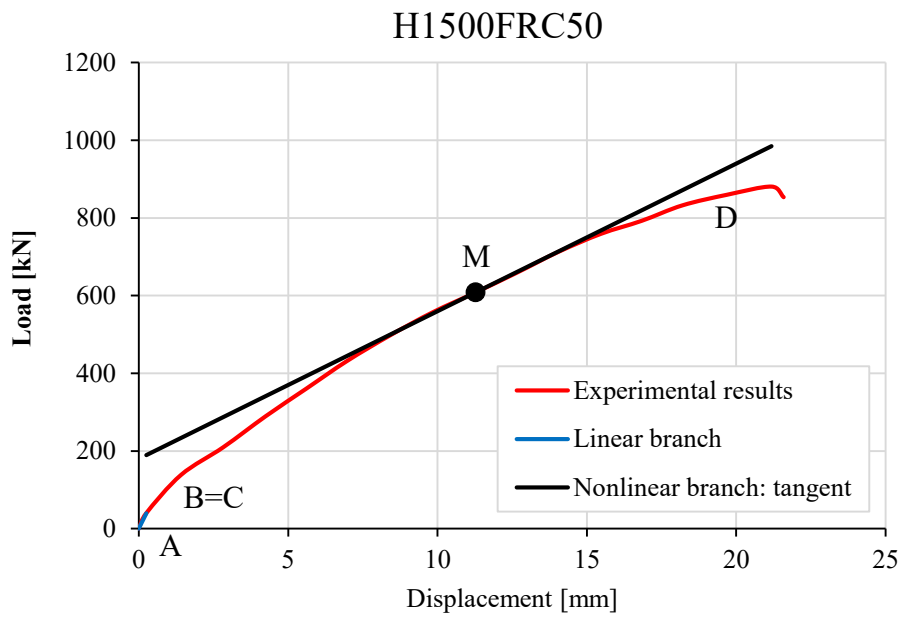


Fig. 99 - Experimental H1500FRC50 load-displacement curve with control parameters

Table 75 - Data input for the evaluation of experimental H1500FRC50 S_1

Points	x	y
Point A	0.00	0.00
Point B	0.25	39.86
Slope S_1		156

Table 76 - Data input for the evaluation of experimental H1500FRC50 S_2

Points	x	y
Point C	0.25	39.86
Point D	21.18	881.12
Point M	11.27	608.39
Slope S_2		38

– Numerical curve:

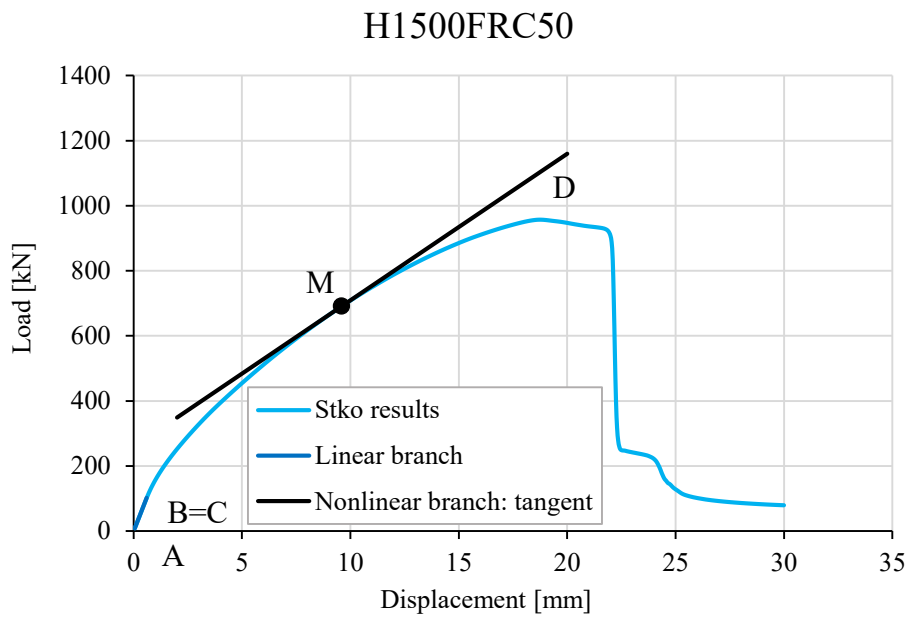


Fig. 100 - Numerical H1500FRC50 load-displacement curve with control parameters

Table 77 - Data input for the evaluation of H1500FRC50 numerical S_1

Points	x	y
Point A	0.05	8.48
Point B	0.6	101.75
Slope S_1		170

Table 78 - Data input for the evaluation of H1500FRC50 numerical S_2

Points	x	y
Point C	0.6	101.75
Point D	18.75	957.54
Point M	9.6	691.45
Slope S_2		45

- H500FRC75
- Experimental curve:

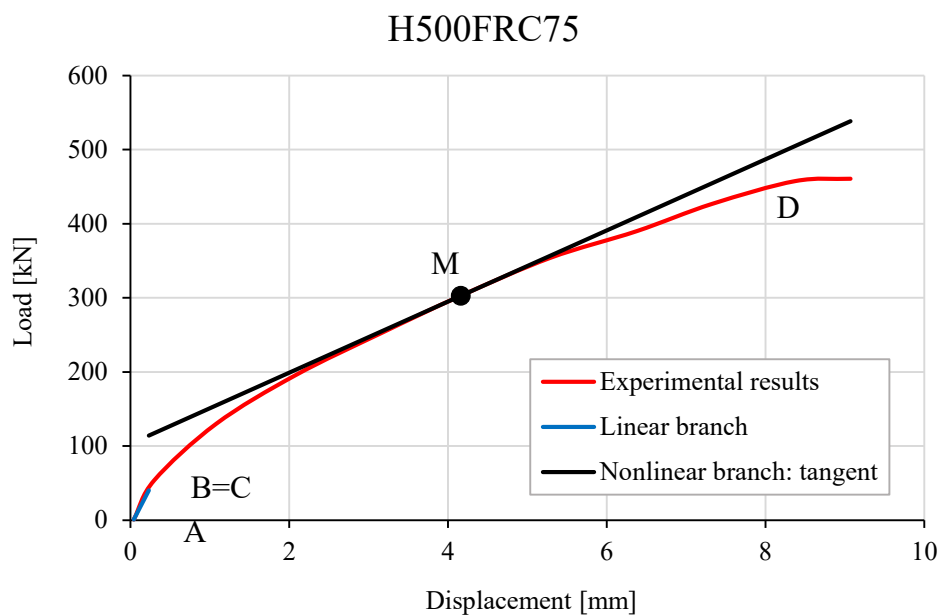


Fig. 101 - Experimental H500FRC75 load-displacement curve with control parameters

Table 79 - Data input for the evaluation of H500FRC75 experimental S_1

Points	x	y
Point A	0.04	1.06
Point B	0.23	40.00
Slope S_1		209

Table 80 - Data input for the evaluation of H500FRC75 experimental S_2

Points	x	y
Point C	0.23	40.00
Point D	9.07	460.56
Point M	4.16	302.64
Slope S_2		48

– Numerical curve:

H500FRC75

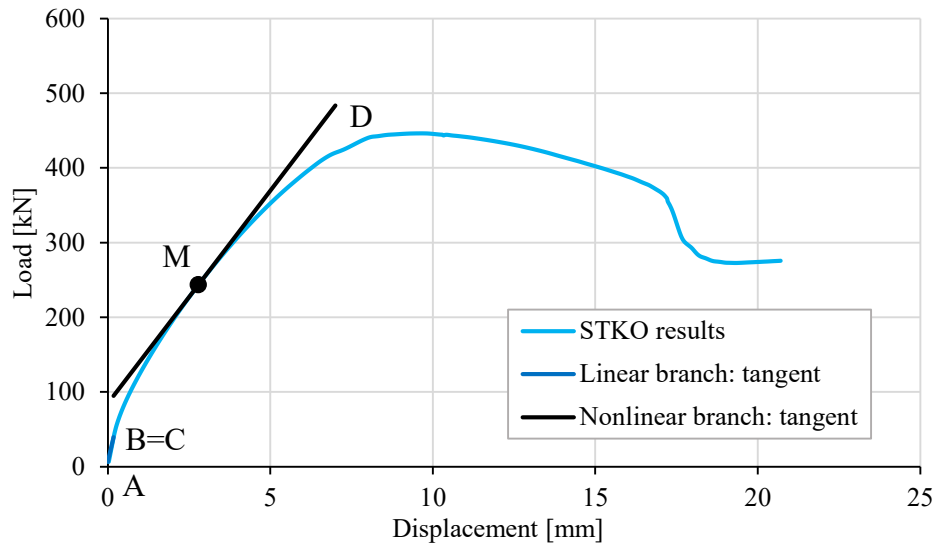


Fig. 102 - Numerical H500FRC75 load-displacement curve with control parameters

Table 81 - Data input for the evaluation of H500FRC75 numerical S_1

Points	x	y
Point A	0	6.57
Point B	0.18	39.40
Slope S_1		182

Table 82 - Data input for the evaluation of H500FRC75 numerical S_2

Points	x	y
Point C	0.18	39.40
Point D	9.6	446.31
Point M	2.79	243.50
Slope S_2		57

- H1000FRC75
- Experimental curve:

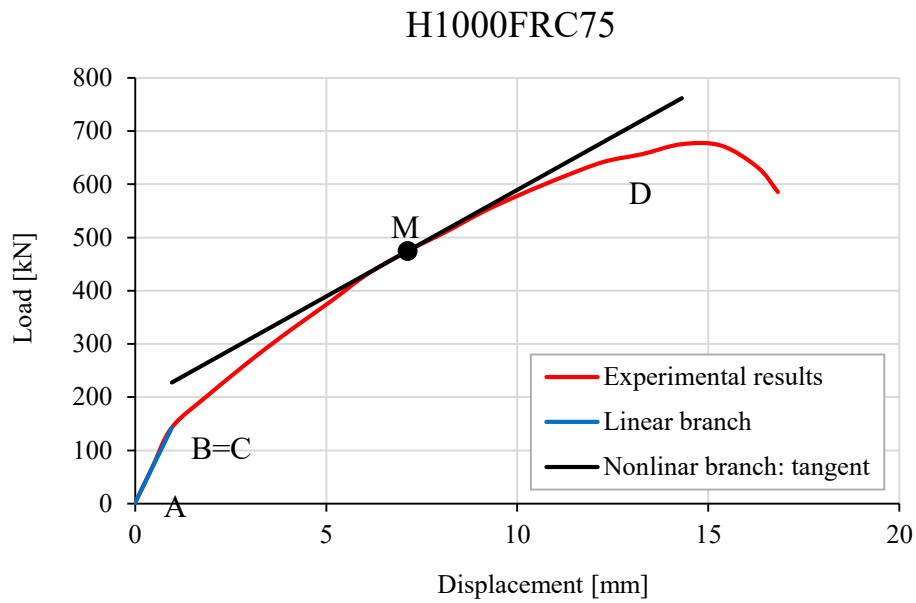


Fig. 103 - Experimental H1000FRC75 load-displacement curve with control parameters

Table 83 - Data input for the evaluation of H1000FRC75 experimental S_1

Points	x	y
Point A	0.00	1.43
Point B	0.96	142.93
Slope S_1		147

Table 84 - Data input for the evaluation of H1000FRC75 experimental S_2

Points	x	y
Point C	0.96	142.93
Point D	14.31	675.31
Point M	7.13	474.80
Slope S_2		40

– Numerical curve:

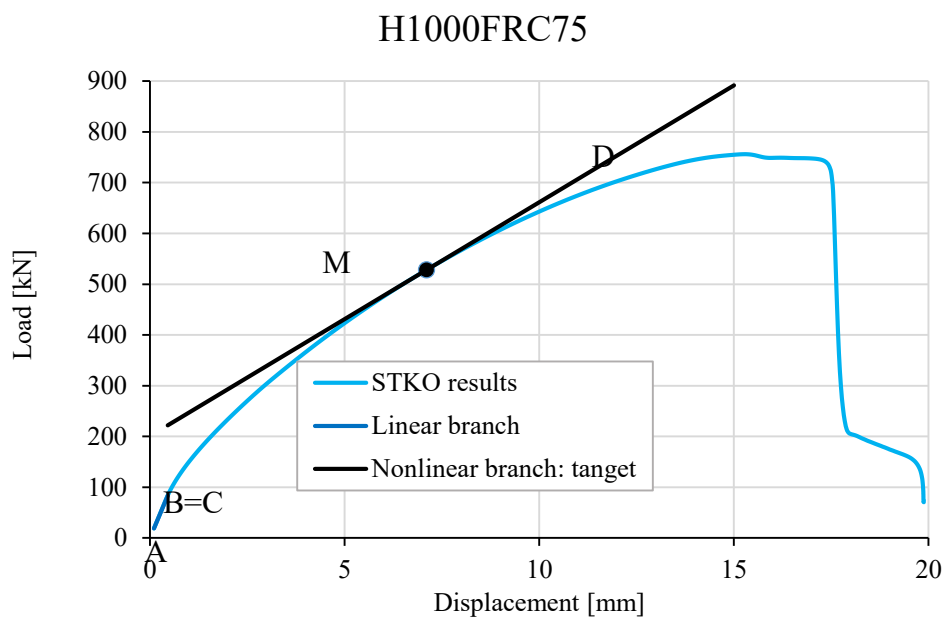


Fig. 104 - Numerical H1000FRC75 load-displacement curve with control parameters

Table 85 - Data input for the evaluation of H1000 numerical S_1

Points	x	y
Point A	0.1	18.60
Point B	0.45	83.14
Slope S_1		184

Table 86 - Data input for the evaluation of H1000FRC75 numerical S_2

Points	x	y
Point C	0.45	83.142
Point D	17.1	756.13
Point M	7.1	528.01
Slope S_2		46

- H1500FRC75
- Experimental curve:

H1500FRC75

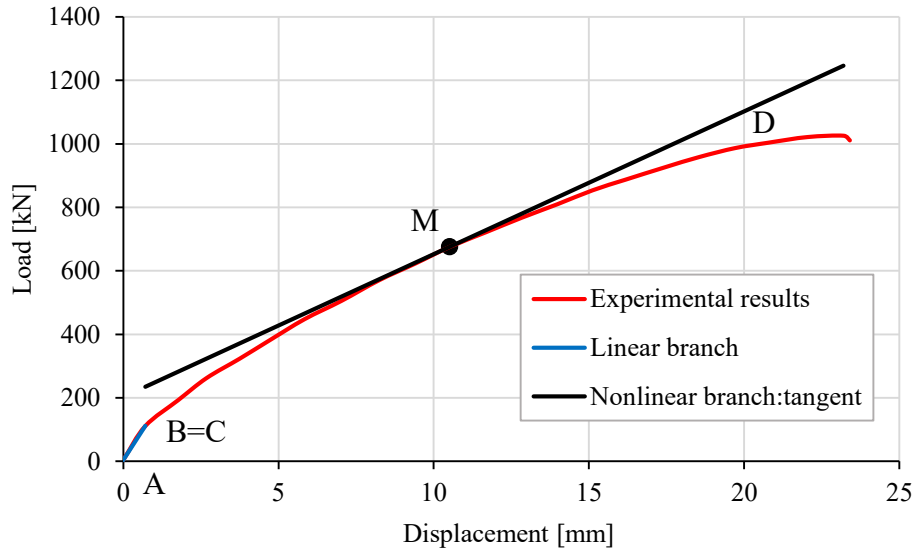


Fig. 105 - Experimental H1500FRC75 load-displacement curve with control parameters

Table 87 - Data input for the evaluation of H1500FRC75 experimental S_1

Points	x	y
Point A	0.00	4.20
Point B	0.71	111.19
Slope S_1		151

Table 88 - Data input for the evaluation of H1500FRC75 experimental S_2

Points	x	y
Point C	0.71	111.19
Point D	23.20	1025.87
Point M	10.51	675.52
Slope S_2		45

– Numerical curve:

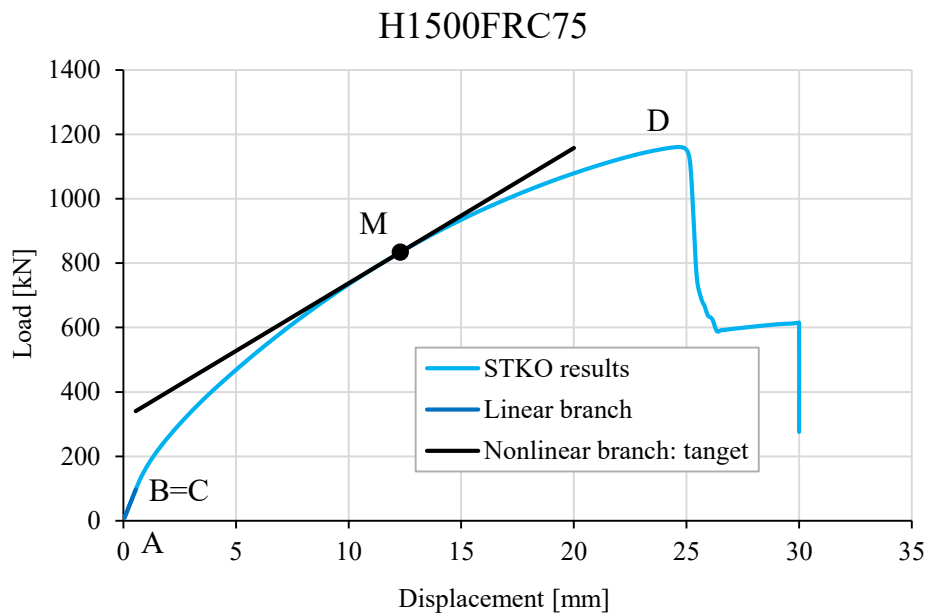


Fig. 106 - Numerical H1500FRC75 load-displacement curve with control parameters

Table 89 - Data input for the evaluation of H1500FRC75 numerical S_1

Points	x	y
Point A	0.05	8.80
Point B	0.55	96.78
Slope S_1		176

Table 90 - Data input for the evaluation of H1500FRC75 numerical S_2

Points	x	y
Point C	0.55	96.80
Point D	24.65	1161.15
Point M	12.3	834.33
Slope S_2		42

- H500FRC50 – adjusted G_t
- Numerical curve:

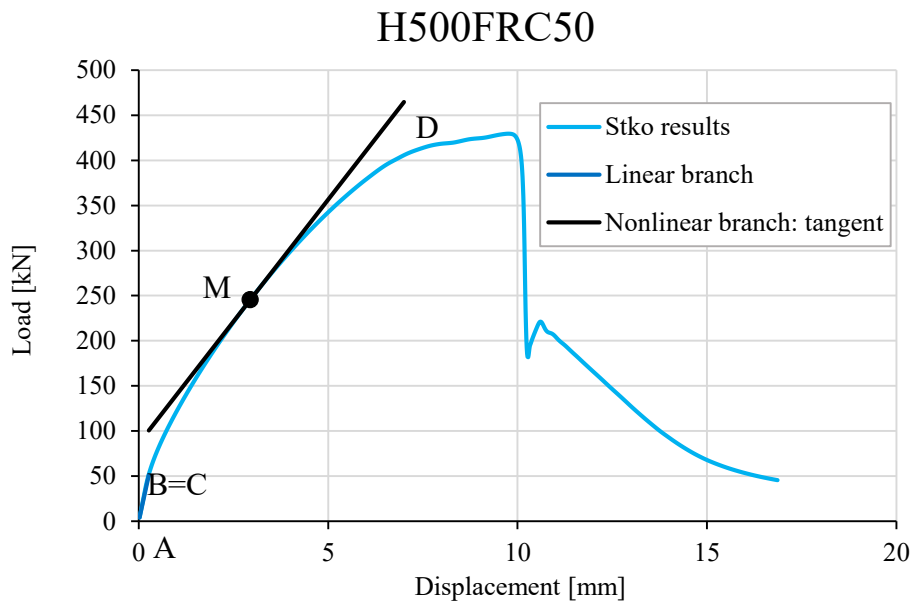


Fig. 107 - Numerical H500FRC50 load-displacement curve with control parameters with G_t adjusted

Table 91 - Data input for the evaluation of H500FRC50 numerical S_1 with G_t adjusted

Points	x	y
Point A	0.02	4.215
Point B	0.26	51.46
Slope S_1		197

Table 92 - Data input for the evaluation of H500FRC50 numerical S_2 with G_t adjusted

Points	x	y
Point C	0.26	51.46
Point D	8.98	424.34
Point M	2.94	245.40
Slope S_2		54

- H1000FRC50 – adjusted G_t
- Numerical curve:

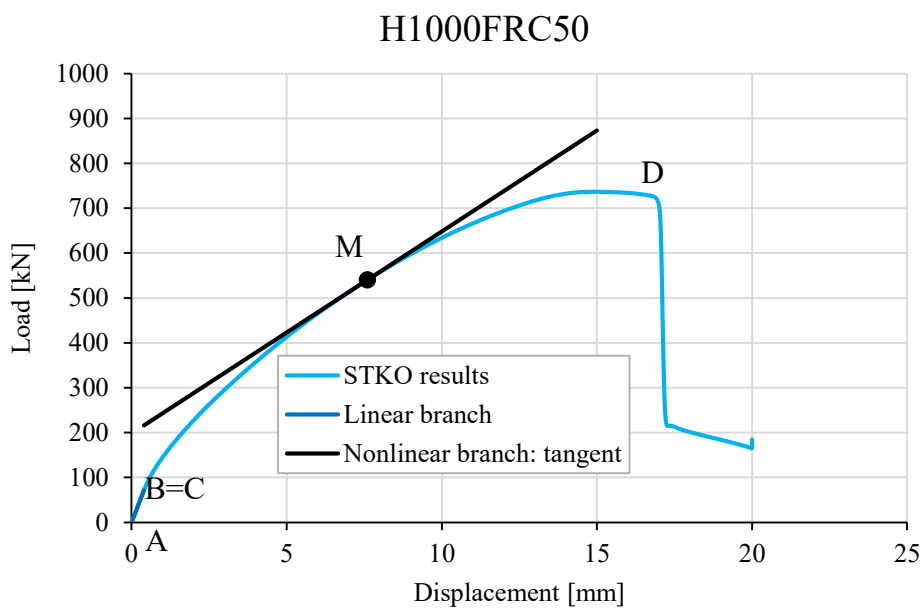


Fig. 108 - Numerical H1000FRC50 load-displacement curve with control parameters with G_t adjusted

Table 93 - Data input for the evaluation of H1000FRC50 numerical S_1 with G_t adjusted

Points	x	y
Point A	0.03	5.98
Point B	0.4	71.62
Slope S_1		179

Table 94 - Data input for the evaluation of H1000FRC50 numerical S_2 with G_t adjusted

Points	x	y
Point C	0.4	71.62
Point D	14.8	736.48
Point M	7.6	540.11
Slope S_2		45

- H1500FRC50 – adjusted G_t
- Numerical curve:

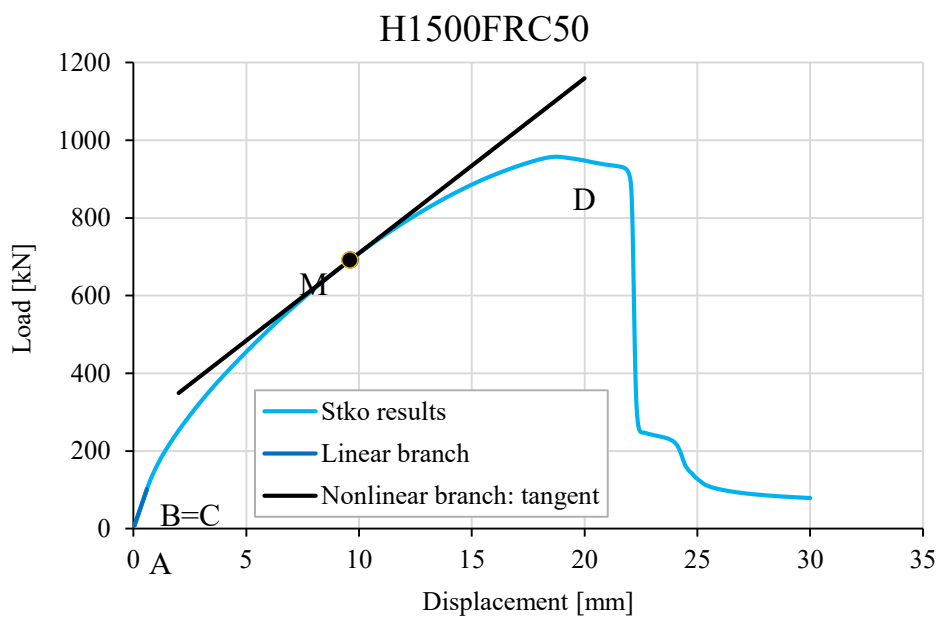


Fig. 109 - Numerical H1500FRC50 load-displacement curve with control parameters with G_t adjusted

Table 95 - Data input for the evaluation of H1500FRC50 numerical S_1 with G_t adjusted

Points	x	y
Point A	0.05	8.48
Point B	0.6	101.75
Slope S_1		170

Table 96 - Data input for the evaluation of H1500FRC50 numerical S_2 with G_t adjusted

Points	x	y
Point C	0.6	101.75
Point D	18.75	957.54
Point M	9.6	691.45
Slope S_2		45

- H500FRC75 – adjusted G_t
- Numerical curve:

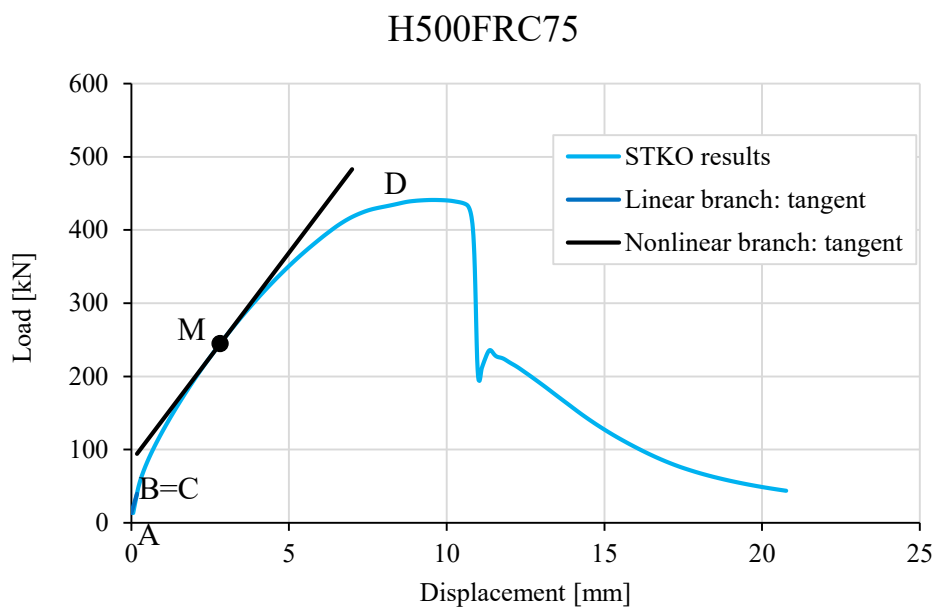


Fig. 110 - Numerical H500FRC75 load-displacement curve with control parameters with G_t adjusted

Table 97 - Data input for the evaluation of H500FRC75 numerical S_1 with G_t adjusted

Points	x	y
Point A	0	13.13
Point B	0.18	39.40
Slope S_1		146

Table 98 - Data input for the evaluation of H500FRC75 numerical S_2 with G_t adjusted

Points	x	y
Point C	0.18	39.40
Point D	9.63	441.03
Point M	2.82	244.73
Slope S_2		57

- H1000FRC75 – adjusted G_t
- Numerical curve:

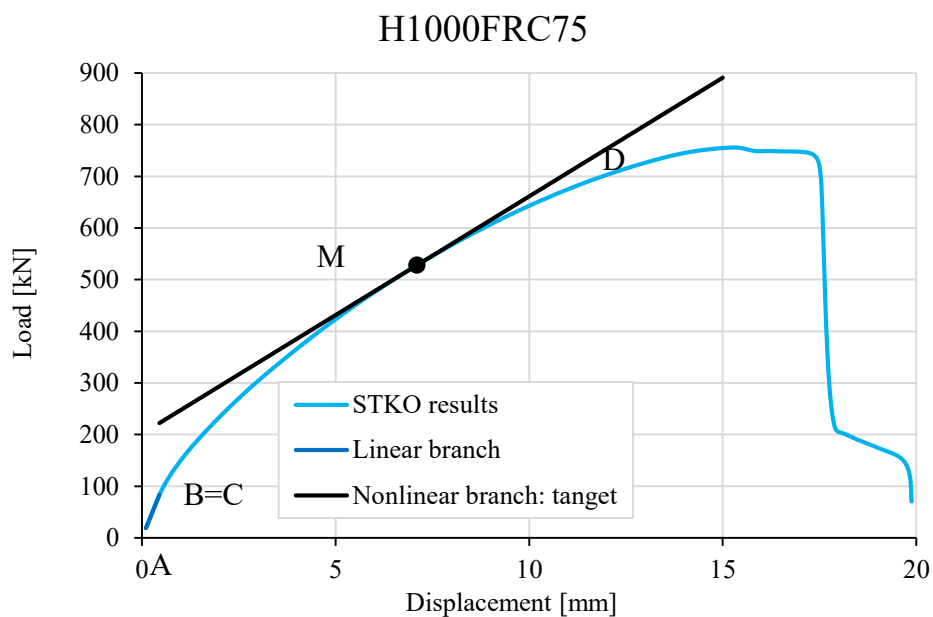


Fig. 111 - Numerical H1000FRC75 load-displacement curve with control parameters with G_t adjusted

Table 99- Data input for the evaluation of H1000FRC75 numerical S_1 with G_t adjusted

Points	x	y
Point A	0.1	18.60
Point B	0.45	83.14
Slope S_1		184

Table 100 - Data input for the evaluation of H1000FRC75 numerical S_2 with G_t adjusted

Points	x	y
Point C	0.45	83.14
Point D	17.1	756.13
Point M	7.1	528.01
Slope S_2		46

- H1500FRC75 – adjusted G_t
- Numerical curve:

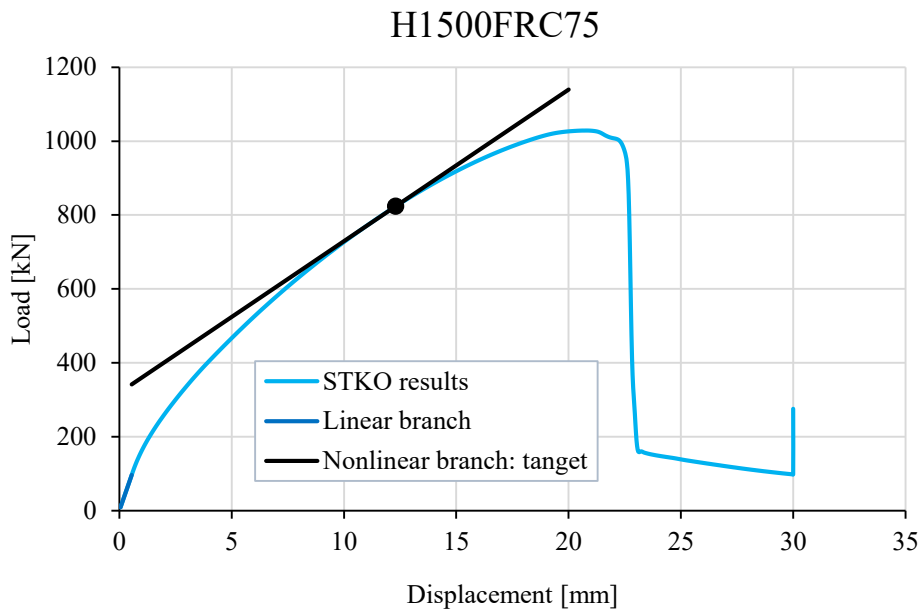


Fig. 112 - Numerical H1500FRC75 load-displacement curve with control parameters with G_t adjusted

Table 101 - Data input for the evaluation of H1500FRC75 numerical S_1 with G_t adjusted

Points	x	y
Point A	0.05	8.80
Point B	0.55	96.78
Slope S_1		176

Table 102 - Data input for the evaluation of H1500FRC75 numerical S_2 with G_t adjusted

Points	x	y
Point C	0.55	96.78
Point D	24.65	1029.03
Point M	12.3	823.75
Slope S_2		41

- *Final report for FRC50 with adjusted G_t*

Table 103 - Control parameters for H500FRC50 with G_t adjusted

H500FRC50 – adjusted G_t	P_{cr} [kN]	P_u [kN]	δ [mm]	S_1 [-]	S_2 [-]
Experimental results	35	471.75	23.18	197	54
STKO predictions	37	429	10.56	210	54
Manual evaluations	39	394	-	-	-
STKO predictions/Experimental results	1.06	1.10	0.46	1.07	1.00
Manual evaluation/Experimental results	1.11	0.83	-	-	-

Table 104 - Control parameters for H1000FRC50 with G_t adjusted

H1000FRC50 – adjusted G_t	P_{cr} [kN]	P_u [kN]	δ [mm]	S_1 [-]	S_2 [-]
Experimental results	41	527.5	11.68	187	55
STKO predictions	71	737	14.80	179	45
Manual evaluations	70	722	-	-	-
STKO predictions/Experimental results	1.73	0.72	1.27	0.96	0.82
Manual evaluation/Experimental results	1.71	1.37	-	-	-

Table 105 - Control parameters for H1500FRC50 with G_t adjusted

H1500FRC50 – adjusted G_t	P_{cr} [kN]	P_u [kN]	δ [mm]	S_1 [-]	S_2 [-]
Experimental results	39	943.25	21.18	158	38
STKO predictions	101	958	18.75	170	45
Manual evaluations	104	1019	-	-	-
STKO predictions/Experimental results	2.59	0.99	0.89	1.08	1.18
Manual evaluation/Experimental results	2.67	1.08	-	-	-

- *Final report for FRC75 with adjusted G_t*

Table 106 - Control parameters for H500FRC75 with G_t adjusted

H500FRC75 – adjusted G_t	P_{cr} [kN]	P_u [kN]	δ [mm]	S_1 [-]	S_2 [-]
Experimental results	40	461.75	9.07	209	48
STKO predictions	39.395	441	9.63	146	57
Manual evaluations	39	416	-	-	-
STKO predictions/Experimental results	0.98	1.05	1.06	0.70	1.19
Manual evaluation/Experimental results	0.98	0.90	-	-	-

Table 107 - Control parameters for H1000FRC50 with G_t adjusted

H1000FRC75 – adjusted G_t	P_{cr} [kN]	P_u [kN]	δ [mm]	S_1 [-]	S_2 [-]
Experimental results	67.17	685.5	14.31	149	40
STKO predictions	71	756	17.10	184	46
Manual evaluations	70	722	-	-	-
STKO predictions/Experimental results	1.06	0.91	1.20	1.24	1.15
Manual evaluation/Experimental results	1.04	1.05	-	-	-

Table 108 - Control parameters for H1500FRC75 with G_t adjusted

H1500FRC75 – adjusted G_t	P_{cr} [kN]	P_u [kN]	δ [mm]	S_1 [-]	S_2 [-]
Experimental results	39	943.25	23.20	151	45
STKO predictions	101	1029	24.65	176	41
Manual evaluations	104	1073	-	-	-
STKO predictions/Experimental results	2.59	0.92	1.06	1.16	0.91
Manual evaluation/Experimental results	2.67	1.14	-	-	-

2.1 FEM cross section of Cuenca's beams

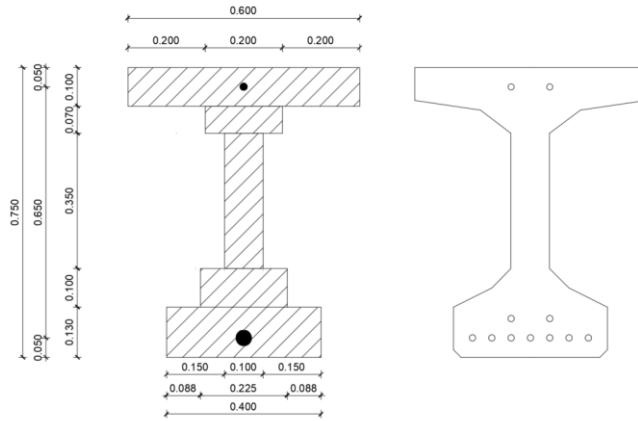


Fig. 113 - Comparison between HF600/5's FEM and real section

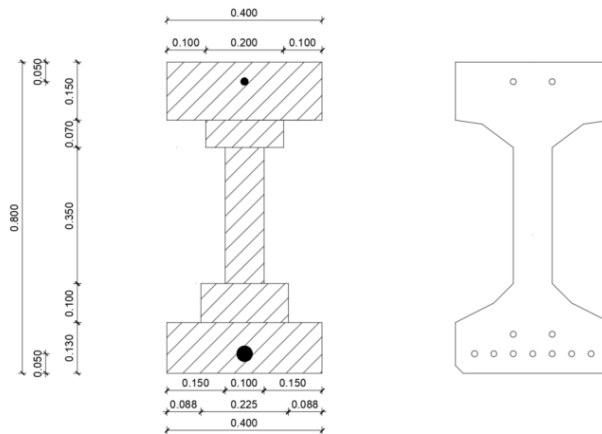


Fig. 114 - Comparison between HF400h/6's FEM and real section

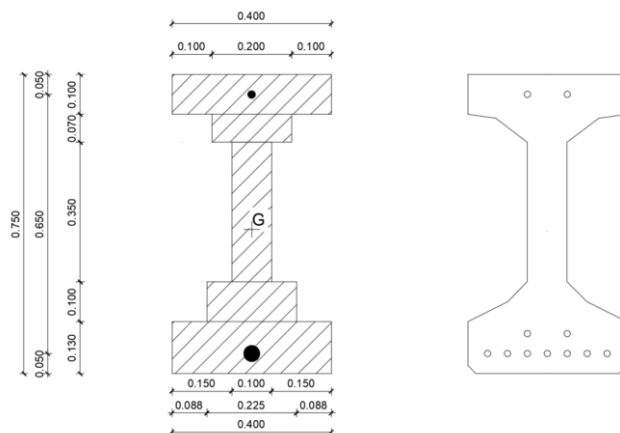


Fig. 115 - Comparison between HF400/7's FEM and real section

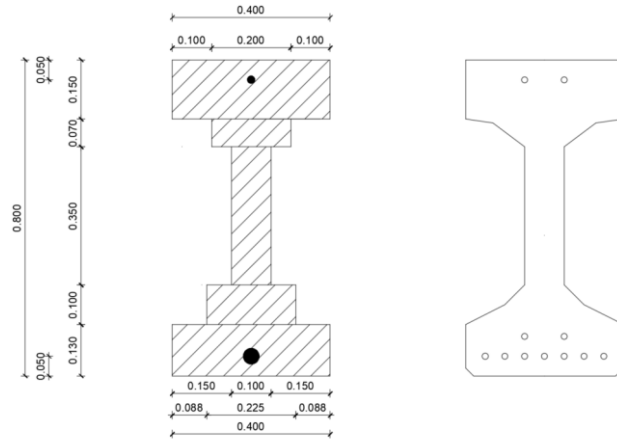


Fig. 116 - Comparison between HF260/9's FEM and real section

2.2 Pre-stressing action on Cuenca's beams

In the following part the main geometrical proprieties and the pre-stressing action are reported:

- A: total area
- S: first moment of inertia
- y_G : coordinate of centroid respect to the extreme bottom fiber
- I: second moment of inertia
- P_{tot} : pre-stressing action
- M_p : moment induced by the P_{tot} eccentricity
- M_{ext} : external moment which decompresses the middle section

- *HF600/5*

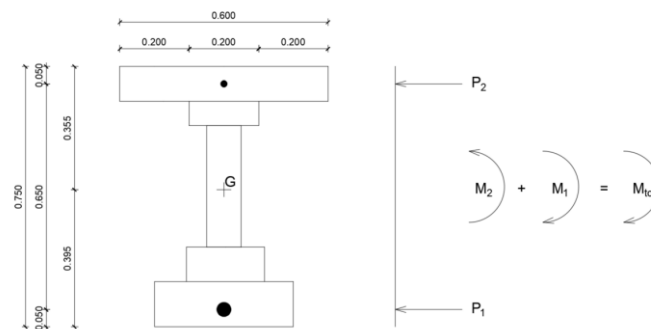


Fig. 117 - HF600/5 FEM model section with pre-stressing action

Table 109 - Geometric characteristic and pre-stressing action on HF600/5

HF600/5	
A [mm ²]	189905.95
S [mm ³]	73292363.64
y _G [mm]	385.94
I [mm ⁴]	14178526899.67
P _{tot} [kN]	-1538.46
M _p [kNm]	-335.01
M _{cxt} [kNm]	632.63

- HF400/7

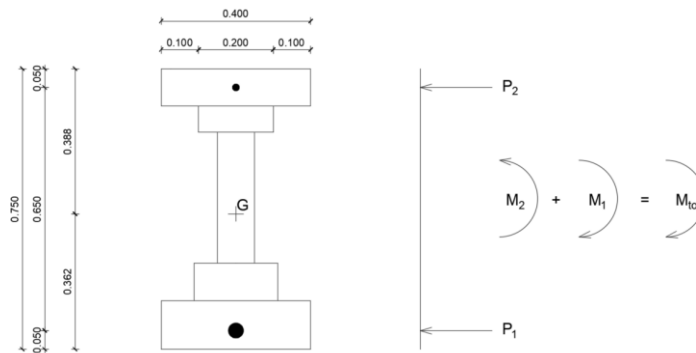


Fig. 118 - HF400/7 FEM model section with pre-stressing action

Table 110 - Geometric characteristic and pre-stressing action on HF400/7

HF400/7	
A [mm ²]	169905.95
S [mm ³]	59292363.64
y _G [mm]	348.97
I [mm ⁴]	11879349317.83
P _{tot} [kN]	-1538.46
M _p [kNm]	-278.14
M _{cxt} [kNm]	586.37

- HF400h/6

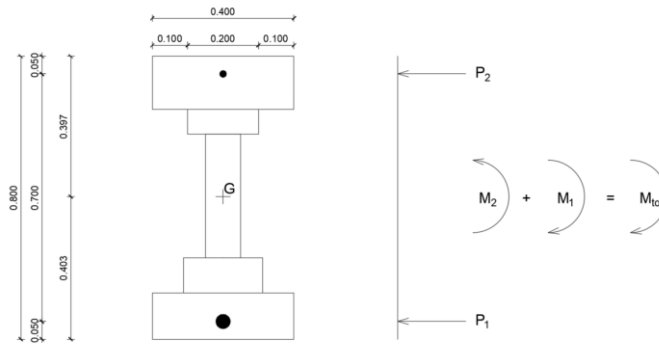


Fig. 119 - HF400h/6 FEM model section with pre-stressing action

Table 111 - Geometric characteristic and pre-stressing action on HF400h/6

HF400h/6	
A [mm ²]	189905.95
S [mm ³]	74792363.64
y _G [mm]	393.84
I [mm ⁴]	13113853530.78
P _{tot} [kN]	-1538.46
M _p [kNm]	-347.16
M _{ext} [kNm]	616.91

- HF260/9

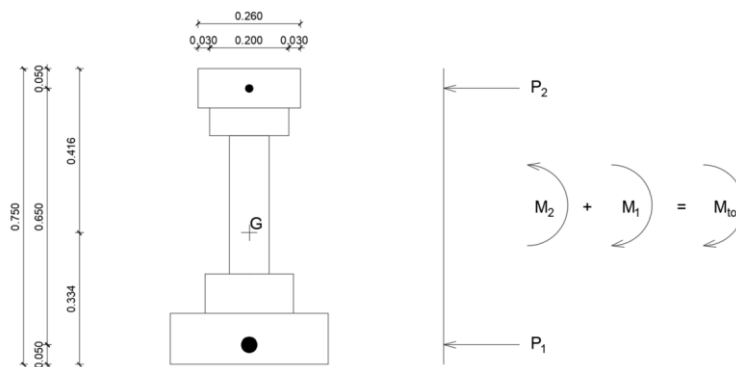


Fig. 120 - HF260/9 FEM model section with pre-stressing action

Annex 3

3.1 Analytic evaluations with MC10 and EC2-draft

- *Minelli's beams*

Table 114 - $V_{u, MC10}$ evaluation for Minelli's beams

Minelli's beams	H500 FRC50	H1000 FRC50	H1500 FRC50	H500 FRC75	H1000 FRC75	H1500 FRC75
γ_c [-]	1	1	1	1	1	1
d [mm]	440	940	1440	440	940	1440
k [-]	1.67	1.46	1.37	1.67	1.46	1.37
ρ_l [-]	0.0112	0.0107	0.01	0.0112	0.0107	0.01
f_{tuk} [MPa]	1.67	1.67	1.67	2.01	2.01	2.01
f_{ctm} [MPa]	2.4	2.4	2.4	2.5	2.5	2.5
f_{cm} [MPa]	32.1	32.1	32.1	33.1	33.1	33.1
b_w [mm]	250	250	250	250	250	250
$V_{u, MC10}$ [N]	201194	369488	519852	211742	388859	547106

Table 115 - $V_{u, EC2-draft}$ evaluation for Minelli's beams

Minelli's beams	H500 FRC50	H1000 FRC50	H1500 FRC50	H500 FRC75	H1000 FRC75	H1500 FRC75
γ_c [-]	1	1	1	1	1	1
γ_F [-]	1	1	1	1	1	1
γ_V [-]	1	1	1	1	1	1
d [mm]	440	940	1440	440	940	1440
z [mm]	396	846	1296	396	846	1296
ρ_l [-]	0.0112	0.0107	0.01	0.0112	0.0107	0.01
f_{yd} [MPa]	440	440	440	440	440	440
f_{tuk} [MPa]	1.67	1.67	1.67	2.01	2.01	2.01
f_{tud} [MPa]	1.67	1.67	1.67	2.01	2.01	2.01
f_{ctm} [MPa]	2.4	2.4	2.4	2.5	2.5	2.5
f_{cm} [MPa]	32.1	32.1	32.1	33.1	33.1	33.1
D [mm]	5	5	5	5	5	5
d_{dg} [mm]	21	21	21	21	21	21
b_w [mm]	250	250	250	250	250	250
η [-]	0.4	0.4	0.4	0.4	0.4	0.4
$\tau_{Rd,c, min}$ [MPa]	0.18	0.12	0.10	0.18	0.12	0.10
$\tau_{Rd,cf}$ [MPa]	1.96	1.89	1.86	2.30	2.23	2.20
$\eta\tau_{Rd,c, min} + f_{tud}$ [MPa]	1.74	1.72	1.71	2.08	2.06	2.05
$V_{u, EC2-draft}$ [N]	193775	399676	601458	227728	472064	712238

- *Cuenca's beams*

Table 116 - $V_{u, MC10}$ evaluation for Cuenca's beams

Cuenca's beams	HF600/5	HF400/7	HF400h/6	HF260/9
γ_c [-]	1	1	1	1
d [mm]	700	700	750	700
k [-]	1.53	1.53	1.52	1.53
ρ_l [-]	0.0183	0.0183	0.0171	0.0183
$f_{t_{uk}}$ [MPa]	1.85	1.59	1.99	1.89
f_{ctm} [MPa]	4.2	4.08	4.45	3.11
f_{cm} [MPa]	65.9	63.5	59.5	65
σ_{cp} [MPa]	8.38	9.41	8.38	10.29
b_w [mm]	100	100	100	100
$V_{u, MC10}$ [N]	179685	176096	181788	198280

Table 117 - $V_{u, EC2-draft}$ evaluation for Cuenca's beams

Cuenca's beams	HF600/5	HF400/7	HF400h/6	HF260/9
γ_c [-]	1	1	1	1
γ_F [-]	1	1	1	1
γ_V [-]	1	1	1	1
d [mm]	700	700	750	700
z [mm]	630	630	675	630
ρ_l [-]	0.0183	0.0183	0.0171	0.0183
f_{yd} [MPa]	1617	1617	1617	1617
$f_{t_{uk}}$ [MPa]	1.85	1.59	1.99	1.89
$f_{t_{ud}}$ [MPa]	1.85	1.59	1.99	1.89
f_{ctm} [MPa]	4.2	4.08	4.45	3.11
f_{cm} [MPa]	65.9	63.5	59.5	65
D [mm]	5	5	5	5
d_{dg} [mm]	20.14	20.46	21.08	20.26
b_w [mm]	100	100	100	100
η [-]	0.4	0.4	0.4	0.4
σ_{cp} [MPa]	8.38	9.41	8.38	10.29
$\tau_{Rd,c, min}$ [MPa]	0.08	0.07	0.07	0.08
$\tau_{Rd,cf}$ [MPa]	3.47	3.36	3.59	3.80
$\eta \tau_{Rd,c, min} + f_{t_{ud}}$ [MPa]	1.88	1.62	2.02	1.92
$V_{u, EC2-draft}$ [N]	218633	211824	242169	239141

- UPM's beams

Table 118 - $V_{u, MC10}$ evaluation for UPM's beams

UPM's beams	BMI12	UMI12
γ_c [-]	1	1
d [mm]	760	760
k [-]	1.51	1.51
ρ_l [-]	0.0217	0.0217
f_{tuk} [MPa]	5.33	5.33
f_{ctm} [MPa]	5.6	5.6
f_{cm} [MPa]	120	120
σ_{cp} [MPa]	12.11	12.11
b_w [mm]	100	100
$V_{u, MC10}$ [N]	303455	303455

Table 119 - $V_{u, EC2-draft}$ evaluation for UPM's beams

UPM's beams	BMI12	UMI12
γ_c [-]	1	1
γ_F [-]	1	1
γ_V [-]	1	1
d [mm]	760	760
z [mm]	684	684
ρ_l [-]	0.0183	0.0183
f_{yd} [MPa]	1617	1617
f_{tuk} [MPa]	5.33	5.33
f_{tud} [MPa]	5.33	5.33
f_{ctm} [MPa]	5.33	5.33
f_{cm} [MPa]	120	120
D [mm]	5	5
d_{dg} [mm]	17.25	17.25
b_w [mm]	100	100
η [-]	0.4	0.4
σ_{cp} [MPa]	12.11	12.11
$\tau_{Rd,c, min}$ [MPa]	0.12	0.12
$\tau_{Rd,cf}$ [MPa]	7.56	7.56
$\eta\tau_{Rd,c, min} + f_{tud}$ [MPa]	5.38	5.38
$V_{u, EC2-draft}$ [N]	516862	516862

Acknowledgments

At the end of this long path, I have to give my acknowledgements to those people who are part of it and have made possible my success.

First of all, I want to thank Professor *Giuseppe Carlo Marano*, for his kindness and humanity, for believing and trusting in me, giving me the possibility to live the most important experience in my life at *Universidad Politécnica de Madrid*. I will be infinitely grateful.

I would like to express my appreciation also to all the professors of *Departamento de mecánica de medios continuos y teoría de estructuras* of *ETS de Ingenieros de Caminos Canales y Puertos de Madrid*. In particular, to Professors *Hugo Corres Peiretti* and *Leonardo Todisco*. Thanks for accepting me and treating me as an equal from the first day. Working with you has been an honor. I will always remember your advice, expert and extensive knowledge and principles you have passed to me.

A special acknowledgement is for *Rafa*, who has always been on my left side in these three months. Thanks for your patience, for your dedication, for your aptitude and your kindness. Thanks for encouraging me, supporting and listening to me in the bad moments as well as for celebrating me in the successful ones. I don't have enough words to express my gratitude. You have been not just a supervisor but an older brother, a friend.

I would like to say thanks also to *Raffaele*, who followed my work and helped me in the drafting of the documents being thousands of miles away. Thank you for your patience, time, help and advice.

Thanks also to my *Compañeros de oficina*, for making me feel at home and part of the group since the first day, involving me in all the activities. In particular, thank you, *Benny*, for your kindness, your advice and your sympathy. Thank you, *Carlos*, because with your cheerfulness you are the soul of the office, taking away the bad thoughts and making everyone's day better. Finally, thank you, *Marck*, for the advice and support given to me.

A big thanks goes also to my *Compagñeros de piso*, *Francesco*, *Federica*, *Claudia*, *Mateo*, *Ann* and *Claudio*. We have rubbed shoulders in these three long months, understanding, listening and encouraging me. I hope to meet all of you somewhere in the world one time.

I will bring Madrid forever in my heart, especially the people who I met and the experience I lived.

The biggest acknowledgement goes to all my family, for always supporting and believing in me. Thank you, *Mamma*, for teaching me how to get over every time I fall and fight to achieve what I aspire to. Thank you, *Papà*, for teaching me that to achieve a goal you need work, sacrifice and passion. Thank you, *Umberto*, for always supporting my career. Finally, thanks to my *Grandparents*, for being unconditionally my supporters and teaching me the values which make the person that I am. Thanks to you, *Nonna Maria*, even without being here with us, I know you would have been proud and happy for your spiteful and messy granddaughter.

I would like to express my gratitude also to those people who have lived with me day by day through this long master course experience. Thank you, *Beppe*, for thousands of video calls, notes and explanations given, but especially thanks for listening to my worries and anxieties, for encouraging me and being my shoulders during those two years, not easy for all of us. Thank you, *Fra*, for your sympathy and friendship which have made the tough study moments less heavy.

Finally, thank you to all the new and old friends who I met in this long university path, to all the people who have believed in me and pushed me over my difficulties. In particular, thanks to the girls who are always part of my life, *Veronica*, *Marzia*, *Marigia* and *Federica*. Thank you for supporting me in my choices and following me wherever my crazy head chose to bring me. You are my refuge, my port and my salvation always.

Torino, 14th December 2021.

Antonella Marinelli